GENERATION OF HIGH-FLUX ATTOSECOND PULSES AND TOWARDS ATTOSECOND-ATTOSECOND PUMP-PROBE EXPERIMENTS

by

YANG WANG
B.S., University of Science and Technology of China, 2006
M.S., Wuhan Institute of Physics and Mathematics of the Chinese Academy of Sciences, 2010

A dissertation submitted in partial fulfilment of the requirements
for the degree of Doctor of Philosophy
in the College of Optics and Photonics
at the University of Central Florida
Orlando, Florida

Fall Term
2017

Major Professor: Zenghu Chang

ABSTRACT

At present, the energy of a single isolated attosecond pulse is limited to nanojoule levels. As a result, an intense femtosecond pulse has always been used in combination with a weak attosecond pulse in time-resolved experiments. To reach the goal of conducting true attosecond pump-attosecond probe experiments, a high flux laser source has been developed that can potentially deliver microjoule level isolated attosecond pulses in the 50 eV range, and a unique experimental end station has been fabricated and implemented that can provide precision control of the attosecond-attosecond pump-probe pulses. In order to scale up the attosecond flux, a unique Ti:-Sapphire laser system with a three-stage amplifier that delivers pulses with a 2 J energy at a 10 Hz repetition rate was designed and built. The broadband pulse spectrum covering from 700 nm to 900 nm was generated, supporting a pulse duration of 12 fs. The high flux high-order harmonics were generated in a gas tube filled with argon by a loosely focused geometry under a phase-matching condition. The wavefront distortions for the driving laser were corrected by a deformable mirror with a Shack-Hartmann sensor to significantly improve the extreme ultraviolet radiation conversion efficiency due to the excellent beam profile at focus. A high-damage-threshold beam splitter is demonstrated to eliminate energetic driving laser pulses from high-order harmonics. The extreme ultraviolet pulse energy is measured to be 0.3 microjoule at the exit of the argon gas target. The experimental facilities developed will lead to the generation of microjoule level isolated attosecond pulses and the demonstration of true atto pump-atto probe experiments in near future. Finally, in experiment, we show the first demonstration of carrier-envelope phase controlled filamentation in air using millijoule-level few-cycle mid-infrared laser pulses.

ACKNOWLEDGMENTS

I would like to thank my PhD advisor, Professor Zenghu Chang, for supporting me during these past years. He's one of the smartest professors I know. I hope that I could be as enthusiastic, and energetic as him. Dr. Chang has provided insightful scientific advice, discussions and knowledge about research. I would like to thank the members of my PhD committee, Prof. Shin-Tson Wu, Prof. David J. Hagan and Prof. Haripada Saha for their helpful advice and suggestions in general. I also acknowledge the support staff of UCF, including (but certainly no limited to) Rachel Franzetta, Jessica Brooks, Monika Crittenden, Robert Wong, and Elizabeth Rivera. I was lucky to have many excellent colleagues with whom to gain experience: Dr. Yi Wu, Dr. Kun Zhao, Dr. Michael Chini, Dr. Qi Zhang, Dr. Eric Cunningham, Dr. Jialin Li, Dr. Xiaowei Wang, Dr. Yan Cheng, Dr. Xiaoming Ren, Dr. Yanchun Yin, Dr. Fengjiang Zhuang, Dr. Seunghwoi Han, Dr. Krishna Murari, Dr. Huaping Zang, Jie Li, Tianyi Guo, Andrew Chew, Shuyuan Hu and Lam Mach. I appreciate all their kinds of support and helpful discussions. It is my honor to work with several former colleagues and friends during the first year in Kansas. They are Dr. Junliang Xu, Dr. He Wang, Dr. Steve Gilbertson, Dr. Sabih Khan, Dr. Shouyuan Chen, and Dr. Baozhen Zhao. Finally, I would like to acknowledge all my relatives, friends, family members and especially my parents, wife Jiong Deng and my baby Shutong Wang. This work truly would not have been accomplished by me without their support over the past few years. These past seven years have not been an easy ride, academically and personally. My wife has been a true and great supporter for me and has unconditionally loved me all the time. There are no words to convey how much I love her.

TABLE OF CONTENTS

LIST OF FIGURES

LIST OF TABLES

CHAPTER 1 - INTRODUCTION

Since the invention of the laser, significant progress has been made in developing shorter and more intense light sources [1-3]. The reduction of the pulse duration and the maintenance of high power laser have driven many areas of physics over the past decades [4]. The high intensity femtosecond (1 fs=10^{-15} s) lasers were always beneficial to atomic, molecular, and optical research but electron dynamic processes which occur on attosecond (1 as = 10^{-18} s) timescales could not be imaged [5]. Thus, to image any electron dynamics process in atoms or molecules, a light pulse faster than the process itself is required to prevent blurring of the image. For example, the time it takes for an electron in the first Bohr orbit to travel a Bohr radius is ~27.2 as [6]. This timescale is out of the reach of the shortest laser pulses ever produced directly by any laser amplifier in the world. A new method was required to reach attosecond pulse durations, which were created by way of high harmonic generation (HHG) [7]. When a high power laser is focused into a rare gas target with an intensity of ~ 10^{13} - 10^{15} W/cm^2, a series of odd order harmonics of the fundamental driving pulse is produced, which is the generation of high harmonics [8]. HHG is recognized as a very attractive coherent short-wavelength light source, being applied to many research areas such as attosecond sciences, plasma physics, high-resolution imaging, spectroscopy and nonlinear optics in the extreme ultraviolet (XUV) region [9-11]. However, currently, the energy of available XUV pulses is limited by the low conversion efficiency and the energy of the driving laser [12]. For the further development of various applications, the most important issue is attosecond pulse energy scaling.

1.1 The Principle of High-order Harmonic Generation

HHG process has been studied extensively in recent years. It was first discovered by M. Ferray etc. in 1988 [8]. By interacting intense femtosecond lasers with a gas or solid target, high harmonics can be generated. In experiments, this is usually realized by focusing a femtosecond laser into a noble gas cell. The HHG process can be understood with a three step model theory which was developed in 1993 [13]. It is a semi-classical re-collision model as shown in Fig. 1.1 [1].

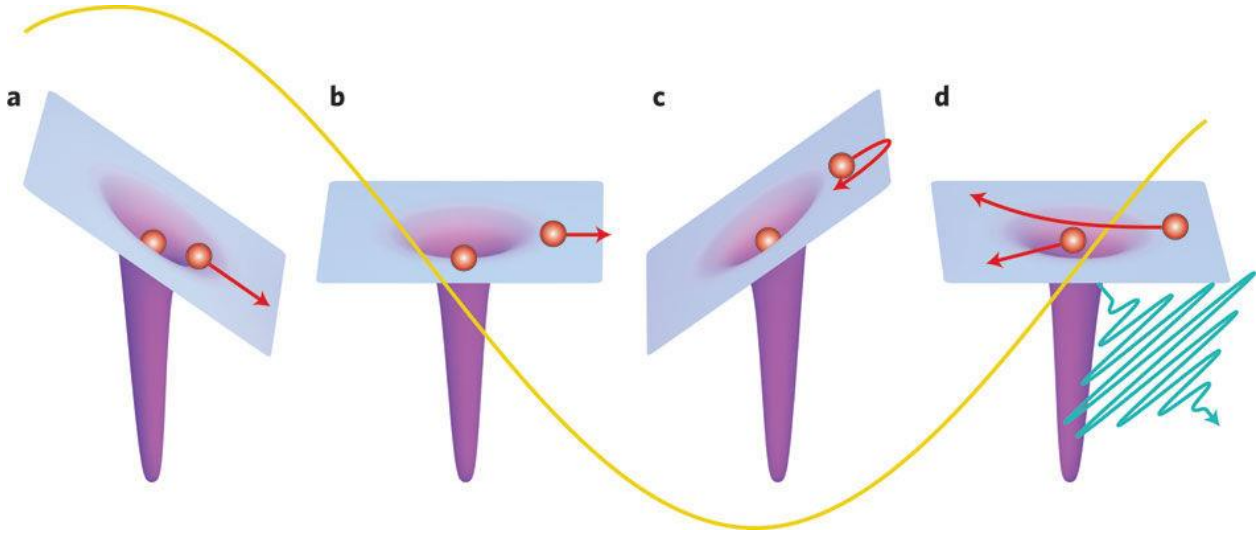

Figure 1.1 The three step model for HHG (adapted from [1]).

A ground-state bound electron in an atomic potential can tunnel through the atomic potential when the intense femtosecond near-infrared pulses (yellow line) are applied. First, the electron is pushed away from an atom near the peak of laser field (a) and accelerated (b). When the laser field reverses, the electron can be driven back (c). Then the electron recombines with its

parental ion, and a photon is produced (d). When the following two conditions are met, this process can be treated classically after the electron is free from the atom or molecules: (i) the electron in the continuum states is no longer affected by the coulomb interaction of the atom, (ii) only the ground state of the atom contributes to the evolution of the process. This is true in the non-perturbative regime where the Keldysh parameter, γ, is much less than 1 [14]. Here, γ is given by the following equation:

$$\gamma = \sqrt{\frac{2I_P m\omega^2}{e^2 E_0^2}} \tag{1-1}$$

where I_p is the ionization potential of the atom, e and m are the electron charge and mass, respectively, E_0 is the laser field amplitude, and ω is the laser frequency [15]. After tunneling, the electron will travel some distance away from the parent ion and when the electric field of the laser switches sign, the electron will reverse direction and return. The kinetic energy (K.E.) of the electron is given by:

$$\text{K.E.} = 2U_P(t)[\sin(\omega t_f + \varphi) - \sin(\omega t_0 + \varphi)]^2 \tag{1-2}$$

where t_f is final recombination time, t_0 is the electron born time and φ is the carrier-envelope phase (CEP) of the laser [16]. U_p (t) is the ponderomotive energy which is a cycle-averaged kinetic energy of the electron "quivering" in the electric field. U_p (t) is given by:

$$U_p\,(t) = \frac{e^2 E_0(t)^2}{4m\omega^2} \tag{1-3}$$

The electron has a probability of recombining with its parent ion after propagating in the laser field. The electron releases all the kinetic energy it gained in the form of a harmonic pulse once it returns to its ground state. The energy of the photons produced depends on the time the

electron was born in the electric field. The maximum kinetic energy of electrons can reach is $3.17U_p$, so the highest energy photon (E_{cutoff}) possibly released is [17]:

$$E_{cutoff} = I_p + 3.17\frac{e^2E_0(t)^2}{4m\omega^2} \sim I_L\lambda_L^2 \quad (1\text{-}4)$$

Here I_L is the laser intensity and λ_L is the laser wavelength. This implies that if the intensity or wavelength of the driving laser is increased, the cutoff is increased as well. Since the tunneling, propagation, and recombination occurs once per half laser cycle, it means for a multi-cycle pulse, a train of attosecond pulses is produced with every half an optical cycle.

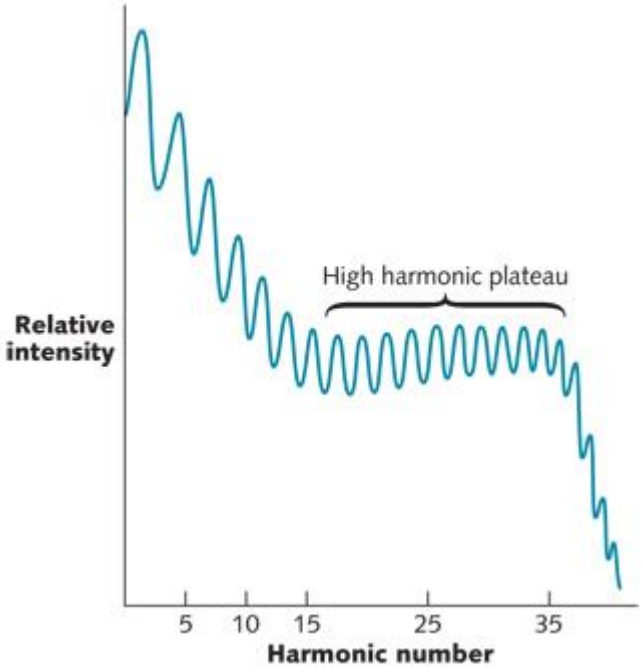

Figure 1.2 A typical HHG spectrum. After the fast decreasing of HHG signal in the low energy domain, a plateau region with comparable intensity was followed by a cutoff [18].

A typical HHG spectrum is illustrated in Fig. 1.2. The energy for each harmonic drops at low frequencies, but levels out in a plateau of successive harmonics with similar energy before eventually dropping to the far end (cut off).

1.2 Experimental Setup and Measurement of HHG

Figure 1.4(a) shows an extreme-ultraviolet (XUV) generation and spectrometer capable of producing and measuring the spectrum of emitted HHG [19]. A 30 fs, multi-cycle 800 nm laser pulse is focused by an f=300 mm focal length plano-concave mirror with an anti-reflection coating into a 1.6 mm long gas target, which is a glass cell with two laser drilled holes in it. The gas cell is usually filled with either argon, neon or xenon at pressures on the order of 10 torr. The excess gas is evacuated from the generation chamber with turbos and roughing pumps. A train of attosecond pulses is generated (see Fig. 1.4(b)) as long as the laser intensity reaches the order of 10^{13}-10^{14} W/cm^2. The high-intensity pump pulse is co-propagating with the HHG. It is necessary to reduce the intensity of the driving laser to less than a hundred gigawatts per square centimeter to avoid damaging the following optical components. A thin (~200 nm) aluminum (Al) filter is used to remove the residual driving laser, leaving only the XUV photons. It also partially compensates the intrinsic atto-chirp [20]. The transmission range of this Al filter covers from 15 eV to 71 eV, corresponding from the 9th to 45th harmonics of the driving laser as shown in Fig. 1.3 [21].

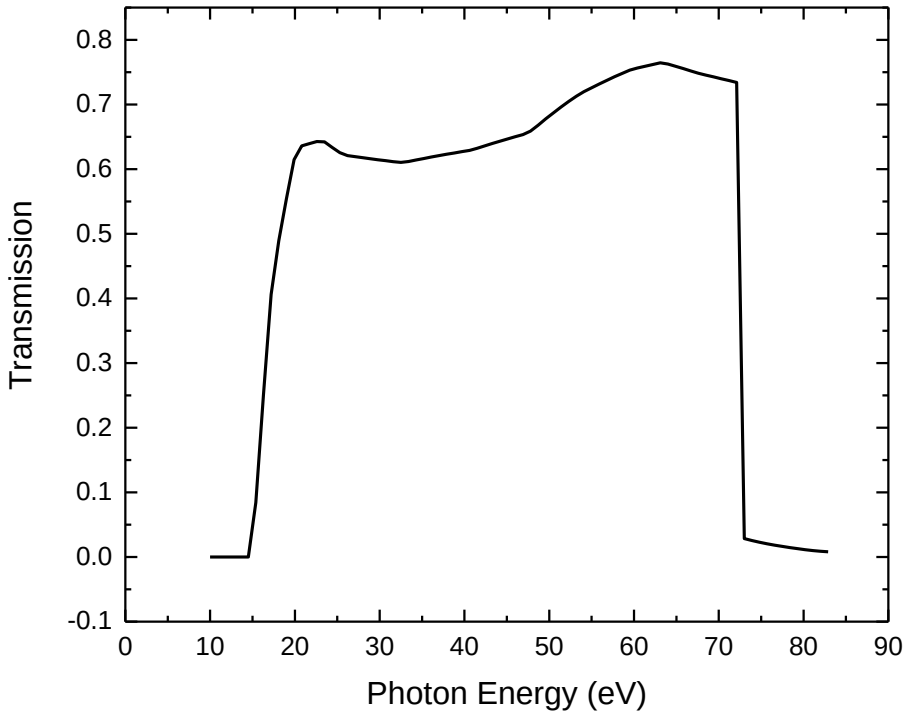

Figure 1.3 The transmission for a 200 nm Al filter as a function of the XUV photon energy.

After the filter, an XUV photodiode could be placed into the beam line to measure the total XUV photon flux. Then, the harmonics were incident on a toroidal grating. The dispersed XUV hit a microchannel plate (MCP) detector with ~1200 V applied and a phosphor screen with ~2000 V applied. The image of the spectrum was recorded by a CCD camera behind the screen.

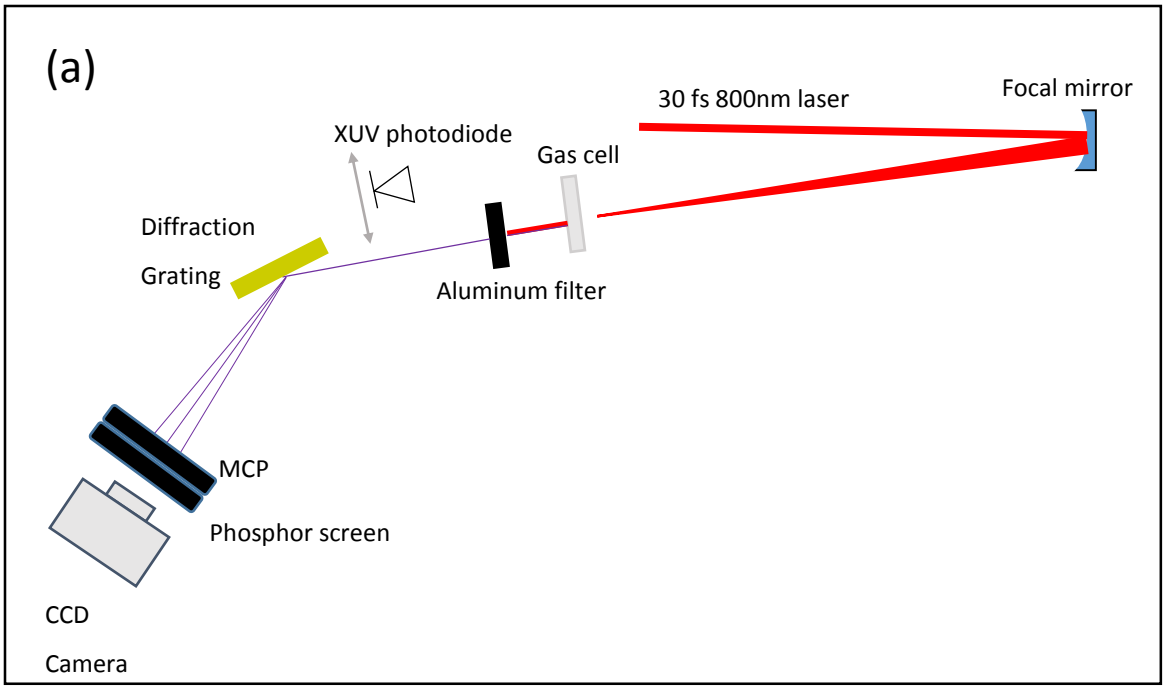

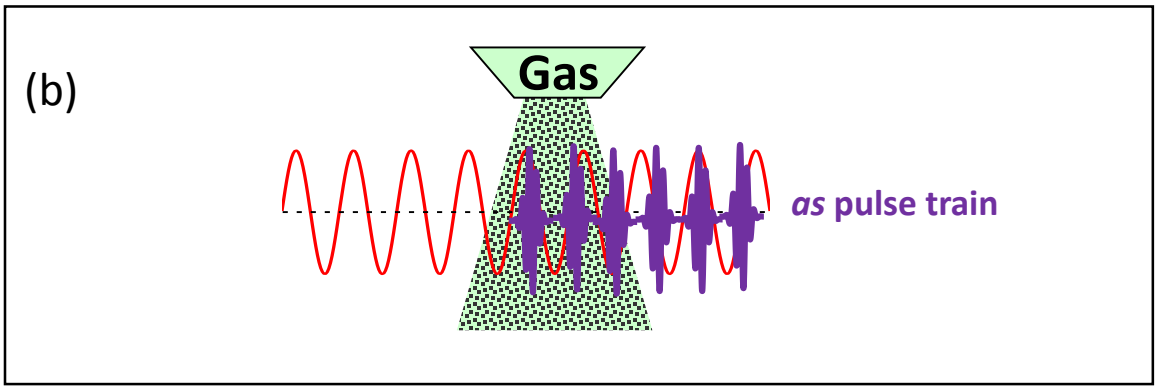

Figure 1.4 (a) XUV Spectrometer, (b) Attosecond pulse train from a gas target.

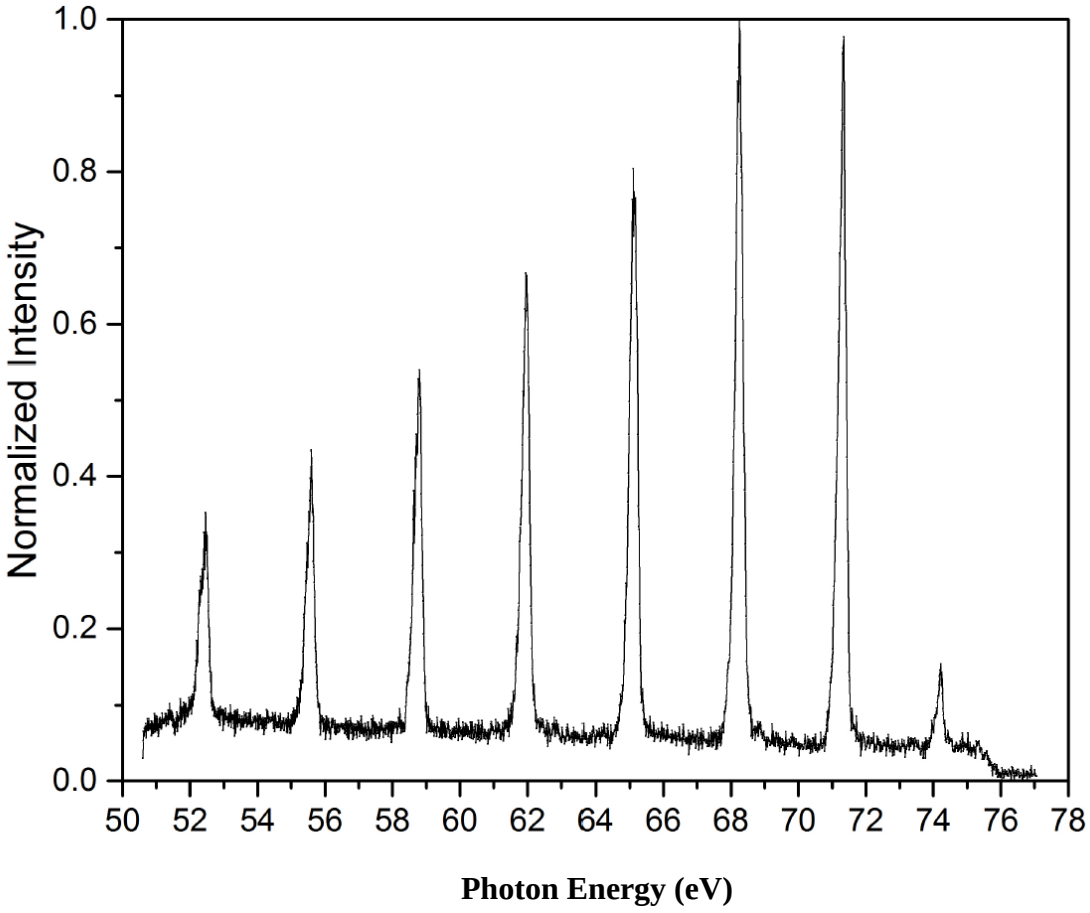

Figure 1.5 A typical HHG spectrum of helium gas by a 30 fs linearly polarized driving laser.

Figure 1.5 depicts an HHG spectrum generated from a helium gas target under this experimental condition. Ammosov-Delone-Krainov (ADK) theory was developed to calculate the ionization probability of atoms in the intense laser field. The ionization only occurs within a fraction of one optical cycle. The average ionization rate is given in atomic units by [22]:

$$W(t) = I_p |C_{n^* l^*}|^2 G_{lm} \left(\frac{4(2I_p)^{3/2}}{E(t)} \right)^{2n^* - |m| - 1} e^{\frac{2(2I_p)^{3/2}}{3E(t)}} \tag{1-5}$$

where the coefficients are given by:

$$|C_{n^*l^*}|^2 = \frac{2^{2n^*}}{n^*\Gamma(n^* + l^* + 1)\Gamma(n^* - l^*)} \tag{1-6}$$

$$G_{lm} = \frac{(2l+1)(l+|m|)!}{(2^{|m|}|m|!\,(1-|m|)!} \tag{1-7}$$

where I_p is the ionization potential of atoms or molecules. The n* is the effective principle quantum number, given as:

$$n^* = \frac{Z}{\sqrt{2I_p}} \tag{1-8}$$

Here, Z is the atomic core charge and m is the projection of the angular momentum on the electric field. And l* is the effective angular momentum quantum number. So, the ionization probability is calculated as:

$$P(t) = 1 - \exp(\int_{-\infty}^{t} W(t')dt' \tag{1-9}$$

As an example, Figure 1.6 depicts the ionization probability for the argon gas. The pulse duration is 40 fs and the intensity is 2×10^{14} W/cm^2.

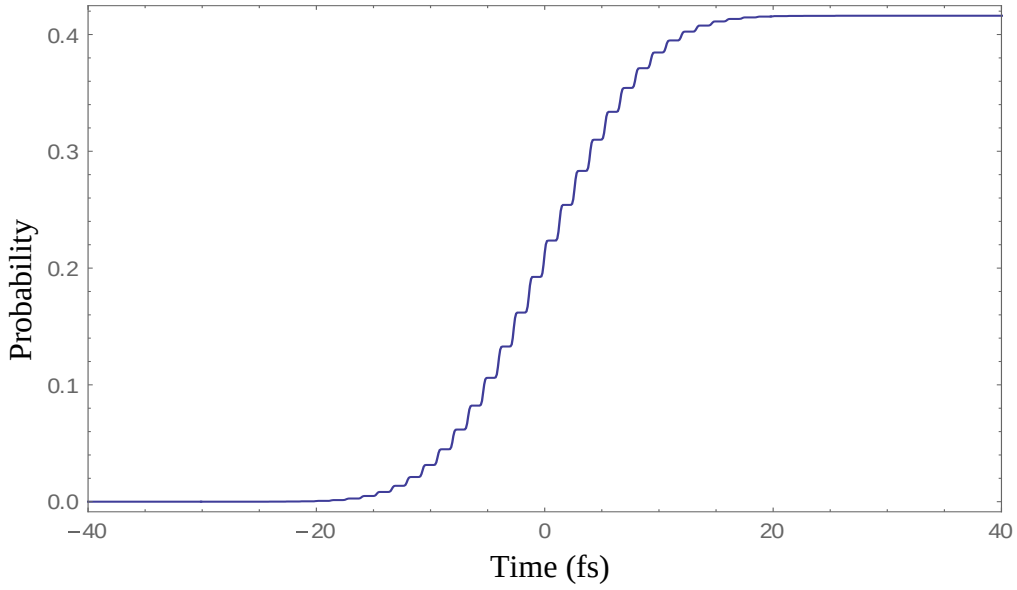

Figure 1.6 ADK calculation for ionization probability for argon gas with a laser intensity of 2×10^{14} W/cm^2.

1.3 High-flux Attosecond Pulses

Attosecond pulses generated by the interaction of the ultrafast high power laser with atoms as discussed previously are recognized as a very attractive coherent short-wavelength light source [23]. Great interests have been aroused recently to study the interaction of intense XUV radiations with atoms and molecules thanks to the rapid development of different intense coherent XUV sources such as the free electron laser [24], the plasma x-ray laser [25] and high-order harmonics [26]. In the next few years, attosecond time-resolved measurements will address key advances in materials science that are of great interest to scientists [27, 28]. The physical phenomena induced by these intense XUV pulses are expected to be much different from those by visible or infrared pulses since the electron quiver energy and the average electron energy gained in the electric field

are proportional to the square of the driving laser wavelength. Attosecond techniques will also be used to unravel the dynamics of phase transitions in strongly correlated materials, providing new insights into metal-to-insulator transitions (MIT) in these materials that will provide rapid switching of optical transmission and novel developments in high speed electronics with much lower power consumption [20, 28, 29].

Recent progresses include the observation of He^{2+} ions generated by a nonlinear interaction between helium atoms and photons with an energy of 42 eV which are generated by the 27^{th} HHG [30]. Also, experiments perform an illustration of two-photon double ionization of neon atoms by using an intense attosecond pulse train (APT) where both direct and indirect sequential mechanisms are allowed [31].

Figure 1.7 shows the theoretical attosecond pump probe demonstration with its application to detect ultrafast electron motions inside atoms or molecules [32]. A ground state helium atom is pumped firstly by an XUV pulse with a 500 as pulse duration. One of the two ground-state electrons is excited into 1s2p state of He. After pumping, the excited electron wave packet periodically moves between the outer turning point and its nuclear core while the inner electron wave packet remains close to the nucleus. The two electrons' correlation mainly depends on their relative separation, and this correlation can be screened by a probing ultrashort attosecond pulse with a pulse duration of 250 as. If the outer electron has a large separation from the nucleus, the core electron will absorb most of the XUV photon energy and leaves the atom quickly. The outer electron will experience a "shake-off'' process. If the attosecond probe occurs when the outer-electron is very close to the core, the two electrons will share the XUV photon energies and will be "kicked out" from the helium atom at the same time [32]. So, by varying the time delay between the attosecond pump and probe, it is expected to "image" the electron correlation by measuring

the energy sharing between the two ejected electrons from atoms. Although these demonstrated performances open up theoretical possibilities, it is very hard to carry out true pump-probe experiments due to the limitation of the attosecond pulse energy. To sum up, there are three reasons why pump-probe technology is still inaccessible to attosecond science: (1) Attosecond pulses are inefficiently generated using relatively low energy drivers. (2) The isolated attosecond pulses are only generated with 800 nm driving lasers, which limits the x-ray photon energy to less than 150 eV and (3) The focal properties of attosecond pulses have not been optimized and the opportunity for micron focusing of the short wavelength attosecond pulses has never been exploited.

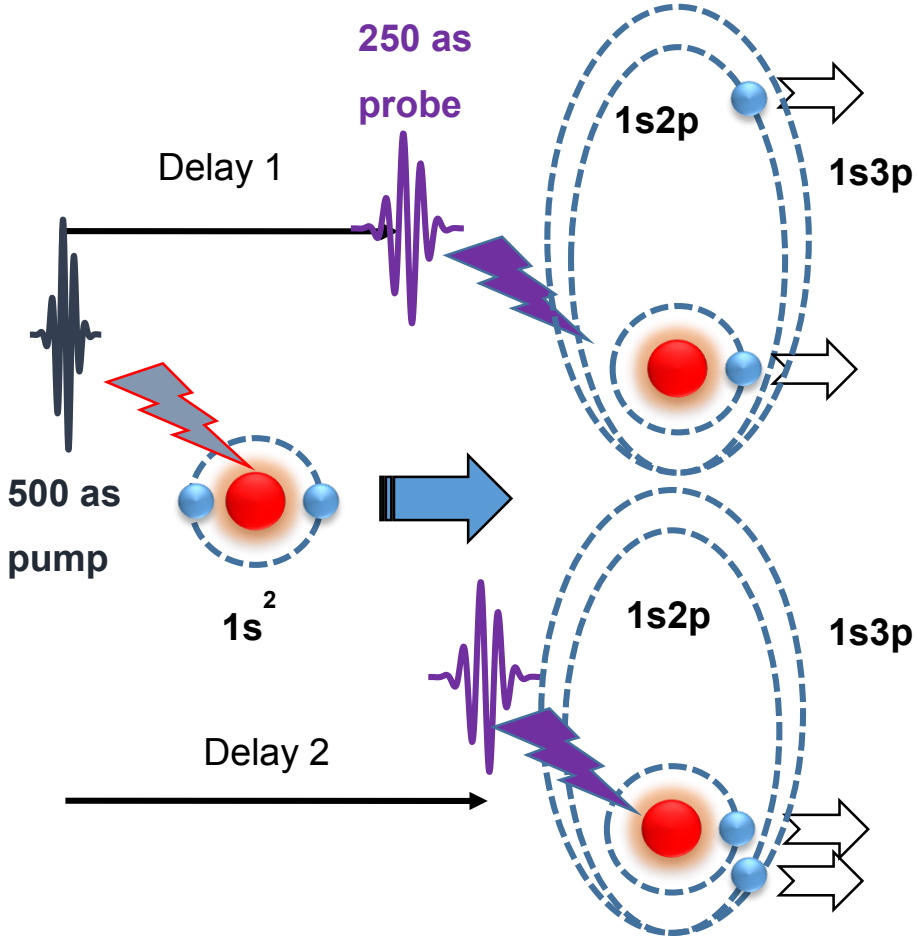

Figure 1.7 Schematic diagram of the attosecond pump probe for helium.

CHAPTER 2 - ISOLATED ATTOSECOND PULSE GENERATION

This chapter will give an overview of the gating techniques for generating isolated attosecond pulses: amplitude gating, polarization gating, two color gating, double optical gating and generalized double optical gating.

2.1 Amplitude Gating

Photoionization confined to a single wave cycle contributes to high-harmonic generation which can be related to electron trajectories with a known timing to the driving laser field. From the three-step process discussed in chapter one, the most straightforward way is to use a driving pulse of a single-cycle duration [33]. A 3.3 fs driving laser was used, which corresponded to sub-1.5-cycles as shown in Fig. 2.1.

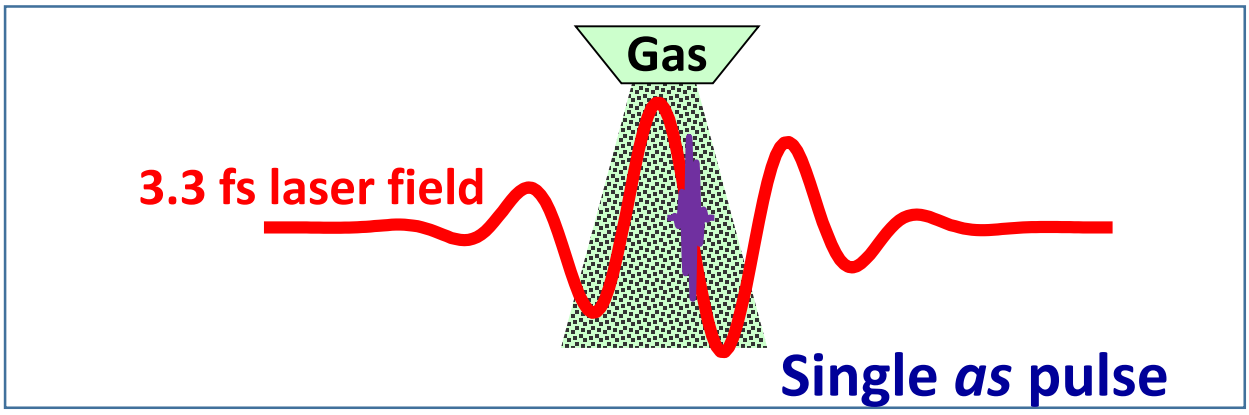

Figure 2.1 Single attosecond pulse generation by few cycle lasers.

With this amplitude gating (AG) method, 80 as isolated pulses were generated. But this method limits the achievable pulse bandwidth for the super continuum and hence the pulse duration since the zirconium filter was applied to filter out the low energy components, and only the cutoff region makes contribution to the final single attosecond pulse.

2.2 Polarization Gating

The HHG process shows the strong ellipticity dependence on the driving laser field [34]. This can gate a single pulse from an attosecond pulse train, which can be explained by the three-step model. For the last step, the electron driven by a linearly polarized intense field returns to the parent ion. However, the electron can be steered away from the parent ion if an ellipticity is introduced to the driving field, resulting in no recombination, and no attosecond emission due to an acceleration in a transverse direction for the electron. Thus, the harmonic efficiency drops off quickly [35]. This effect can be maximized for circularly polarized fields and the electron will never return to the parent ion. This opens another method to generate single isolated attosecond pulses without single-cycle driving lasers [36]. It relaxes the extremely difficult requirement of amplitude gating [37]. In experiment, by combination of a right and left circularly polarized laser pulse with a time delay, T_d, between them, an electric field with a small linear portion in the center is generated [38-40]. At the same time, it also has the circularly polarized leading and trailing edges as shown in Fig. 2.2.

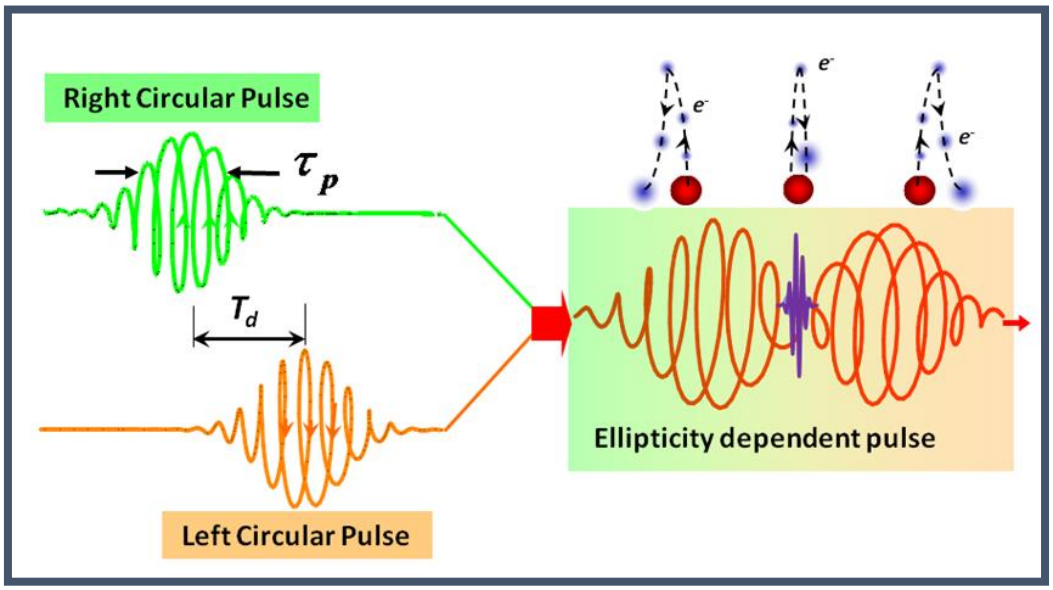

Figure 2.2 The right and left circularly polarized pulses and the PG gating field.

This gates an isolated single pulse from an attosecond pulse train since it only allows attosecond pulses to be produced within the central linearly polarized portion of the driving laser filed. The superimposed electric field is given by:

$$\overrightarrow{E(t)} = E_{drive}(t)\hat{i} + E_{gate}(t)\hat{j} \tag{2-1}$$

The driving field E_{drive} is given by:

$$E_{drive}(t) = E_0[(e^{-2In2\frac{(t+\frac{T_d}{2})^2}{\tau_p^2}} + e^{-2In2\frac{(t-\frac{T_d}{2})^2}{\tau_p^2}})\cos(\omega_0 t + \varphi_{CE})] \tag{2-2}$$

And the gating field E_{gate} is given by:

$$E_{gate}(t) = E_0[(e^{-2In2\frac{(t+\frac{T_d}{2})^2}{\tau_p^2}} - e^{-2In2\frac{(t-\frac{T_d}{2})^2}{\tau_p^2}})\sin(\omega_0 t + \varphi_{CE})] \tag{2-3}$$

where E_0 is the amplitude of the circularly polarized laser field, ω_0 is the frequency, φ_{CE} is the CE phase and τ_p is the pulse duration. Figure 2.3 demonstrates the three dimensional frame for the electric fields.

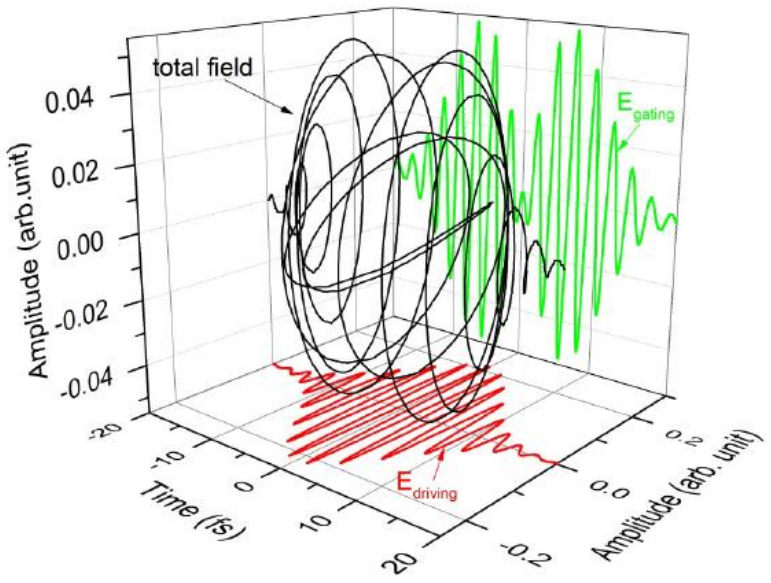

Figure 2.3 A three dimensional frame for the PG electric field. The black line represents total field. The red (driving field) and green lines (gating field) are projections on two orthogonal planes.

The ratio of the magnitude of the gating field and the driving field yields the time dependent ellipticity:

$$\xi(t) = \frac{|E_{gate|}}{|E_{drive}|} = |\frac{1 - \mathrm{e}^{\frac{-4\mathrm{t}T_d \mathrm{In}2}{\tau_\mathrm{p}^2}}}{1 + \mathrm{e}^{\frac{-4\mathrm{t}T_d \mathrm{In}2}{\tau_\mathrm{p}^2}}}| \tag{2-4}$$

The Taylor expansion of the center of the electric field can be calculated and approximately yields the term:

$$\xi(t) = |2\mathrm{In}(2)\frac{T_d}{\tau_p^2}t| \tag{2-5}$$

where the laser is approximately linearly polarized. For maximizing the HHG flux, a gate width is attained and can be written as:

$$\delta t_G = \frac{\xi_{th}}{\mathrm{In}(2)}\frac{\tau_p^2}{T_d} \tag{2-6}$$

where ξ_{th} is defined as the threshold ellipticity for harmonic generation. The experimental setup is shown in Fig. 2.4.

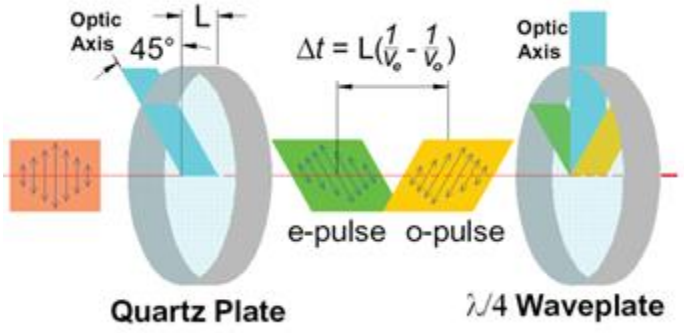

Figure 2.4 Optical Components for polarization gating.

A birefringent quartz plate which has its optical axis oriented at 45^0 with respect to the input polarization is used to generate the left and right polarized pulses (o- and e- pulses) and also gives a time delay between the two components. After that, a zero order quarter waveplate is introduced with its optical axis parallel to the input laser polarization. So, this causes the linear polarization in the center of the combined laser field. An isolated attosecond pulses as short as ~130 as were generated by this method [41]. The major disadvantage for PG is that the leading

and trailing edges of the pulse deplete the ground state of the target gas and in fact they do not contribute to the HHG process. Therefore, a large portion of the input laser pulse energy is wasted and it significantly reduces the conversion efficiency.

2.3 Two Color Gating

As was discussed before, a laser focused into a gas target will generate a HHG spectrum of odd orders. Mathematically this is due to the Fourier transform of the pulses train separated by half an optical cycle of the driving laser and this will generate odd multiples of the driving laser frequency. Physically it can be explained by the fact that the symmetry of the isotropic rare gas is centrosymmetric [42]. If the symmetry is broken, like in a BBO crystal, even orders can also be generated. Instead of breaking the symmetry of an isotropic gas, it is, of course, much easier to break the symmetry of the driving laser [43]. This can be achieved by adding a weak, linearly polarized second harmonic field to the fundamental driving laser [44]. Every other half cycles are slightly enhanced while the other cycles are reduced between the two pulses. This slight change to the driving laser field can drastically change the HHG spectrum considering the high intensity and nonlinearity [45, 46]. The time dependent electric field is given by the equation:

$$E(t) = E_0 \cos(\omega t + \varphi_{CE}) + aE_0 \cos(2\omega t + 2\varphi_{CE} + \phi) \qquad (2\text{-}7)$$

where a is ratio of the amplitude of the second harmonic to the fundamental laser, φ_{ce} is the CE phase and Φ is the relative phase between the second harmonic and fundamental. Figure 2.5 shows the fundamental, second harmonic and total electric field distributions.

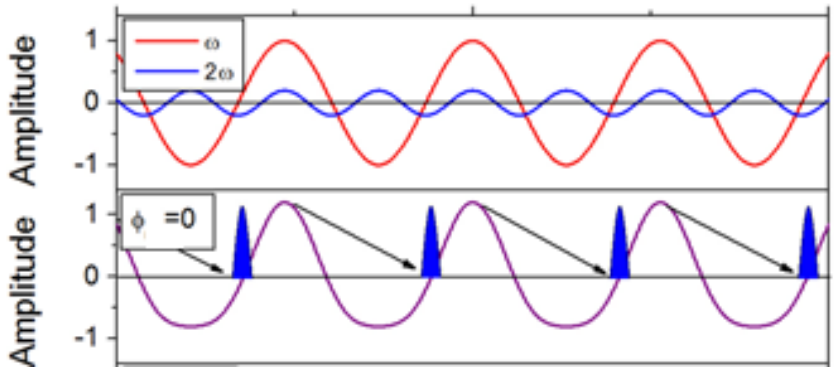

Figure 2.5 Two-color gating electric field: (a) Individual fields, (b) Combined fields.

If the second harmonic intensity is strong enough, every other cycle will not have the sufficient intensity to produce an attosecond pulse, resulting in a full-cycle period between pulses. Unfortunately, in experiment, satellite pulses are not many orders of magnitude below the main pulse. So, two-color gating alone will not guarantee true isolated attosecond pulse generation.

2.4 Double Optical Gating

From the above two sections, it is very obvious that both two-color gating and polarization gating have serious disadvantages with them, respectively. However, combining these two methods, it may overcome the limitations of these two gating methods and makes a robust method for the generation of an isolated attosecond that can be daily attained in the lab. Double optical gating (DOG) is developed by a combination of two gating methods to produce the broad spectra and single attosecond pulses [47]. Another disadvantage for both PG and the two color gating technique is that it requires a few-cycle driving laser with a precisely controlled CE phase for

generating single attosecond pulses [44]. The requirement of CE phase stabilization for few cycle driving laser put a restriction for the attosecond science research. DOG can reduce this requirement, thus favoring isolated attosecond pulse generation. The driving field for DOG is now given by:

$$E_{drive}(t) = E_0[(e^{-2In2\frac{(t+\frac{T_d}{2})^2}{\tau_p^2}} + e^{-2In2\frac{(t-\frac{T_d}{2})^2}{\tau_p^2}})\cos(\omega_0 t + \varphi_{CE}) + ae^{-2In(2)\frac{t^2}{\tau_{2\omega}^2}}\cos(2\omega_0 t + 2\varphi_{CE} + \phi)] \quad (2\text{-}8)$$

where $\tau_{2\omega}$ is the pulse duration of the second harmonic field.

The gating field is described as:

$$E_{gate}(t) = E_0[(e^{-2In2\frac{(t+\frac{T_d}{2})^2}{\tau_p^2}} - e^{-2In2\frac{(t-\frac{T_d}{2})^2}{\tau_p^2}})\sin(\omega_0 t + \varphi_{CE})] \quad (2\text{-}9)$$

Figure 2.6 (a) shows the total laser field for DOG. A weak second harmonic field is induced to the driving field and distorts the electric fields slightly compared with the PG fields. The orthogonal fields for DOG are shown in Fig. 2.6 (b). The DOG fields (red line) is the combination of the SH field (purple line) and PG field (black line).

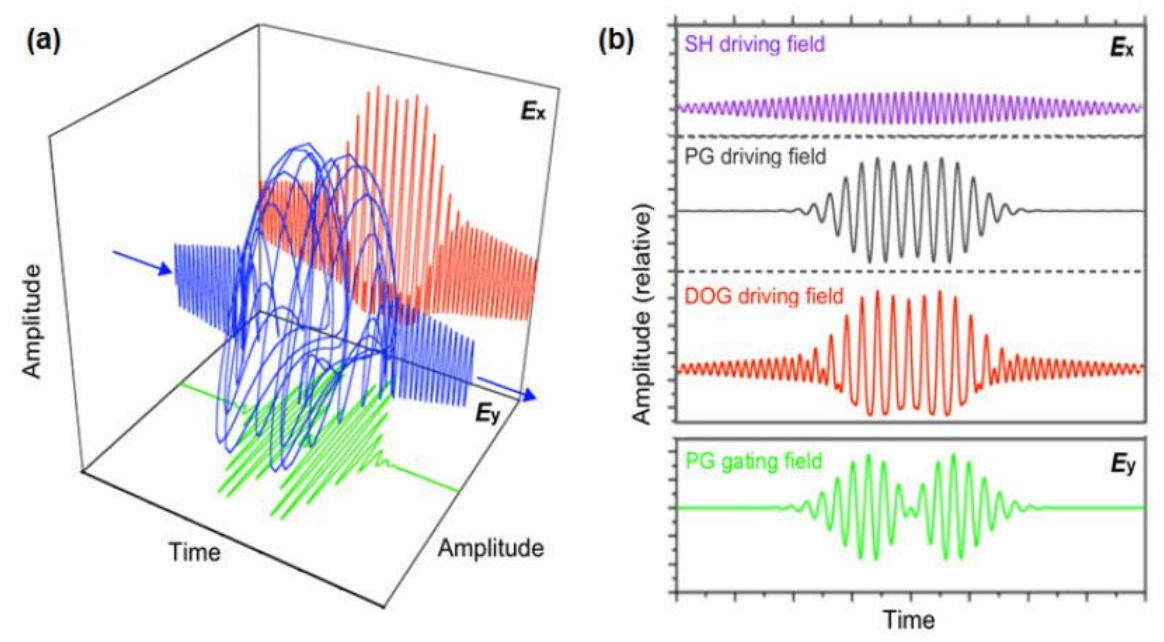

Figure 2.6 (a). 3-D image for the DOG fields, (b). SHG field (purple line), Driving field (black line), DOG field (red line) and Gating field (green line).

From the gate width equation (2.6), it can be concluded that if the gate width is one optical cycle, the pulse duration can be increased compared to half-cycle gate widths. This relaxes the requirement for the driving laser pulse duration. So, DOG allows much longer pulse durations to be used. This is one of the major advantages for DOG since longer pulse durations are much easier to generate in the lab for a daily operation [48].

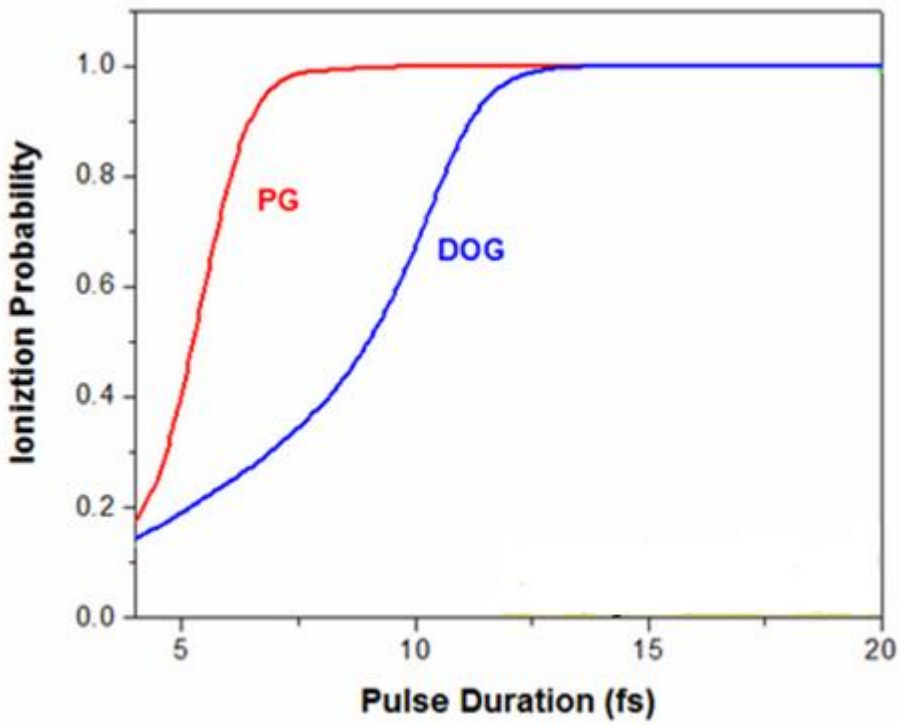

Figure 2.7 Ionization probabilities for DOG and PG by ADK calculation.

The ADK calculation for ionization probabilities is shown in Fig. 2.7. The ionization probability for DOG is much less than PG for all the pulse durations which means the target will be less depleted by the leading edges of the laser. As a result, the conversion efficiency will be improved, leading to a higher HHG flux. Besides, the combined field of the right and left circularly polarized pulse for the DOG is stronger than PG at a point. This means there will be higher laser intensity within the gate width as shown in Fig. 2.8. Since the harmonic cutoff is proportional to the laser intensity, DOG can greatly extend the cutoff and broaden the HHG spectrum. Thus, it can support shorter pulses than PG.

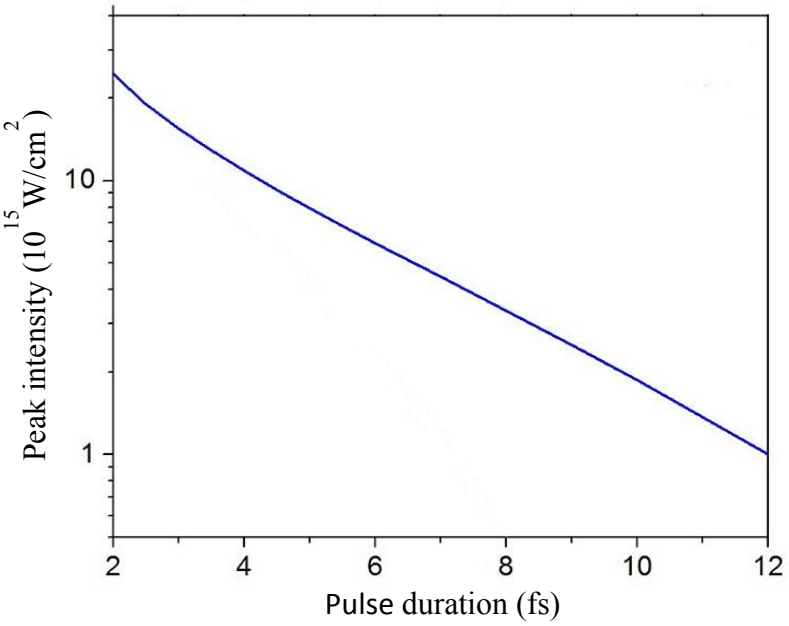

Figure 2.8 Peak Intensity within the gating width for DOG.

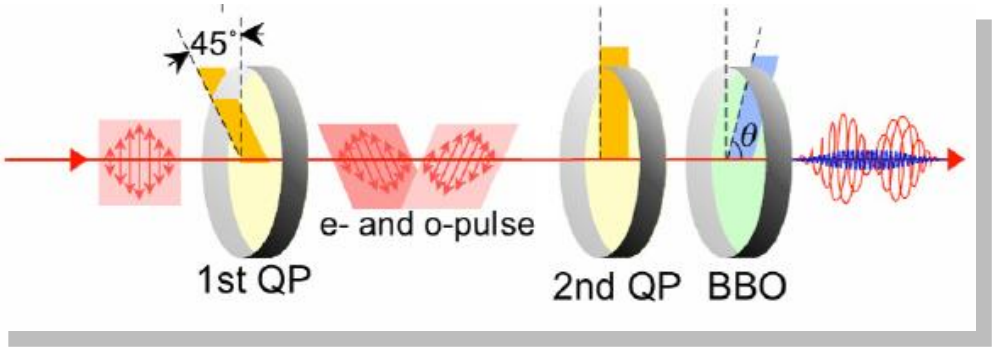

Figure 2.9 Experimental setup for DOG optical components.

The experimental setup for DOG is very close to that for PG except the additional BBO crystal for the second harmonic generation as shown in Fig. 2.9 [49]. The optical axis of the BBO crystal lies 29^0 from the normal, which meets the phase matching condition for the second harmonic generation of the 800 nm fundamental. The first quartz plate works the same as PG. It

separates a linearly polarized input pulse into two orthogonally polarized pulses with a delay. After the first quartz plate, the two e-and o- pulses are incident onto a second quartz plate and then a BBO crystal. The two pulses project onto the optical axis of the second quartz plate and generate two new orthogonal fields: driving and gating fields. The BBO is negative uniaxial and it can cancel some of the delay introduced by the second quartz plate and generate the second harmonics of the fundamental. As a result, they work together as a quarter waveplate. The field components of a driving laser pulse after BBO are shown in Fig. 2.10.

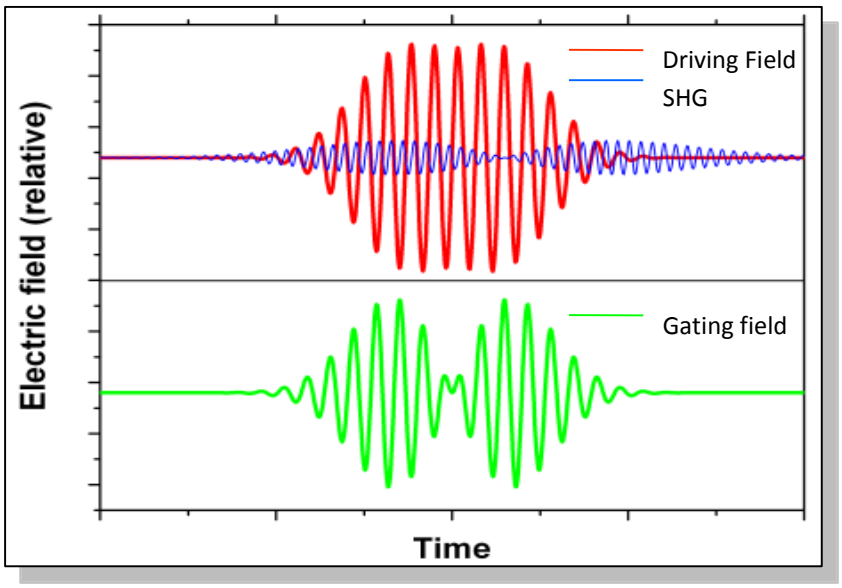

Figure 2.10 Field components for DOG after BBO crystal.

An important point here is how the BBO should be rotated. To fine tune the phase-matching angle, it should be rotated about an axis perpendicular to the input polarization. Since the SHG efficiency is dependent on the intensity of the fundamental laser, its position along the laser

focusing geometry should be optimized. Great care must be taken not to place it too close to the focal point to avoid damaging the crystal.

2.5 Generalized Double Optical Gating

The DOG method still has a disadvantage because it requires a pulse less than 12 fs. The output pulse duration of the Ti:-Sapphire femtosecond laser is usually ~25-35 fs which is too long for DOG to work. A hollow-core fiber and chirped mirrors for spectral broadening and temporal compression are applied to shorten the pulse to a few fs, however this limits the output energy of the driving laser since the coupling efficiency from fiber and chirp mirrors is only ~50%. This implies that the full output energy from the Ti:-Sapphire femtosecond laser system could not be used to scale the attosecond pulse flux to extremely high levels, like the μJ level, which is sufficient for conducting nonlinear attosecond experiments or attosecond-pump attosecond-probe experiments. Therefore, our motivation is to develop a gating method for generating attosecond pulses directly from the driving laser of a high energy output up to J-level without pulse duration limitation. This is of great importance for daily operations in most labs. Due to the depletion of the target gas by the leading edge, it puts a limitation on using longer pulses for generating isolated attosecond pulses. So, a new method to reduce the depletion can improve the efficiency. It can be achieved by changing the ellipticity of the leading edge. This also reduces the requirement on the delay between the two pulses even lower than DOG. This is the main principle of generalized double optical gating (GDOG) [48]. For GDOG, the ellipticity requirement is more general than requiring only circular polarization as with DOG. A factor of ε for ellipticity will be applied to the driving field. The driving field is expressed as [50]:

$$E_{drive}(t) = \varepsilon E_0[(e^{-2In2\frac{(t+\frac{T_d}{2})^2}{\tau_p^2}} + e^{-2In2\frac{(t-\frac{T_d}{2})^2}{\tau_p^2}})\cos(\omega_0 t + \varphi_{CE})] \quad (2\text{-}10)$$

where ε is the ellipticity of the left and right polarized laser pulses that generate the PG fields. For DOG, this equals one as the lasers are circularly polarized. It means DOG is just GDOG with ε = 1. It is worth noting that the second harmonic field terms do not appear here since it is much weaker than the fundamental field. The gating field for GDOG is given by:

$$E_{gate}(t) = E_0[(e^{-2In2\frac{(t+\frac{T_d}{2})^2}{\tau_p^2}} - e^{-2In2\frac{(t-\frac{T_d}{2})^2}{\tau_p^2}})\sin(\omega_0 t + \varphi_{CE})] \quad (2\text{-}11)$$

So, the ellipticity is time dependent and given by:

$$\xi(t) = \min[\frac{1 - e^{\frac{-4tT_d In2}{\tau_p^2}}}{\varepsilon[1 + e^{\frac{-4tT_d In2}{\tau_p^2}}]}, \frac{\varepsilon[1 + e^{\frac{-4tT_d In2}{\tau_p^2}}]}{1 - e^{\frac{-4tT_d In2}{\tau_p^2}}}] \quad (2\text{-}12)$$

The time dependent ellipticity is shown in Fig. 2.11. A Taylor expansion will give an approximation:

$$\xi(t) = \left|2In(2)\frac{T_d}{\varepsilon\tau_p^2}t\right| \quad (2\text{-}13)$$

Solving this equation gives the gating width:

$$\delta t_G = \varepsilon\frac{\xi_{th}}{In(2)}\frac{\tau_p^2}{T_d} \quad (2\text{-}14)$$

where ξ_{th} is the threshold ellipticity for HHG. This equation is very similar to the gate width for DOG. A feature to point out is that driving field is reduced by a factor ε. The gating field remains the same. GDOG pulse still has an elliptically polarized leading and tailing edge.

The experimental setup is shown in Fig. 2.12. Compared with the DOG set up, the only difference is that one Brewster window is placed after the 1st quartz plate. The reflectivities of a Brewster window are shown in Fig. 2.13. It allows for the angle to be tuned to control the amplitude ration between driving and gating fields. Here, we have "s" and "p" polarized pulses. If the laser polarization lies parallel to the plane of incidence, it is called "p-polarized". If the polarization is perpendicular to this plane, it is called "s-polarized". For GDOG, the driving pulse is s-polarized at the Brewster window and the gating pulse is p-polarized.

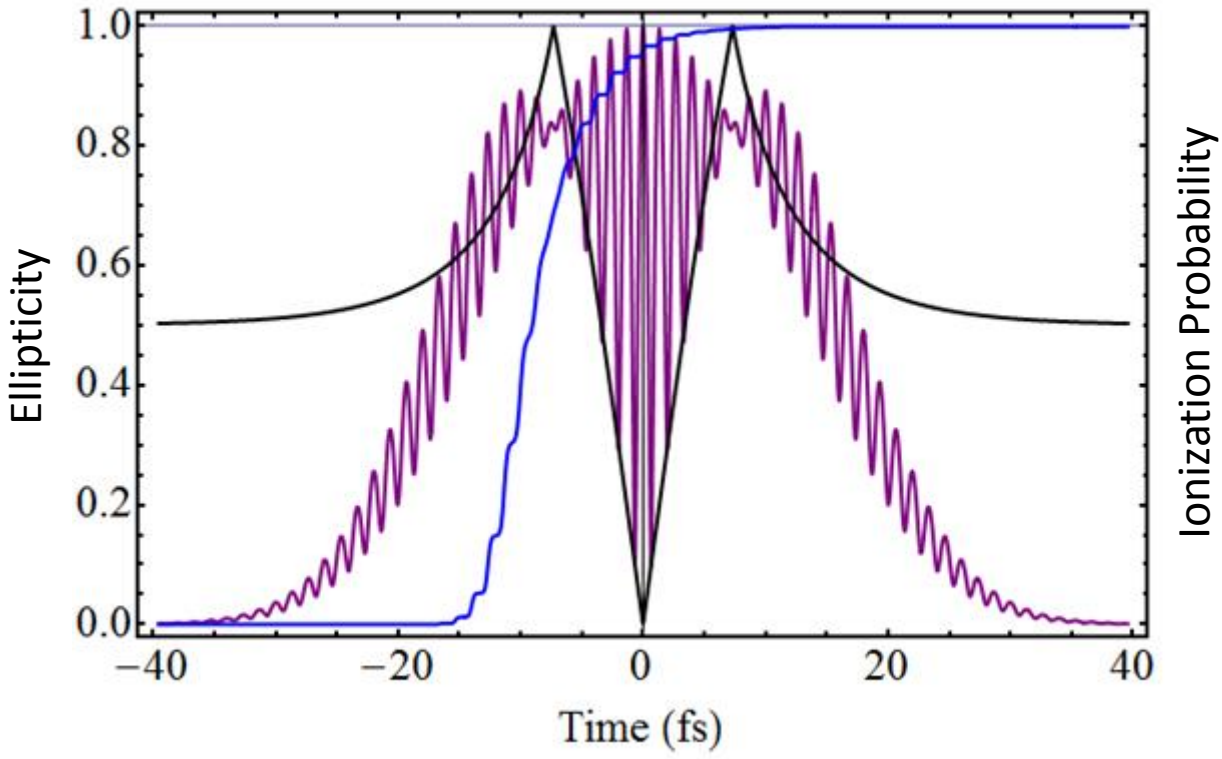

Figure 2.11 GDOG gating field (purple line), The time dependent ellipticity and ADK calculated ionization probability.

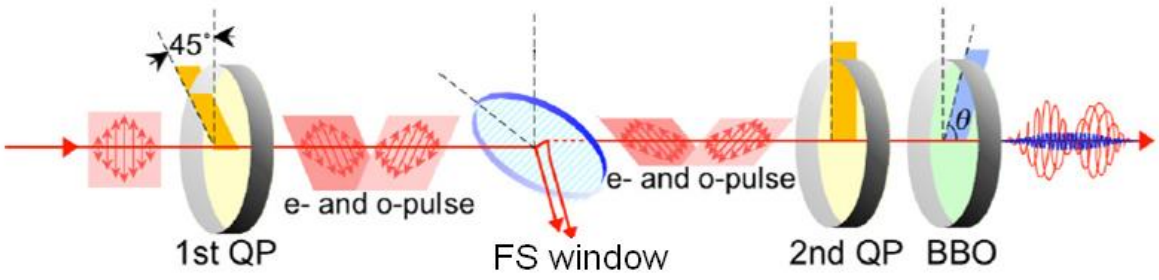

Figure 2.12 Experimental setup for GDOG optics.

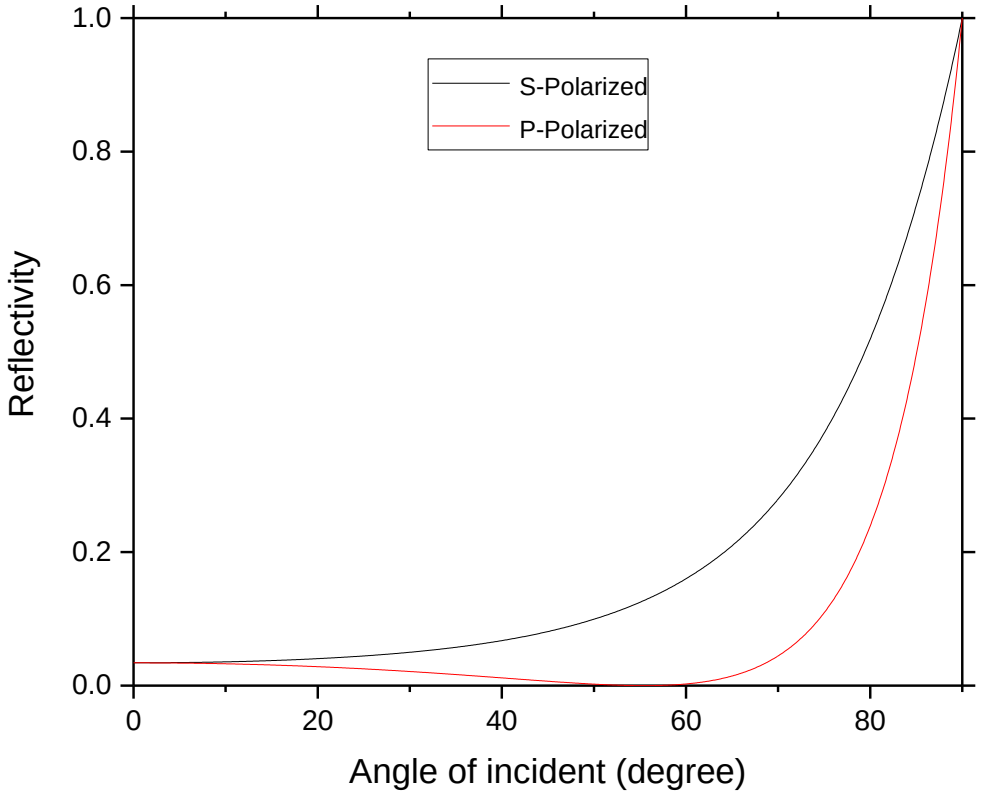

Figure 2.13 Reflectivity versus incident angle for fused silica (SiO_2).

Tuning the window to some angle can change the ratio between the driving and the gating fields and it can provide a method to control the gating width of the GDOG pulse. One of the main advantages for GDOG is that it can further reduce the delay between the two driving and gating pulses so that it will reduce the leading edge depletion for the gas target. Figure 2.14 shows an ADK calculation and comparison for these three gating methods as a function of pulse duration. GDOG definitely works without fully depleting the gas target for pulses longer than 20 fs. It is also worth noting that this GDOG scheme can potentially be driven by a joule-level laser to scale the attosecond flux.

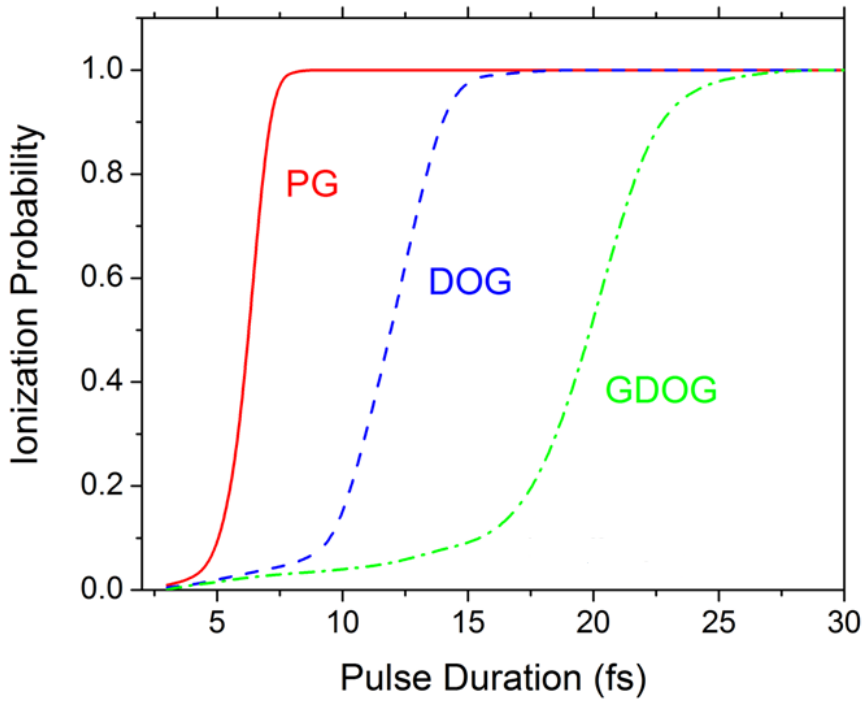

Figure 2.14 ADK calculation for ground state depletion of argon gas target for PG, DOG and GDOG. The laser intensity is 1.9×10^{14} W/cm^2. Argon is used as the gas target.

CHAPTER 3 - THE 100 TW TI:-SAPPHIRE LASER SYSTEM

Currently, the energy of HHG available is limited by both low conversion efficiency and driving laser energies. For the further development of different applications, one of the most important issues is HHG pulse energy scaling. To boost the HHG flux, there are two methods: the first is to increase the conversion efficiency by improving the phase-matching conditions for the HHG process[51]; the second is to boost the driving laser intensity [52]. As a result, a driving laser with a pulse energy up to J-level and a good beam focusability will play an important role for the high flux attosecond generation.

The uniquely designed laser system is capable of delivering 15 fs, 100 TW pulse at a 10 Hz repetition rate [53]. A high-gain amplifier operating at a kHz repetition rate raises the seeding pulse energy from nanojoule (nJ) to millijoule (mJ) level. Then, the mJ-level seeding is boosted by three consecutive power amplifiers working at 10 Hz to a joule level pulse energy.

3.1 Chirped Pulse Amplification

The seeding pulse energy from a mode-locked Ti:-Sapphire oscillator is usually on the order of nJ. To boost the pulse energy to the order of mJ, a gain as high as 10^6 is needed. The pulses should be amplified to a high energy without damaging the optical components or accruing nonlinear effects in the gain medium. To achieve this goal, chirped pulse amplification (CPA) was implemented with the laser pulse being stretched out temporally, resulting in the decrease of the peak intensity to be lower than the damaging threshold of the mirrors and gain medium [54, 55].

3.2 Pulse Stretching and Compressing

In order to avoid damaging, the seeding pulse (pulse duration ~5 fs) from the mode-locked oscillator needs to be stretched before amplification [56]. The seeding pulses are stretched by many orders of magnitude in a CPA system. Then, the stretched out in time pulses were sent to the gain medium to be amplified by a factor of 10^6 or more. The intensity is sufficiently low without causing any damaging but high enough to reach the saturation fluence of the Ti:-Sapphire crystal. Finally, the amplified laser pulses are recompressed back to the seeding pulse width, producing an ultrafast and intense femtosecond laser pulse as illustrated in Fig. 3.1.

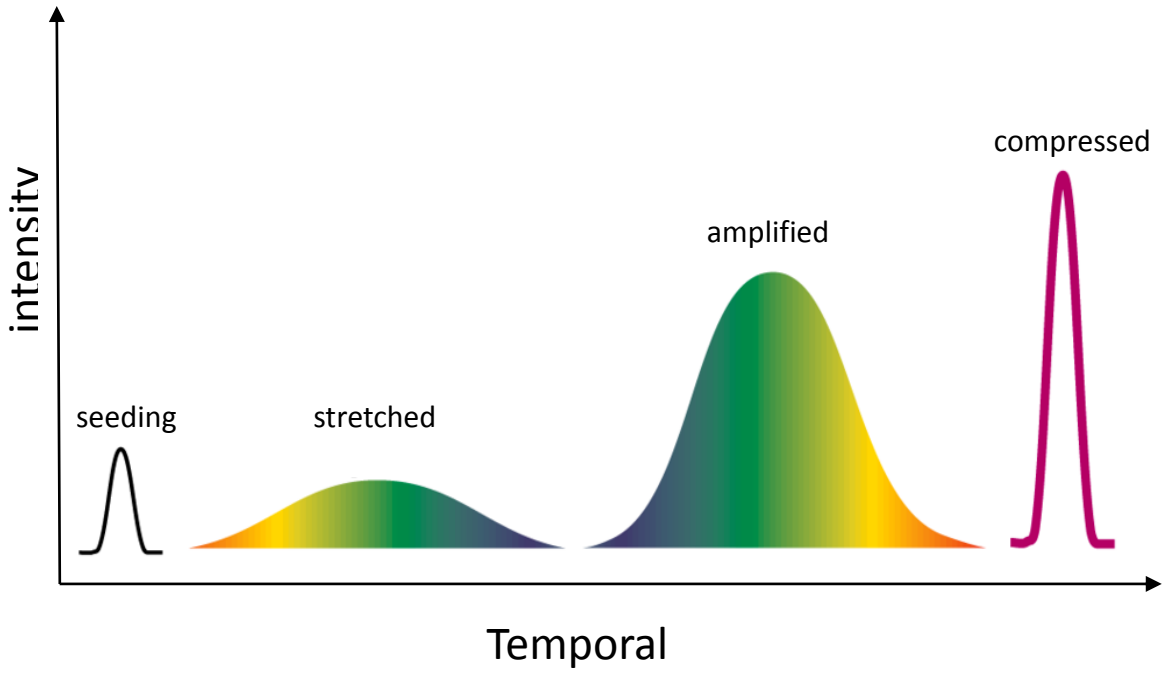

Figure 3.1 The temporal shape of a pulse through a CPA process.

3.2.1 *Stretcher and Compressor*

To stretch an ultrashort laser pulse duration to be ~100ps level, a pair of gratings is used to form a stretcher. A large dispersion should be introduced to stretch and compress the pulse duration over 10^4 times. In a stretcher, the dispersion is controlled by the relative distance between the image of the first grating and the second grating [57]. The high-wavelength components of the laser pulse travel a shorter path than the low-wavelength components. So, it disperses the spectrum and stretches the pulses, introducing positive dispersion [58]. The reverse action, delaying the longer wavelength more than the shorter wavelength, compresses the pulse and this is how the compressor works. The negative dispersion introduced by the compressor can compensate the dispersion induced by the stretcher and materials if it is designed with an appropriate incident angle and displacement for the gratings. The dispersion can be described as a function of wavelength [59]:

$$\emptyset(\lambda) = \frac{8\pi L}{\lambda}\sqrt{1 - (\frac{\lambda}{d} - \sin\theta_{in})^2} \tag{3-1}$$

where d is the spatial period of the grating groove, L is the grating separation and θ_{in} is the angle of incident. After the process of dispersing, amplifying, and compressing, it generates short, high power pulses.

3.2.2 *iFast 20 fs, 3mJ 1 kHz Laser System*

Our iFast kHz laser system with a single 14 passes amplifier can produce 20 fs, 3mJ pulses at a 1 kHz repetition rate as shown in Fig. 3.2 [60].

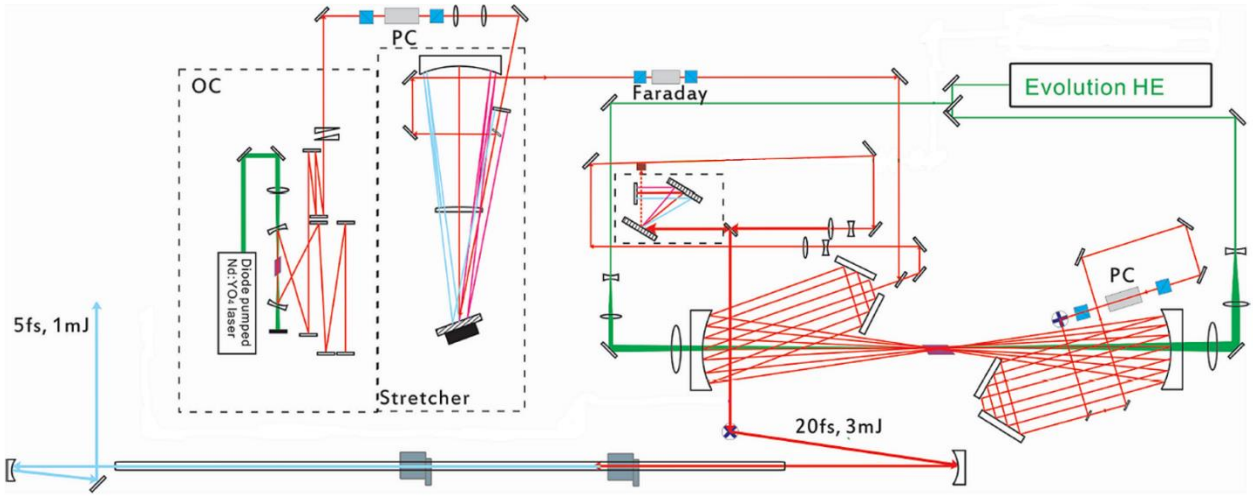

Figure 3.2 Schematic of iFast kHz laser system.

A commercial oscillator integrated with a Verdi-G pump laser (Vitara, Coherent) is capable of producing a 15 fs seeding pulse with a repetition rate of 80 MHz. The output pulse energy is ~ 5 nJ with a beam diameter of 2 mm. The kHz pulses are selected by the Pockels cell and sent to a grating-based stretcher [61]. After passing through the stretcher, the pulses are temporally stretched to ~100 ps. Then, the stretched pulses are amplified to 3 mJ through a 14-pass amplifier as shown in Fig. 3.2. The Ti:-Sapphire crystal is cooled to below 100 K by the cryogenic cooler to suppress not only thermal lensing but also higher-order aberrations and distortions. By geometrically arranging 14 passes of the seed beam through the Ti:-Sapphire gain medium, a total

gain over 10^6 was achieved. A pair of cavity mirrors with ROC = 2000 mm was used in the amplifier. After the first 7 passes, the beam is directed out of the cavity to reduce the amplified spontaneous emission (ASE) generated during the pre-amplification process by a Pockels cell. The beam direction is raised for the second 7 passes to be separated from the first 7 passes. Gain narrowing compensation filters were applied to reduce the gain narrowing effect [62]. After the amplification, the pulses are compressed by a grating compressor and the final output pulses are 20 fs with a 3 mJ pulse energy.

3.3 100 TW, 15 fs CPA System

A driving laser with a J-level pulse energy is developed to scale the isolated attosecond pulse energy to the μJ level. A GDOG method will be applied to generate the isolated attosecond pulses as discussed in chapter two. To reduce the leading and tailing edge ionization and increase the energy from the linearly polarized portion of the laser, the driving laser pulse duration needs to be less than 20 fs since only the center of the combined fields contributes to the generation of the isolated attosecond pulse [50]. To improve the conversion efficiency, it needs to keep the duration of the driving laser pulse as short as possible. Thus, we built a Ti:-Sapphire laser system optimized to produce high-energy (~2 J) and short- duration (~15 fs) pulses for high flux isolated attosecond pulse generation by GDOG.

3.3.1 *Seeding Pulses Generation*

To boost the driving pulse energy, we scale the seeding pulse energy to a mJ level compared with the nJ level for the kHz system. The pulse spectrum was broadened by the hollow-core fiber technique due to the self-phase modulation, resulting in a seeding pulse with a much larger spectral bandwidth [63]. A fiber with a 150 cm length and a 500 μm capillary radius is filled with argon gas as illustrated in Fig. 3.3. The laser beam is focused into the fiber by a 2000 mm focusing mirror through a 0.7 mm thick fused silica window. This window was placed in the middle of the focus and focal mirror to avoid self-phase modulation at the entrance. The fiber system is differentially pumped to achieve a throughput as high as 70%. The exiting beam is collimated by a silver-coated concave mirror with a 3 m radius of curvature. Figure 3.4 demonstrates the spectra before and after the hollow-core fiber. The spectrum is significantly broadened and supports a pulse shorter than 15 fs.

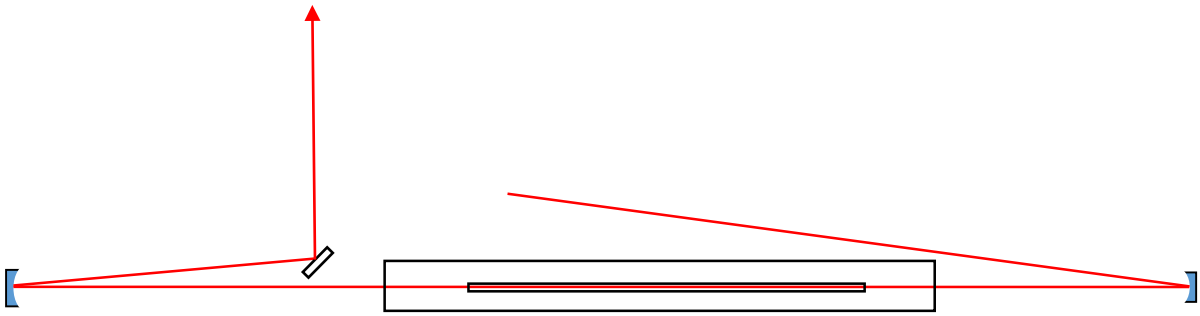

Figure 3.3 Schematic diagram of the hollow-core fiber setup.

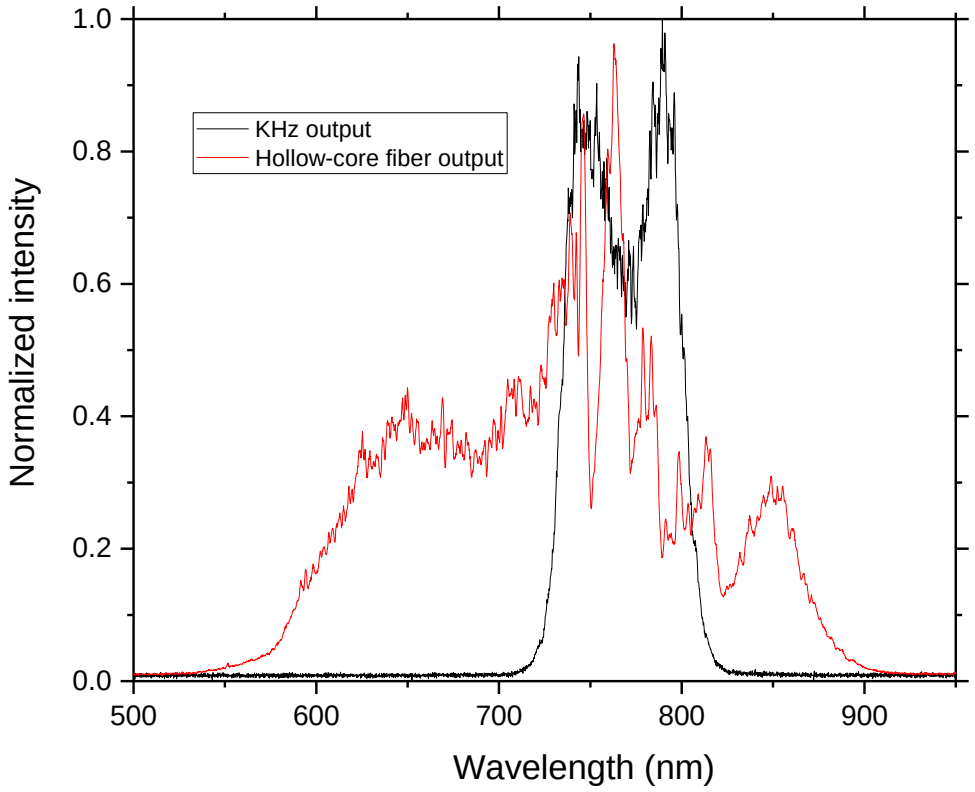

Figure 3.4 Laser spectra before (black) and after hollow-core fiber (red).

Hollow fibers are developed to generate single mode guiding elements and are suitable for high pulse energies. Pulse propagation inside a hollow fiber can be treated as occurring through multiple grazing incidence reflections at the dielectric inner surface of the fiber. Only the fundamental mode will propagate in a long fiber, considering the losses by the multiple reflections for higher order modes. For fused silica hollow fibers, the fundamental mode is the EH_{11} hybrid mode [63, 64]. The radial intensity is given by:

$$I(r) = I_0 J_0^2\left(\frac{2.405r}{a}\right) \tag{3-2}$$

where J_0 is the zero-order Bessel function, I_0 is the peak intensity, and a is the bore radius. The maximum broadening $\delta\omega_{max}$ is given by:

$$\delta\omega_{max} = 0.86\gamma P_0 \frac{1 - e^{-\alpha l}}{aT_0} \tag{3-3}$$

Here $\alpha/2$ is the field attenuation constant, P_0 is the pulse peak power, and T_0 is the half-width of the pulse. The factor γ is the nonlinear coefficient.

3.3.2 *Öffner Type Stretcher*

In a CPA system, the seed pulse is temporally stretched after it passes through a pair of gratings with the positive delay lines. It is a great challenge to stretch the pulses for a 15 fs, 100TW CPA amplification. The spectral width of the seed pulse from hollow-core fiber is relatively wide (~200 nm) and the pulse needs to be dispersed up to 300 ps, reducing the possibility of damaging laser optics. When a laser pulse duration approaches 15 fs, it becomes very difficult to eliminate the residual chirp over a broad spectrum. The Öffner type stretcher is an aberration free stretcher designed for the generation of very short duration pulses [65, 66]. It allows the stretching of a 15 fs pulse to 300 ps. It provides a large expansion ratio with minimized phase distortion. An Öffner type stretcher we use for our 10 Hz amplifier system has a single grating design including a concave and a convex mirror. Figure 3.6 shows the schematic diagram of the Öffner stretcher.

In our experiment, the aberration of this stretcher is small and the dispersion introduced by this stretcher can be mostly compensated by our compressor. The Öffner type stretcher consists of a 1000-mm radius of curvature concave mirror and a 500-mm radius of curvature convex mirror

with a single grating placed out of the center of curvature plane. Figure 3.5 gives the stretched pulse temporal profile.

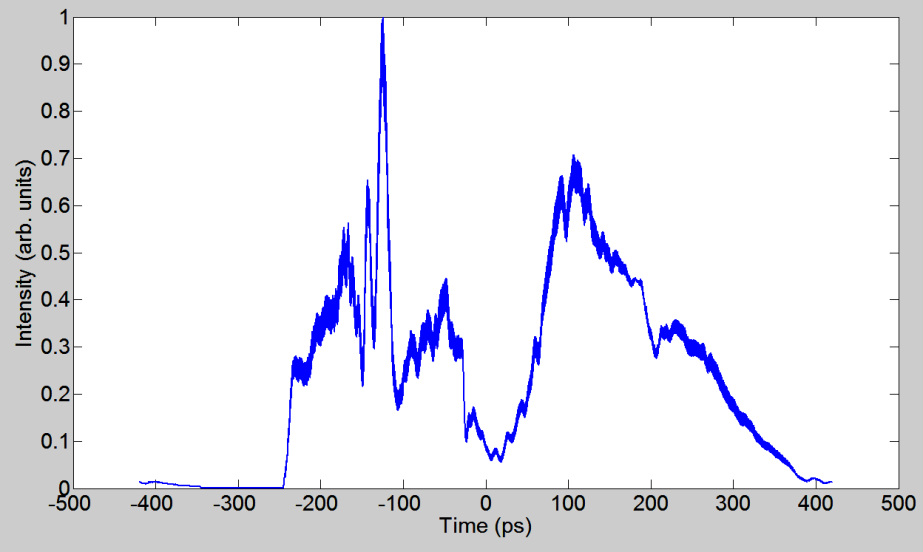

Figure 3.5 Stretched pulse temporal profile by our Öffner type stretcher.

During the amplification process, the pulse experiences the effect of phase distortion induced by different materials in the beam path. The second and third orders of the phase distortion caused by different materials can be mostly compensated by changing the distance between the two gratings and the incidence angle on the gratings. However, it is very difficult to compensate for fourth or higher orders of dispersion. In this case, the stretcher is optimized for a specific configuration. In the actual alignment, the distance between the concave mirror and the grating is 900 mm, and a convex mirror with a 505 mm curvature is used.

This grating size is a 110 mm ×110 mm with a groove density 1400 l/mm. The sizes for the concave and convex mirror are 600 mm × 100 mm 300 mm×10 mm, respectively with a gold coating. The overall throughput of the stretcher is above 30%.

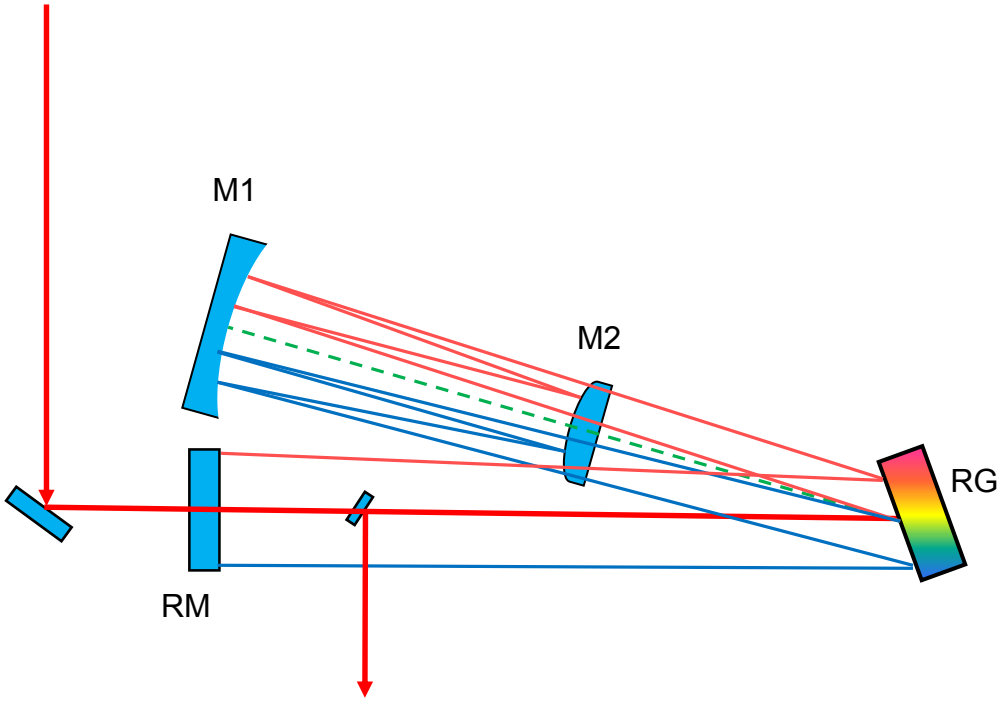

Figure 3.6 Experimental setup of the aberration-free Öffner stretcher: RG - reflective grating, RM - roof mirror, M1 - concave mirror with a radius of curvature of 1000 mm, M2 - convex mirror with a radius of curvature of 500 mm.

3.3.3 *Three-stage Multi-Pass Amplifier*

There are a total of three amplification stages to boost the pulse energy from mJ to J level. The overview setup of the laser is demonstrated in Fig. 3.7. The whole system consists of the seeding pulses generation from kHz system, hollow-core fiber, the Öffner type stretcher, the 1st

amplifier stages with 5 passes, the second stage amplifier with 3 passes [53], the third stage amplifier with 3 passes and the compressor.

The seed pulse generated from the hollow-core fiber has a wide spectrum covering from 550 nm to 950 nm [67]. Spectra from various stages of the laser are shown in Fig. 3.8 (a) and (b).

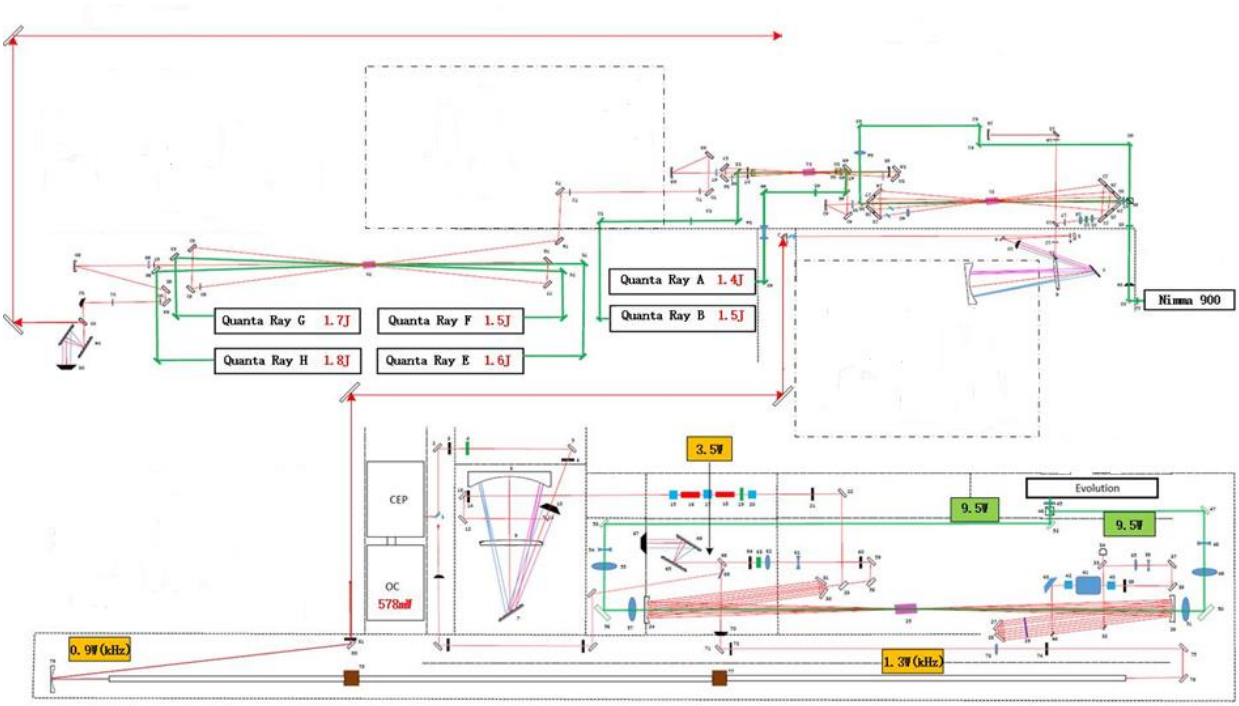

Figure 3.7 Schematic diagram of the 100 TW laser system.

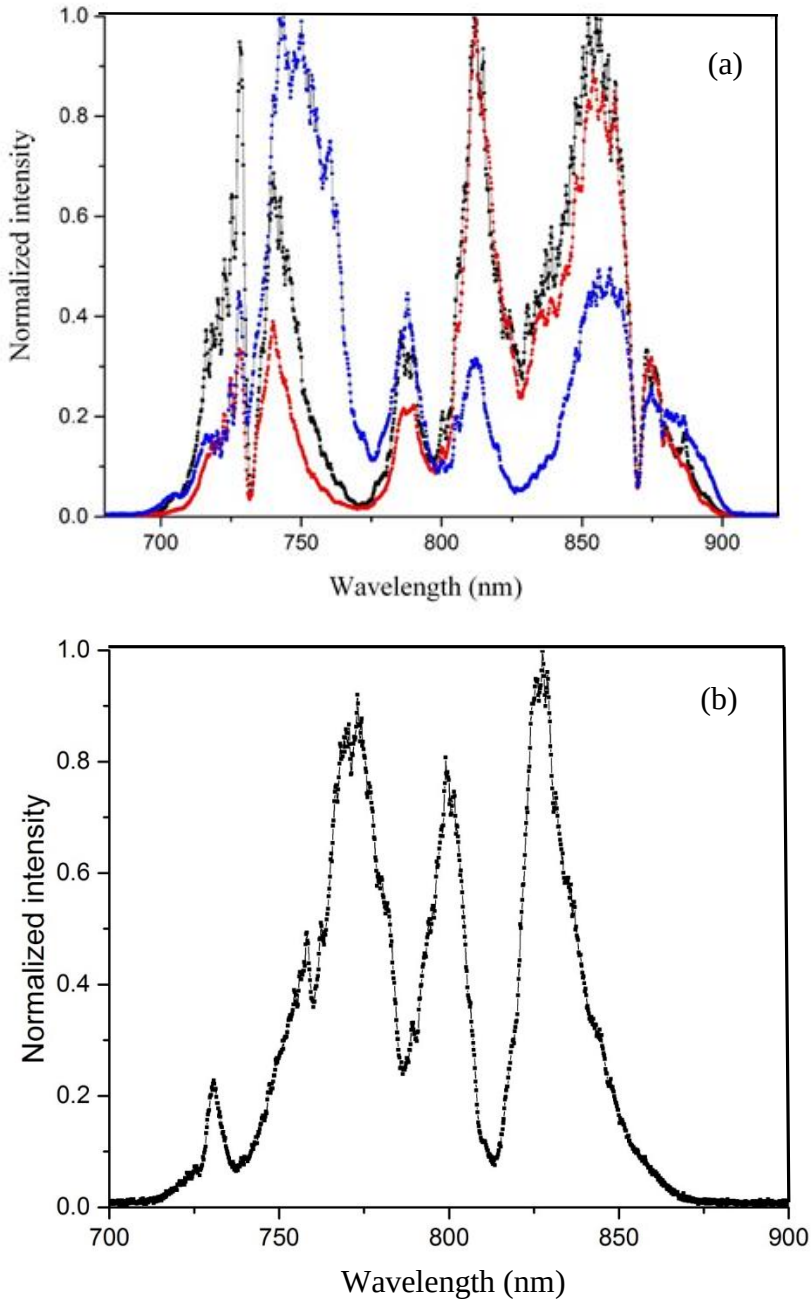

Figure 3.8 (a) spectra from stretcher (black line), 1st (blue line) and 2nd (red line) stage amplifier, (b) spectrum from 3rd stage amplifier.

After the stretcher, the 300 ps, 0.2 mJ positively-chirped pulses are sent to the first amplifier and the pulse energy is scaled to 50 mJ in a five-pass amplifier operating at 10 Hz pumped by a Nimma-900 laser with a pulse energy of 480 mJ from Beamtech Inc. The gain medium for the first stage is a Brewster-cut Ti:-Sapphire crystal cooled by the water from a chiller. A large-area, flat-cut Ti:-Sapphire crystal is used for the second stage. This crystal is pumped on both sides by two Q-switched frequency-doubled Nd: YAG lasers (Quanta Ray Pro 350) with a high M^2 factor. With a pumped area of 10 mm diameter, the first pass pump absorption is ~90%. The pump lasers are relay-imaged to the crystal to provide an excellent flat-top beam profile. Two diffractive optical elements (DOE) are also used for the beam homogenization [68]. The homogenization of the pump beam profiles guarantees the uniformity of the NIR pulse during the amplification process. The clear aperture of the DOEs is 25 mm and they are coated with anti-reflection (AR) coatings for 532 nm. The second gain medium is also cooled by water from a chiller to room temperature. Divergent lenses are used to compensate the thermal lensing. The energy of the amplified pulses can reach up to 600 mJ. The spectrum of these pulses covers from 700 nm to 900 nm as shown in Fig. 3.8 (a), which supports a 12.2 fs transform-limited pulse duration. A 3-D drawing for the stretcher and the 1^{st} and 2^{nd} amplifiers are shown in Fig. 3.9.

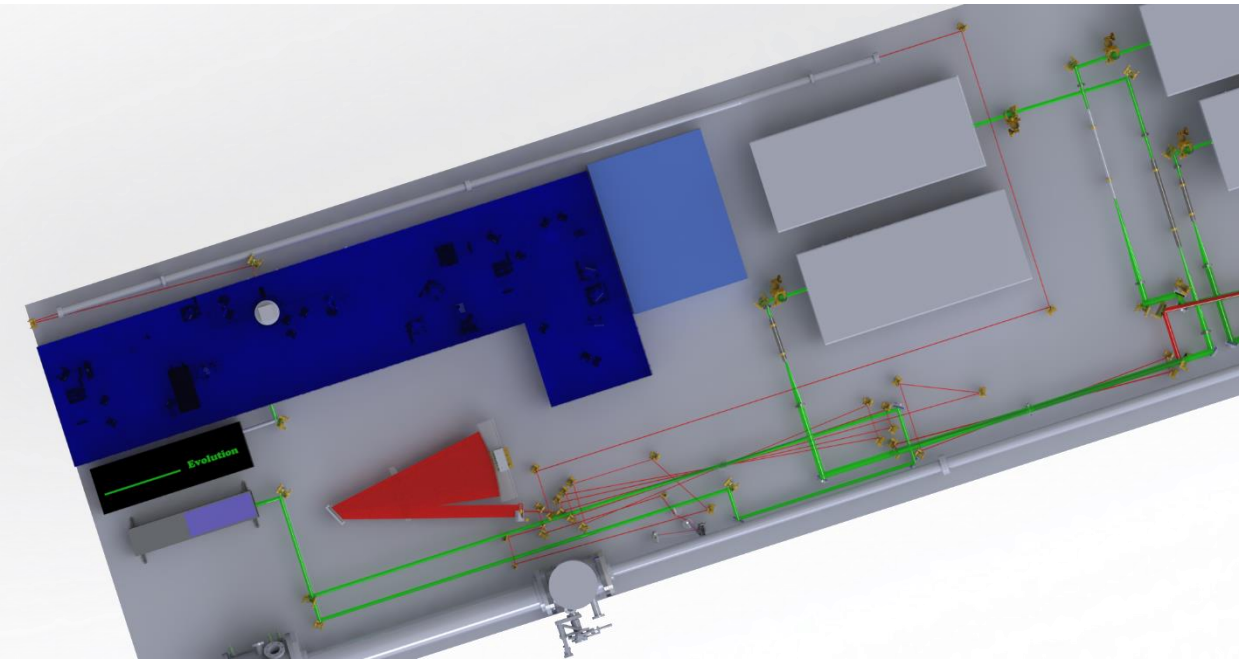

Figure 3.9 A 3-d drawing for the laser system for the first two stages.

After the pulse energy was boosted to 600 mJ, the beam size was expanded to 26 mm by a telescope. The beam was then sent to the 3rd amplification stage. The gain medium is a two inch,

flat-cut, cylindrical Ti:-Sapphire crystal. This crystal is pumped on both sides by four relay-imaged Quanta Ray Pro 350 pump lasers with two pump lasers for each side. After the 3 passes, the NIR laser is amplified to a pulse energy up to 3.3 J, with a total gain of ~5. The spectrum for the pulses is depicted in Fig. 3.8 (b). The transform limited pulse duration is about 13 fs. Figure 3.10 illustrates the configuration for the 3rd stage amplifier.

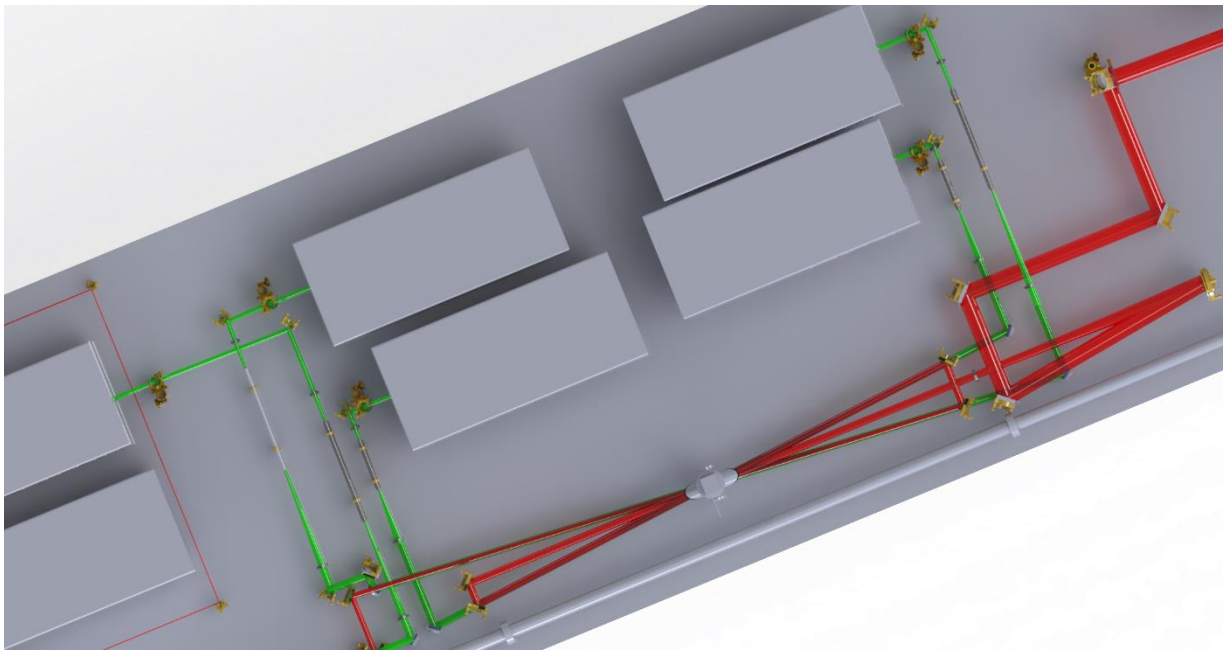

Figure 3.10 3-D drawing for the 3rd amplifier stage configuration of the 100 TW laser system.

It is worth noting that several gain narrowing compensation filters are used. Due to the gain narrowing effect during the amplification, a narrowed output spectrum will limit the compressed pulse duration and eventually reduce the peak intensity and the application of gating technique to generate isolated attosecond pulses [62]. In our laser system, we design and use dielectric multilayer (HfO_2/SiO_2) filters as the compensator to provide sufficient gain narrowing compensation. The calculated transmission curve is shown in Fig. 3.11.

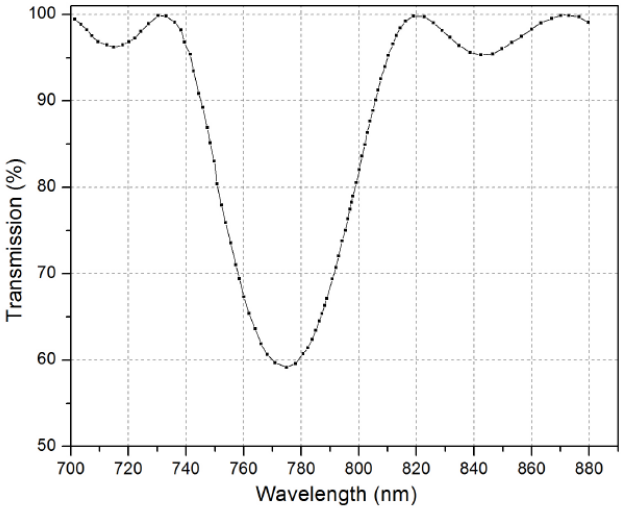

Figure 3.11 Designed and calculated transmission curve for a gain narrowing compensation filter.

Since the pulse energy is very high (J level) with the broadband spectrum, it is a critical part of the design to select a dielectric mirror for a high energy broadband pulse. By arranging broadband TiO2-SiO2 coatings underneath another layer of high-damage-threshold coatings (ZrO2-SiO2), a mirror with a high damaging threshold is designed to survive high laser intensity while providing broadband reflectivity [69]. This mirror can support sub 15 fs pulses for s-polarized laser with a 45-degree angle of incidence.

3.3.4 *10Hz Laser System Compressor*

To prevent the damaging on the optics and degradation due to non-linear effects during propagation, the beam is expanded to a diameter of 70 mm before the compressor chamber as shown in Fig. 3.12. The output energy of the pulse was 2 J for a 3.3 J input, which indicates that the peak power of the laser reached 100 TW. A pair of grating with a large size and a higher-

throughput is required. The compressor is placed in a vacuum chamber to avoid nonlinear effect from the interaction between the compressed 100 TW laser pulse and air as shown in Fig. 3.13.

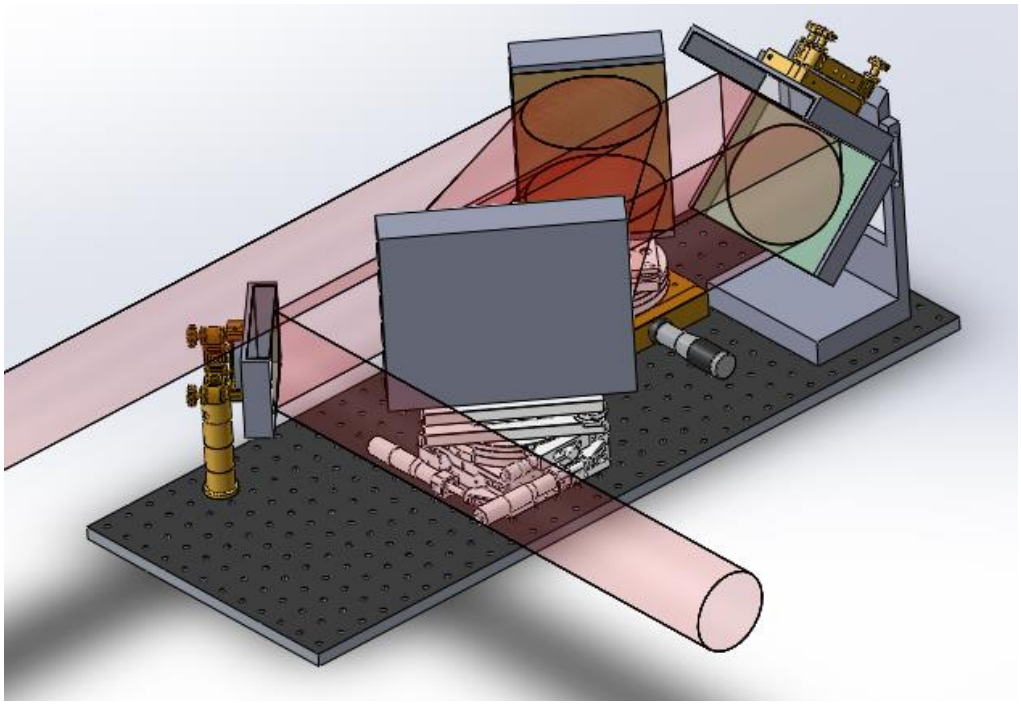

Figure 3.12 An optical layout for our 10Hz compressor.

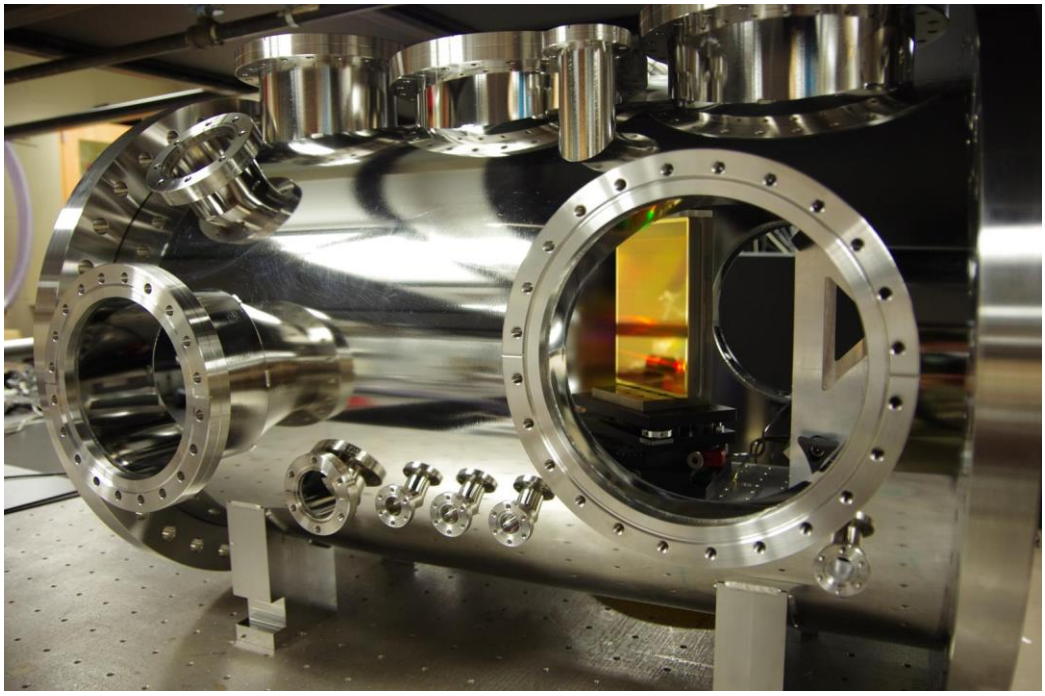

Figure 3.13 A picture of the compressor in a vacuum chamber.

The compressor uses a pair of 1480 l/mm gratings (220 mm × 165 mm and 175 mm ×135 mm, respectively) and has an overall throughput of 60%. The final output pulse energy is ~2 J after the compressor.

3.3.5 *Pulse Duration*

Under the phase-matching conditions, the HHG flux strongly depends on the beam quality of the driving laser. After the three-stage power amplifier, the laser spectrum extends from 700 nm to 900 nm. In order to compress the pulse duration as short as possible, the separation and incident angle of the two compressor gratings were fine-tuned manually to attain a spectral phase that

changed gradually. The high-order phase distortions will be further compensated by an acousto-optic programmable dispersive filter (AOPDF) as the stretcher [70]. The AOPDF has an adaptive phase control. The frequency-resolved optical gating (FROG) measurement indicated the pulse duration of 18.8 fs by optimizing the compressor grating separation and angle of incident as shown in Fig. 3.14 [71]. With the higher dispersion orders corrected by an AOPDF in near future, the pulse duration will be further compressed to below 15 fs. The measured and retrieved FROG traces of the pulse are represented in Fig. 3.15 (a) and (b) respectively. Figure 3.15 (c) is the retrieved temporal pulse shape (solid red line) and phase (dashed blue line). Figure 3.15 (d) depicts retrieved pulses spectrum (solid back line) and phase (dashed blue line) with the directly-measured spectrum (solid red line).

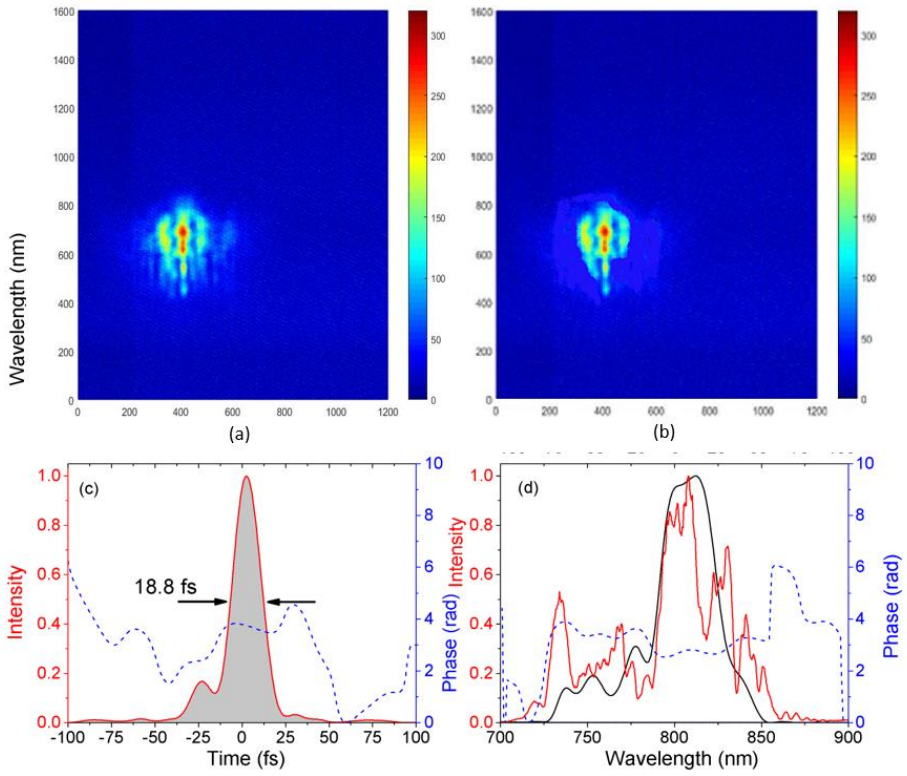

Figure 3.14 Characterization of the 18 fs laser pulse by SHG FROG.

CHAPTER 4 - GENERATION AND CHARACTERIZATION OF A HIGH-FLUX ATTOSECOND WITH A 100 TW LASER

So far, two types of attosecond pulse sources have been developed, one based on isolated attosecond pulses and the other on pulse trains [35, 41]. Isolated attosecond pulses are produced by different gating techniques as discussed in chapter two. So far, all attosecond experiments have been performed by combining one very weak (a few nanojoule) attosecond pulse with a stronger femtosecond visible or near infrared pulse [72, 73]. It is a grand challenge to generate isolated attosecond pulses with sufficiently high pulse energies (~1 microjoule) to perform true attosecond-attosecond pump-probe measurements, which is a goal of this thesis. The high attosecond flux will make it possible to use one pulse to initiate a process and a second attosecond pulse to probe the time dynamics of the electron-correlation, either in transient absorption or by photoelectron spectroscopy [32]. Two key reasons to pursue attosecond-attosecond measurements are to perform attosecond measurements on highly correlated materials for the first time and to build the capabilities to extend attosecond x-ray dynamics measurements to solid-state semiconductor, magnetic, and plasmonic systems [74].

In order to carry out the attosecond-attosecond pump-probe experiments, special facilities have been developed and implemented in our lab. They consist of three parts: 1) the 100 TW laser system as discussed in chapter three, 2) the HHG generation, 3) the HHG characterization and experimental station (end station) as shown in Fig. 4.1.

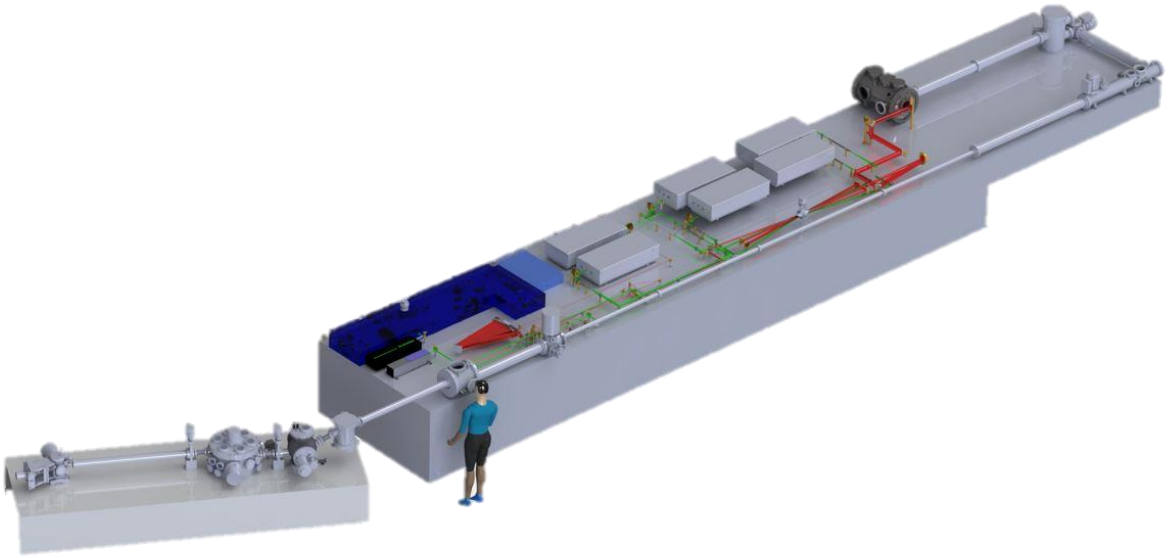

Figure 4.1 The schematic diagram of the attosecond-attosecond pump-probe facilities.

4.1 Wavefront Distortions Corrected by a Deformable Mirror

The laser beam focus profile is an important beam parameter for the generation of attosecond pulses after completion of the laser construction. The increase in harmonics energy is linearly dependent on the geometrical focusing area of the pump pulse. As a result, a loosely focused beam with an excellent beam quality is required under the phase-matching conditions [26, 75-77]. Unfortunately, in CPA laser system with a joule-level pulse energy, geometrical aberrations and surface quality from optical components, thermal effects and inhomogeneous doping in the Ti:-Sapphire crystal affect the beam profile and focusability, resulting in degrading of the energy distribution and wavefront [78]. It results in a different propagation pattern for a long focused geometry and thus to a poor focusability. A large portion of the pulse energy will be spread out into the wings of the focus, thereby severely reducing the attainable focused intensity.

As a result, the conversion efficiency is limited by the focus beam profile and restricts the scaling for the attosecond pulses flux. A deformable mirror (DM) with a feedback sensor was implemented to correct the wavefront distortions of lasers and keep the best focusability of the laser to the experimental chamber [79, 80]. In this case, all the energy from our laser system will be efficiently used for high flux HHG experiments.

The principle of adaptive optics is to correct an aberrant wavefront using a system consisting of: 1) a wavefront sensor to measure the wavefront deformation, 2) a wavefront corrector to perform the correction using actuators that deform its reflective surface, 3) a software package that controls the mirror according to the data from the sensor. In our setup, the system consists of three parts: 1) a ILAO Star deformable mirror, 2) a HASO3 FIRST wavefront sensor, and 3) wave-tuning software. The experimental configuraton for a DM is illustrated in Fig. 4.2. The picture of the real DM is shown in Fig. 4.3.

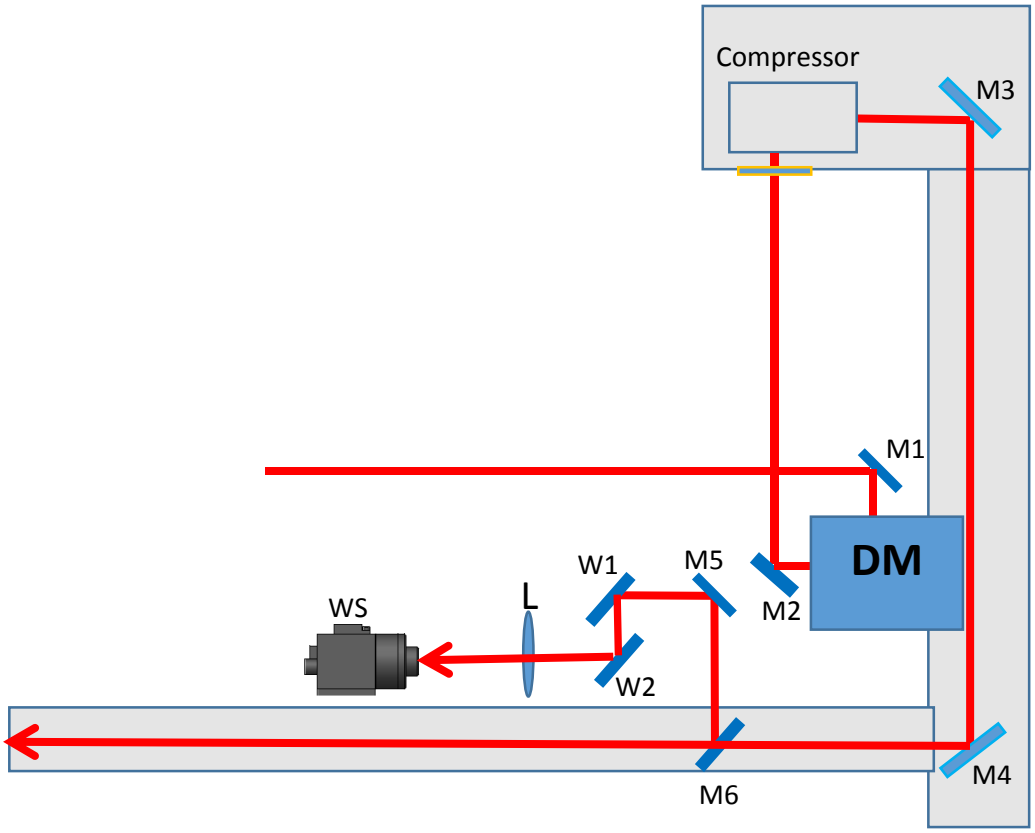

Figure 4.2 The DM setup in experiment: M1~M5 - dielectric mirror, DM - deformable mirror, w1 and w2 - wedge, M6- dielectric mirror on a manipulator, L - a f=500 mm concave lens, WS - wavefront sensor (HASO3 FIRST).

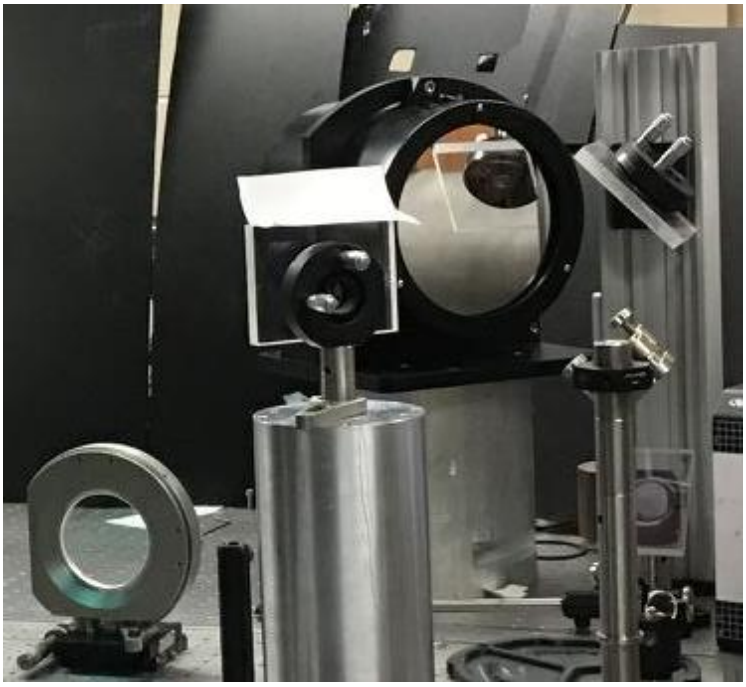

Figure 4.3 The picture of the 6 inch DM on the optical table.

A deformable mirror (ILAO Star, Image Optic Inc) is based on the use of mechanical actuators which apply a force at the back of the substrate. Macroscopic displacement of mechanical parts of the actuators will modify the force applied to the back of the mirror, which introduces a nanometer scale change to the reflective surface as shown in Fig. 4.4 [81].

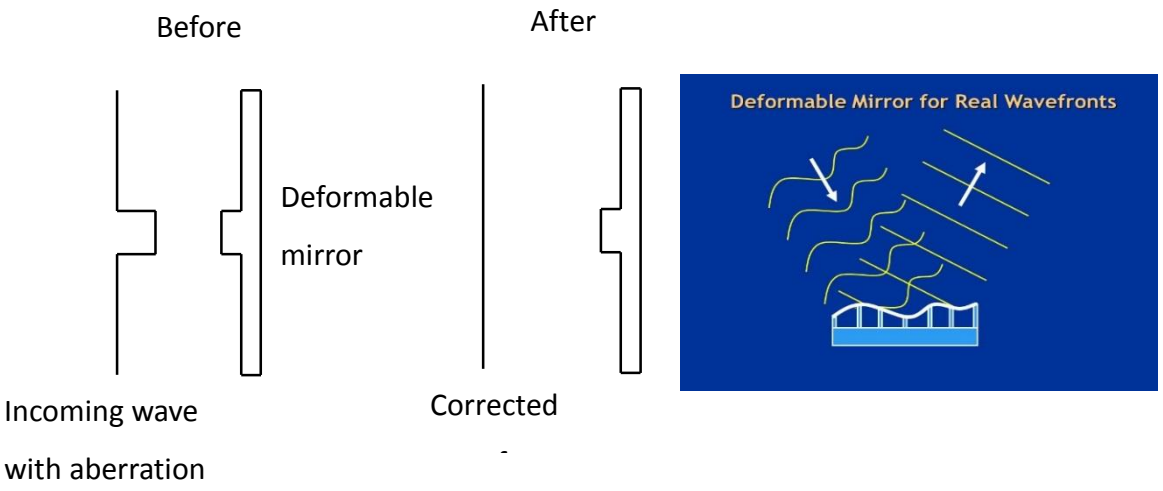

Figure 4.4 The correction of the wavefront by a DM.

When voltages are applied to the actuators, the mirror can be locally deformed. The overall deformation caused by the whole set of actuators defines a new mirror shape. The macroscopic displacement inside the actuator requires much more time than a simple voltage or current change. With mechanical actuator technology, it is not necessary to hold voltages to actuators to maintain the force to the mirror surface. Mirror shape is not modified if power is turned off or if the controller is unplugged. Once the desired shape is reached, the deformable mirror plays as a passive component, and the surface shape is stable like a passive component as shown in Fig. 4.5.

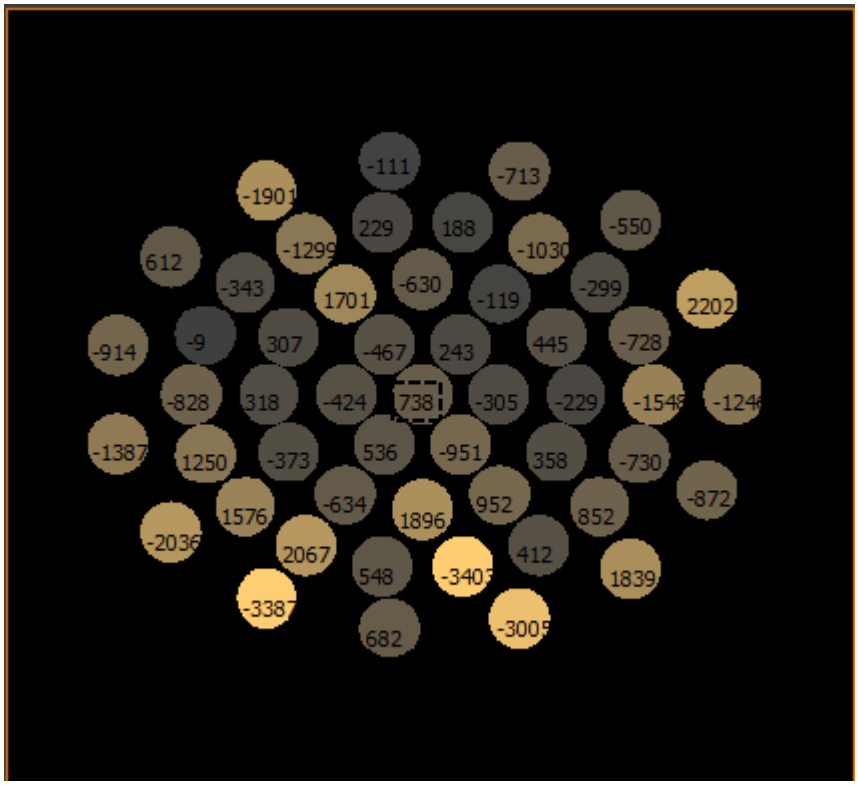

Figure 4.5 The DM actuators with voltages applied.

With these characteristics, DM is in a sense more like a programmable phase modulation component than an adaptive optics system. We use the DM in a finite closed loop configuration (3-10 iterations) to set its shape, and once the desired shape is obtained, we stop the closed loop. The DM will perfectly maintain its shape, and the laser beam wavefront will be corrected without the hassle and requirement of having a closed loop system running continuously while using our laser. The mirror's reflective area is larger than the beam size to avoid clipping of the far edge of the beam which would create diffraction hotspots in the beam. The laser beam is always carefully centered on the deformable mirror to get the best correction quality and optimal performance of the DM.

To collect information about the wave front and the intensity profile to the DM feedback control, a Shack-Hartmann wavefront sensor is used [82]. First, the pulse is broken down into "multiple elementary beams" by a matrix of microlenses. Each lens takes a small part of the aperture. The secondary beams then are focused on the detectors of a CCD camera.

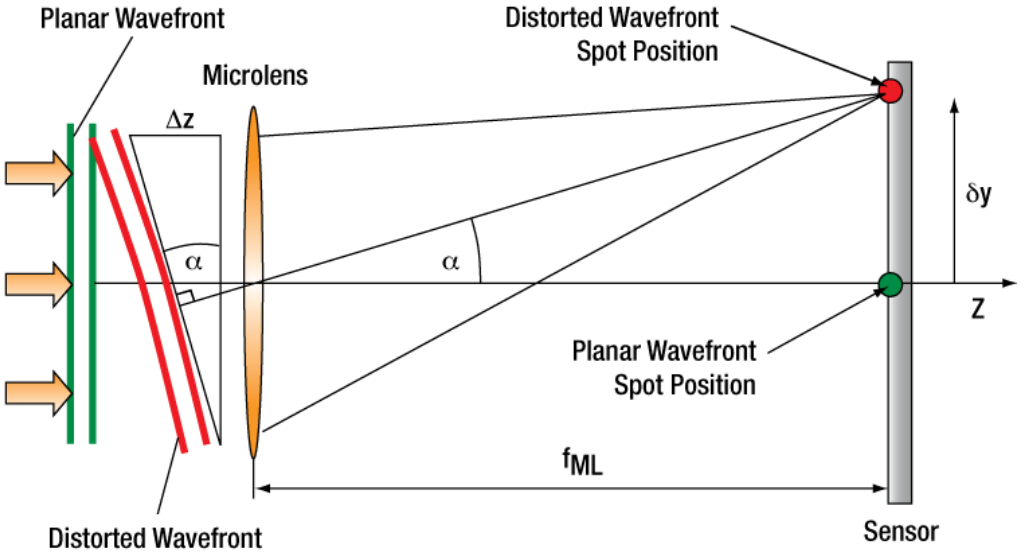

Figure 4.6 A Shack–Hartmann sensor. An incident pulse is focused on a CCD camera and we can obtain the angle of incidence of the wavefront (adapted from “"Shack-Hartmann Wavefront Sensors Tutorial", Thorlabs.com).

When an incoming wavefront is plane, all images are projected in a regular grid. If a wavefront is distorted, the images deviate from their nominal positions as shown in Fig. 4.6. The displacements of image in y direction is given by:

$$\delta y = \alpha f_{ML} = \frac{\Phi(x,y)}{dy} f_{ML} \tag{4-1}$$

where α is the wavefront slope in the y direction, Φ (x, y) is the wavefront. The same equation can be used to determine the slope along the x-axis:

$$\delta x = \beta f_{ML} = \frac{\Phi(x,y)}{dx} f_{ML} \tag{4-2}$$

where β is the wavefront slope in the x direction.

The first derivative of the wavefront is what is measured. Indeed, as shown in Fig. 4.6, the presence of aberrations in the beam being measured causes the focal spots to move to the focus of each microlens. The movement of each of these focal spots is directly proportional to the local derivative of the wavefront of the incident beam. The proportionality factor is the focal length of the microlenses. The intensity of the beam is directly proportional to the amplitude of each focal spot on the CCD camera's sensor. A good feature of the Shack–Hartmann wavefront sensor (SHWFS) is that it is completely achromatic, so the slopes are independent on the wavelength.

The first step to measure a wavefront with the SHWFS is to determine the location of these diffracted spots on the camera. The sensor has been calibrated by recording an image of a standard uniform plane wave. These diffracted spot locations can be determined by calculating the centroids along the x- and y-axis [83]. The centroid in the x direction is given by:

$$\bar{x} = \frac{\int_{-\infty}^{+\infty}\int_{-\infty}^{+\infty} I(x,y)\cdot x\cdot dx\cdot dy}{\int_{-\infty}^{+\infty}\int_{-\infty}^{+\infty} I(x,y)\cdot dx\cdot dy} \tag{4-3}$$

where I (x, y) is the intensity as a function of x and y.

The Hartmann wavefront sensor consists of a set of discrete pixels on a CCD that can be described by the variable i along x-axis and j along y-axis as shown in Fig. 4.7.

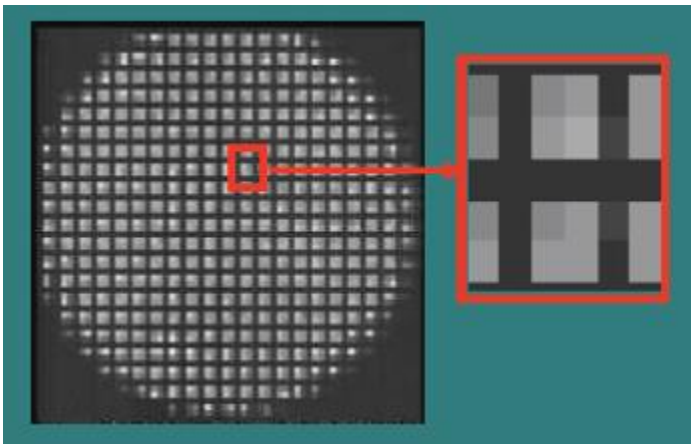

Figure 4.7 An image taken by SHWFS and the inset shows the CCD camera pixels. (adapted from LECTURES Ay122a-Adaptive Optics I).

So, we can replace the integral with a summation and the general centroid can be written as:

$$\bar{x} = \frac{\sum_{i=i_{min}}^{i_{max}} \sum_{j=j_{min}}^{j_{max}} I(i,j) \cdot i}{\sum_{i=i_{min}}^{i_{max}} \sum_{j=j_{min}}^{j_{max}} I(i,j)} \cdot s \tag{4-4}$$

where s represents the spacing for pixels.

Thus, we will have the wavefront equations:

$$\frac{\sum_{i=i_{min}}^{i_{max}} \sum_{j=j_{min}}^{j_{max}} I(i,j) \cdot i}{\sum_{i=i_{min}}^{i_{max}} \sum_{j=j_{min}}^{j_{max}} I(i,j)} \cdot s = \frac{\Phi(x,y)}{dx} f_{ML} \tag{4-5}$$

By integrating the wavefront differential equations for both x and y direction, the wavefront then can be reconstructed by performing an integration on the gradient measurements. Two types of wavefront reconstruction algorithms (zonal and modal) can be implemented to reconstruct the wavefront [84]. The terms of various aberrations are applied to the reconstruction of the wavefront

Zernike polynomials as demonstrated in Table 4.1 since WF distortion is a collection of various aberrations [85].

Table 4.1 ZERNIKE aberration terms used for reconstruction of the wavefront.

#	Form of the Polynomial	Name
1	$\rho\cos(\theta)$	Tilt x, (about y axis)
2	$\rho\sin(\theta)$	Tilt y, (about x axis)
3	$\rho^2\cos(2\theta)$	Astigmatism x, (0°)
4	$2\rho^2-1$	Power or Focus
5	$\rho^2\sin(2\theta)$	Astigmatism y, (45°)
6	$\rho^3\cos(3\theta)$	Trefoil x
7	$(3\rho^3-2\rho)\cos(\theta)$	Coma x
8	$(3\rho^3-2\rho)\sin(\theta)$	Coma y
9	$\rho^3\sin(3\theta)$	Trefoil y
10	$\rho^4\cos(4\theta)$	Tetrafoil x
11	$(4\rho^4-3\rho^2)\cos(2\theta)$	Secondary Astigmatism x
12	$6\rho^4-6\rho^2+1$	Primary Spherical
13	$(4\rho^4-3\rho^2)\sin(2\theta)$	Secondary Astigmatism y
14	$\rho^4\sin(4\theta)$	Tetrafoil y
15	$\rho^5\cos(5\theta)$	Pentafoil x
16	$(5\rho^5-4\rho^3)\cos(3\theta)$	Secondary Trefoil x
17	$10\rho^5-12\rho^3+3\rho)\cos(\theta)$	Secondary Coma x
18	$10\rho^5-12\rho^3+3\rho)\sin(\theta)$	Secondary Coma y
19	$(5\rho^5-4\rho^3)\sin(3\theta)$	Secondary Trefoil y
20	$\rho^5\sin(5\theta)$	Pentafoil y
21	$(6\rho^6-5\rho^4)\cos(4\theta)$	Secondary Tetrafoil x
22	$(15\rho^6-20\rho^4+6\rho^2)\cos(2\theta)$	Tertiary Astigmatism x
23	$20\rho^6-30\rho^4+12\rho^2-1$	Secondary Spherical
24	$15\rho^6-20\rho^4+6\rho^2)\sin(2\theta)$	Tertiary Astigmatism y
25	$(6\rho^6-5\rho^4)\sin(4\theta)$	Secondary Tetrafoil y
26	$(21\rho^7-30\rho^5+10\rho^3)\cos(3\theta)$	Tertiary Trefoil x
27	$(35\rho^7-60\rho^5+30\rho^3-4\rho)\cos(\theta)$	Tertiary Coma x
28	$(35\rho^7-60\rho^5+30\rho^3-4\rho)\sin(\theta)$	Tertiary Coma y
29	$(21\rho^7-30\rho^5+10\rho^3)\sin(3\theta)$	Tertiary Trefoil y

In real experiments, the most important specific principle is the pupil conjugation for an adaptive optics system. The purpose is to create an image of the DM on the matrix of micro-lenses of the wavefront sensor using a dedicated optical system. This optical system is also used to adapt the size of the DM to the size of the measurement pupil of the wavefront sensor. The effect of conjugation is to ensure a fixed pupil on the wavefront sensor when the various actuators are in motion. When the DM applies a correction, the result of pupil conjugation is to provide a fixed pupil on the wavefront sensor and to maintain a constant spatial distribution of the intensity. Each action applied to the DM is therefore visible only on the measured wavefront. When pupil conjugation is absent or poorly executed, more iterations are required to achieve the best possible correction, and the final quality of the correction is diminished.

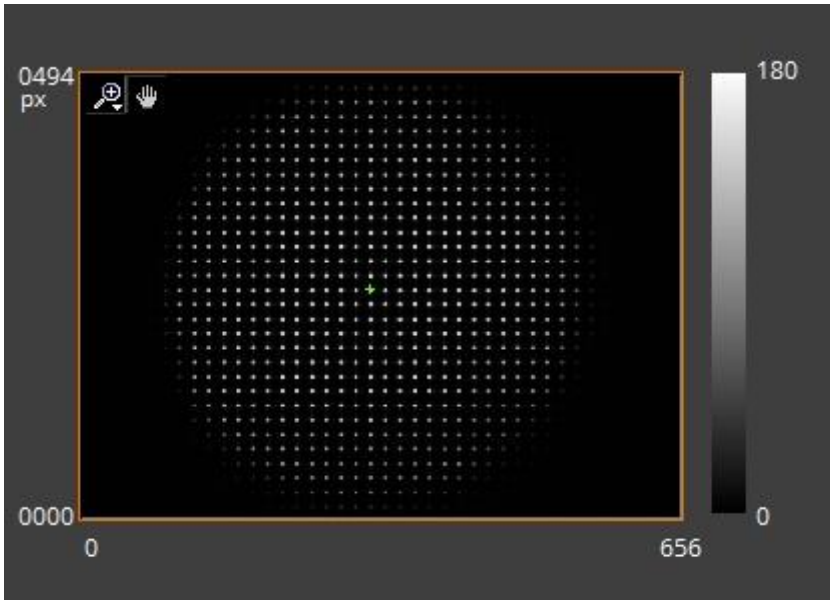

Figure 4.8 An image for intensity distribution from a SHWFS.

Figure 4.8 describes the image directly from a DM sensor with an excellent pupil conjugation. It has a constant spatial distribution of the intensity. Table 4.2 shows the specifications for our wavefront sensor (HASO3 FIRST, Imagine Optic, Inc).

Table 4.2 Wavefront sensor specifications.

Description	Specification
Aperture dimension	4.8 x 3.6 mm²
Number of microlenses	40x 32
Tilt dynamic range	>±3° (400 λ)
Focus dynamic range - minimum local radius of curvature	15 mm
Focus dynamic range - maximum NA	> 0.1
Repeatability (rms)	< λ/200
Wavefront measurement accuracy in relative mode (rms)	~λ/100
Wavefront measurement accuracy in absolute mode (rms)	~λ/100
Tilt measurement sensitivity (rms)	5 µrad
Focus measurement sensitivity (rms)	3·10^-3 m-1
Spatial resolution	~110 µm
Working wavelength range	350 - 1100 nm
External trigger	yes

To characterize and quantify the quality of the beam, the Strehl ratio criterion is chosen [86]. This Strehl ratio is the ratio between the peak intensity at focus with a distorted wavefront and a near-field intensity profile to that of the same intensity distribution but with a flat wavefront.

$$\text{Strehl ratio} = \frac{\text{Peak intensity at focus of a real beam}}{\text{Peak intensity at focus of a reference beam}} \tag{4-6}$$

Using the results from our wavefront sensor, we can calculate this Strehl ratio and quantify accurately the peak intensity at focus.

The experimental results with different phase compensations given by the ILAO DM for our 10 Hz laser are demonstrated in Fig. 4.9. The wavefront in Fig. 4.9 (b) has a wavefront with a peak to valley (PV) value of 725 nm, while the result in Fig. 4.9 (a) shows a PV value of 190 nm. The distortion of the wavefront root mean square (RMS) are 31 nm and 94 nm, respectively.

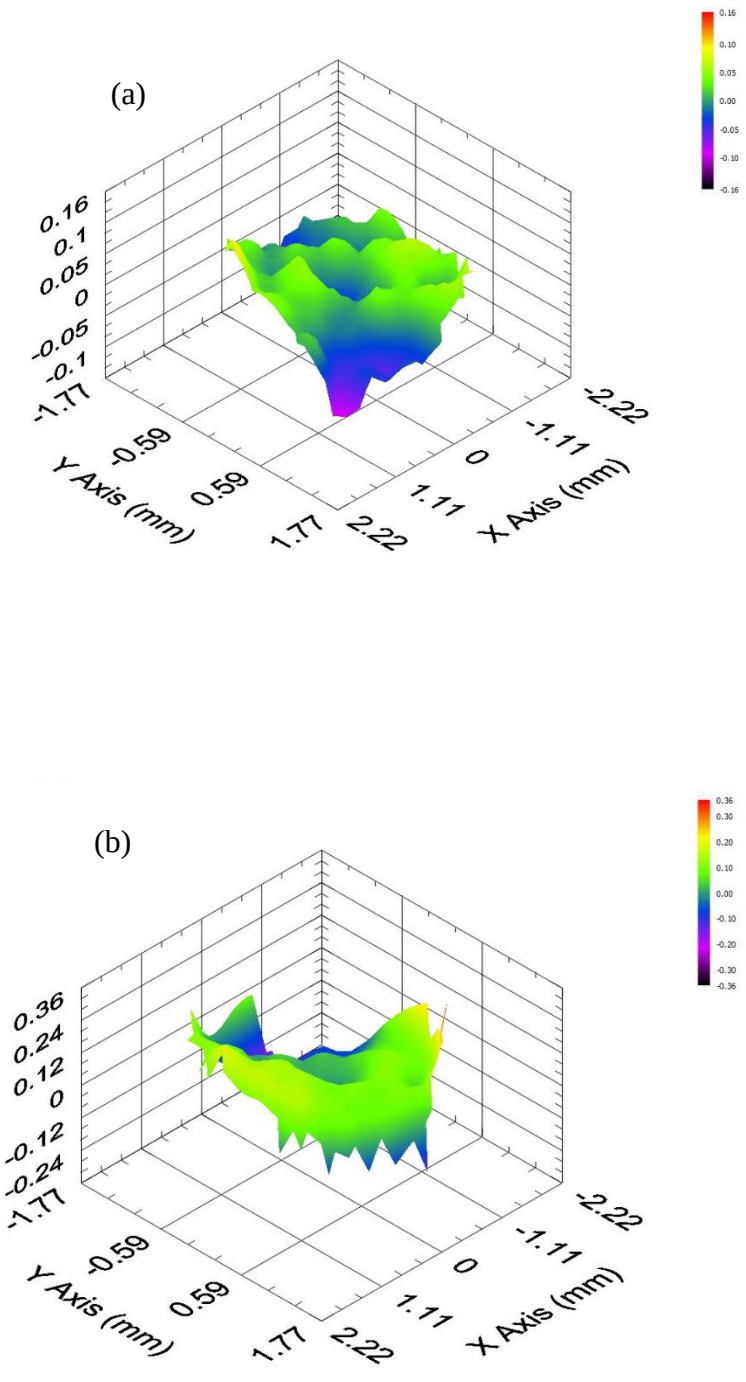

Figure 4.9 Experimental results for correction of a wavefront: (a) 31 nm RMS, (b) 94 nm RMS.

Figure 4.10 shows the intensity profile of the corrected beam from the DM sensor with a phase distortion of 94 nm RMS. It is worth noting that the profile begins to show a flat-top shape.

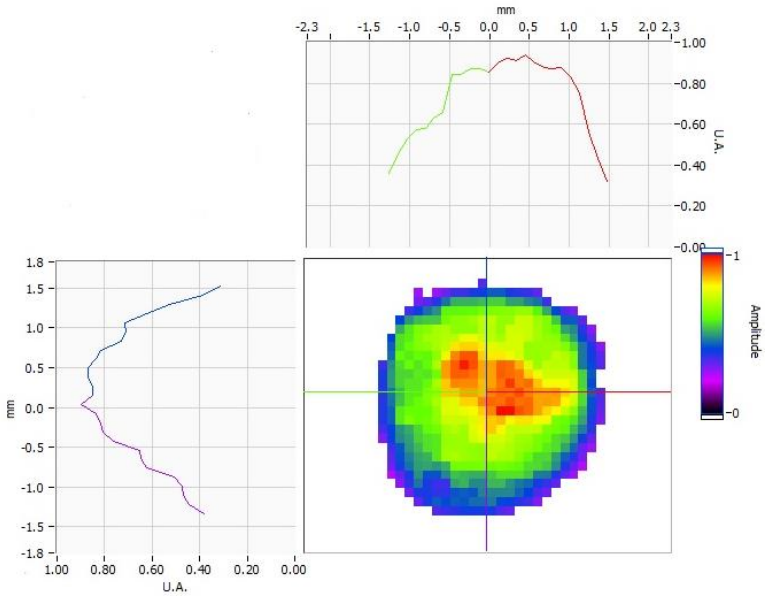

Figure 4.10 Intensity profile measured by the DM sensor.

Figure 4.11 illustrates the measured wavefront with different distortion RMS values and calculated spot size for phase A without corrections, and phase B with corrections. The distortion RMS values are 208 nm and 21 nm for phase A and phase B, respectively. Figure 4.11 (b) shows two spots calculated with different wavefront distortions. It clearly shows a significant improvement of the beam profile by reducing the distortion, which could allow the focal peak intensity of our laser to be significantly increased. The correction of distortions by the DM permits both spatial cleaning of the laser beams and an increase in the peak intensity for our gas target. We improved the wavefront by decreasing the distortion from 208 nm to 21 nm (RMS). The Strehl ratio was increased from 10% to 92%, or by a factor of 9.

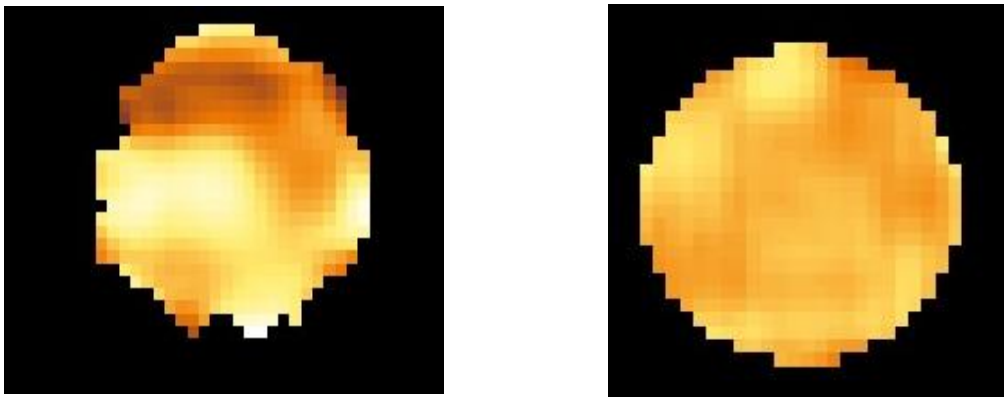

Phase A Phase B

(a)

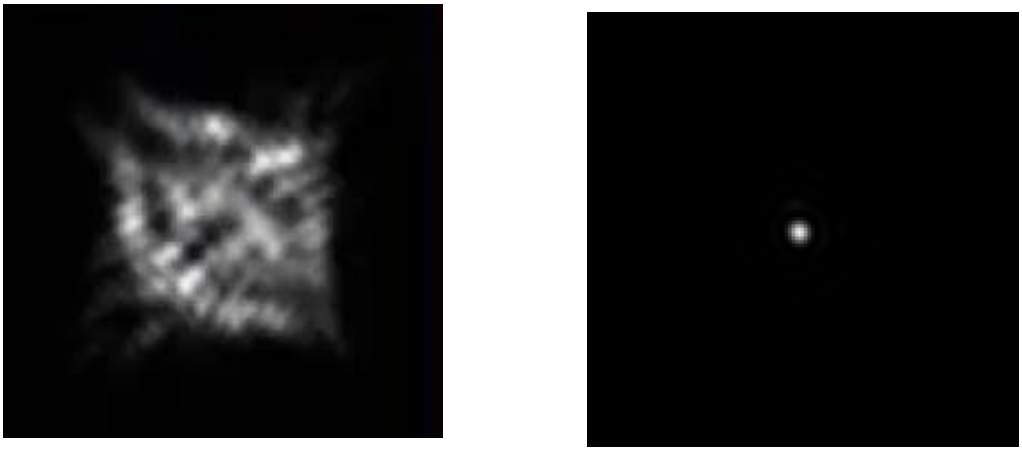

Spot A Spot B

(b)

Figure 4.11 (a) Experimental results for a distorted wavefront (Phase A) and a corrected wave front (Phase B), (b) Calculated spot sizes A, without corrections and B, with corrections.

We also check the wavefront distortion RMS by DM for different pulse energies since the distortions may change due to the thermal effect and energy distribution. The result shows a distortion RMS stability from 50 nm to 63 nm.

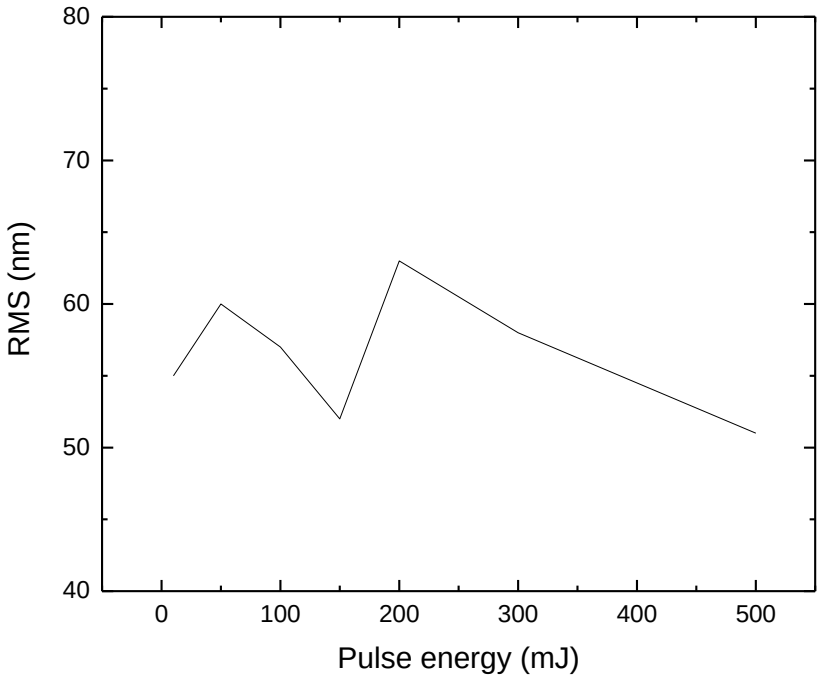

Figure 4.12 Correction RMS stability for different pulse energies.

As a comparison, the focus of our laser in the experiment chamber is shown in Fig. 4.13 measured directly by a CCD camera, without installation of the adaptive optics system. The focus beam profile shows a spatial distortion due to the distortion of the wavefront [79, 87]. It indicates the degradation of the laser beam profile. The experimental beam size is about 5 times the diffraction-limited spot size. Here, the diffraction limit is the Fourier transform distribution with a flat phase, leading to a 25 times decrease of the peak intensity in the gas target. Thus, the conversion efficiency of the HHG will be very low.

With a distortion of RMS 21 nm ($\lambda/40$), an excellent focus beam profile was attained as shown in Fig. 4.13. The FWHM beam diameter is ~500 μm, which is close to the diffraction transform limited beam size.

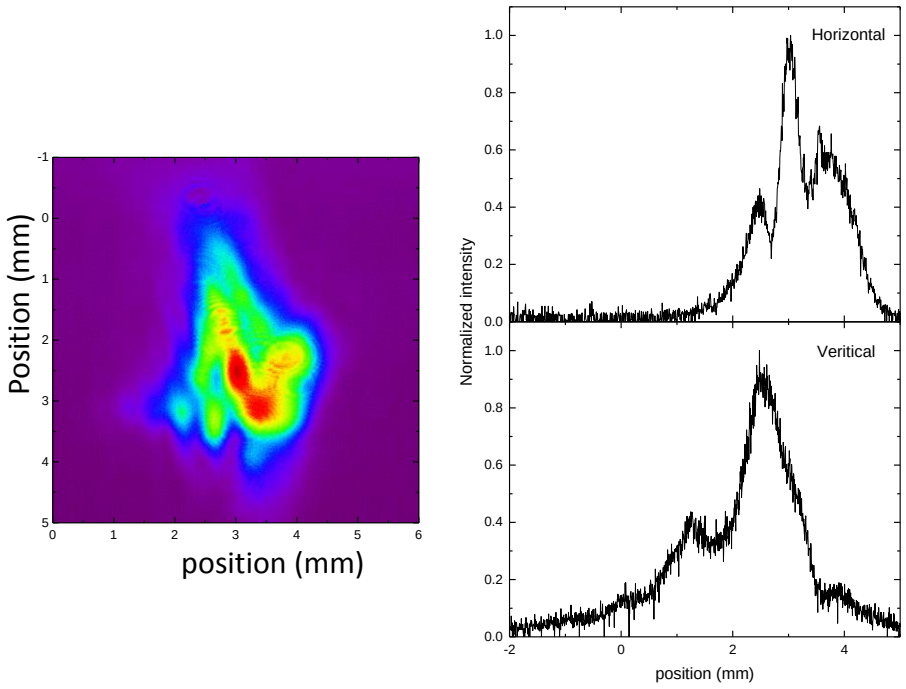

Figure 4.13 A measured focus beam profile without DM.

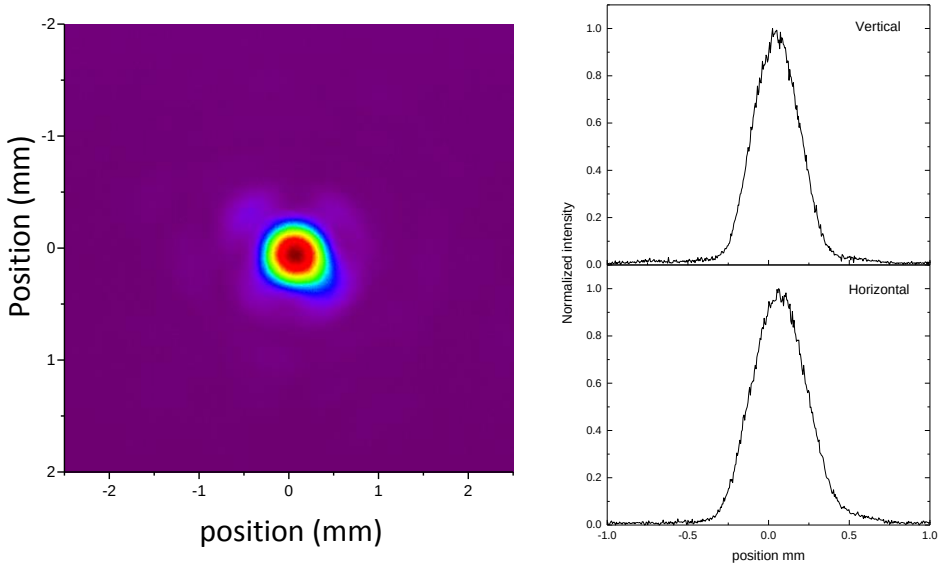

Figure 4.14 A measured focus beam profile with a distortion of 21 nm RMS by our DM.

4.2 Phase Matching for Enhancing Attosecond Pulse Flux

The photon flux for isolated attosecond pulses needs to be as high as possible to make it applied to non-linear multi-photon processes in both atoms and molecules. Phase-matched HHG by a loose-focusing geometry generates highly focusable intensity with a fully spatiotemporal coherence [88, 89]. It is thus sufficient to induce nonlinear phenomena in the XUV region if the conversion efficiency of HHG can be significantly improved by the phase-matching between the HHG field and the atomic dipole [31]. High conversion efficiency for HHG requires optimization of microscopic and macroscopic properties of the radiation process. A microscopic response is well explained by the three-step model as described in chapter one. In every half cycle of the driving laser field, an electron can tunnel through the distorted atomic potential barrier. Electrons will be accelerated in the intense laser field. Depending on the release time, the electrons have a possibility to return to the parent ion, recombine and emit XUV photons. The trajectories of ejected electrons can be treated as so called short and long ones, depending on the excursion time in the continuum. The generation of harmonics requires laser intensities from 10^{14} W/cm^2 to 10^{15} W/cm^2 depending on different medium gases.

On the other hand, the macroscopic response can be described as this: the total HHG intensity is a coherent sum of the photons emitted from different atoms or molecules in the target medium. The HHG flux can only be scaled up when the XUV fields emitted by atoms at different positions in the propagation direction of the driving laser are in phase so that they can be added up constructively and maximized by the time they reach the detector. Perfect phase matching happens when the speed of a polarized field (including the dipole phase) equals to that of a HHG field [90]. Unfortunately, normal dispersion is frequency dependent and makes the harmonics travel at a

different phase velocity as compared to the driving laser through the gas medium. This leads the phase to be mismatched and the output HHG flux would be expected to reduce dramatically while increasing gas medium length.

So here, $\Delta k = qk_1 - k_q$ is the wave-vector mismatch along the propagation direction between the wave-vector of the driving laser and the harmonics. In order to maximize the HHG flux, the wave-vector mismatch must be minimized. The coherence length is defined as $L_{coh} = \pi/\Delta k$. The main terms associated with the phase matching in a non-guiding focus geometry include: the neutral medium dispersion, atomic dipole phase, geometrical dispersion, plasma density, and any nonlinear effects. Each of these terms has a different sign and it means one effect can be cancelled by changing the effect of another to minimize the phase mismatch or attain the phase-matching condition. The total wave-vector mismatch is given as:

$$\Delta k = \Delta k_{neu} + \Delta k_{geom} + \Delta k_{plasma} + \Delta k_{dipole} + \Delta k_{other} \tag{4-7}$$

The main dispersion term due to the neutral atomic target is expressed as:

$$\Delta k_{neu} = k_{qneu} - qk_{1neu} \tag{4-8}$$

where k_{qneu} is the wave-vector of the harmonic, k_{1neu} is the wave-vector of the driving laser, and q is the harmonic order [91]. It mainly depends on the type of gas and the pressure. It can be approximately written as:

$$\Delta k_{neu} = qN\frac{2\pi\omega}{c}P(n_\omega - n_{q\omega})(1-\eta) \tag{4-9}$$

where N is the number of atoms per unit volume, ω is the fundamental frequency, P is the pressure of the gas target, n_ω and $n_{q\omega}$ are refractive index of the fundamental and harmonic in the gas target, respectively and η is the ionization probability by the ADK calculation. One of the important

features of this formula is that it is pressure dependent. This term has the positive sign since refractive index of the fundamental is always larger than that for harmonics in gas target.

The term Δk_{geom} concerns the focusing geometry of the driving laser [92]. The Gouy phase shift induced by passing through a focus of the focused Gaussian beam is:

$$\Psi(z) = \arctan^{-1}(\frac{z}{z_R}) \tag{4-10}$$

where z is the distance to the laser focus and $z_R=\pi\omega^2/\lambda$ is the Rayleigh length. So, the phase mismatching due to this Gouy phase shift is given by:

$$\Delta k_{geom} = q k_{geom}(\omega) - k_{geom}(q\omega) = \frac{q}{z_R(1+(\frac{z}{z_R})^2)} \tag{4-11}$$

Of course, this term is always positive. The contribution from this term can be reduced if a longer focal length is used since a loose focus results in a larger focus size. In our case, a loosely focusing geometry is applied so that the geometrical phase mismatching is very small.

The term Δk_{plasma} represents the phase mismatching from the plasma contribution since the plasma has different refractive index properties depending on the frequencies. A certain amount of neutral atoms will be ionized and the free-electron dispersion will result in a change in the refractive index.

A refractive index due to plasma generation can be written as:

$$n_{plasma} = \sqrt{1-(\frac{\omega_p}{\omega})^2} \tag{4-12}$$

$$\omega_p = \sqrt{\frac{e^2 n_e}{\epsilon_0 m_e^*}} \tag{4-13}$$

where ω_p is the plasma frequency, n_e is the density of electrons, e is the electric charge, m_e^* is the effective mass of the electron, and ϵ_0 is the permittivity in free space [93]. The phase mismatching from plasma is given by:

$$\Delta k_{\text{plasma}} = q k_{plasma}(\omega) - k_{plasma}(q\omega) = \frac{\omega_p^2(1-q^2)}{2qc\omega f} \approx -qPN\eta r_e \frac{2\pi\omega}{c} \quad (4\text{-}14)$$

where r_e is a classical electron radius. It is easy to see that the phase mismatching has a negative sign and this term also depends on the pressure of the target.

Another term concerning the atomic dipole phase is Δk_{dipole}. The dipole moment can be written in terms of the quasi-classical action S as [94]:

$$\vec{x}(t) \propto \int_0^\infty d\tau e^{-iS(\vec{p},t,\tau)} \quad (4\text{-}15)$$

where p is the momentum, τ is the time at which the electron makes a transition to the continuum, and t is the time for the wave function to propagate in the field. The quasi-classical action term, S, which describes the motion of electrons moving in a laser field with a constant momentum p is given by:

$$S(\vec{p},t,\tau) = \int_\tau^t dt' \left(\frac{mv(t')^2}{2} + I_p\right) \quad (4\text{-}16)$$

The Fourier transform of $\vec{x}(t)$ gives signal of the q_{th} harmonic:

$$x_q = A_q e^{i\Phi_q} \quad (4\text{-}17)$$

where A_q is an amplitude and the term Φ_q ($=\omega_q \times t - S_q$) is the atomic dipole phase. For the long and short trajectories, the phase term can have two values. The quasi-classical action, S, can be expressed as:

$$S(\vec{p}, t, \tau) \approx U_p \tau + \cdots \tag{4-18}$$

where U_p is the ponderomotive energy [95]. Since U_p is linearly dependent on the laser intensity, this classical action is also linear in intensity. Thus, the atomic phase can be simplified to:

$$\Phi_i(r, z, t) = -\alpha_i I(r, z, t) \tag{4-19}$$

where i represents either the short or long trajectories, α is the slope of the phase as a function of the laser intensity and z is the longitudinal position. The wave-vector mismatch for the atomic dipole phase can be calculated as:

$$\Delta k_{dipole} = \frac{d\Phi_i(r, z, t)}{dz} = q\alpha I\left(\frac{2zz_r^2}{(z_r^2 + z^2)^2}\right) \tag{4-20}$$

Here, we just neglect the last phase mismatching term caused by nonlinear effects. Thus, all terms contributing to phase mismatching have been derived. These terms can be used to cancel each other, resulting in the total mismatch being minimized since they have different signs. By minimizing the phase mismatching, the phase matching conditions can be attained to be implemented to the experimental parameters such as the target gas pressure, laser focus position, laser intensity, the interaction length and the gas cell diameter. Figure 4.15 shows the electric field for a 15 fs driving laser, which is used for the phase matching calculation.

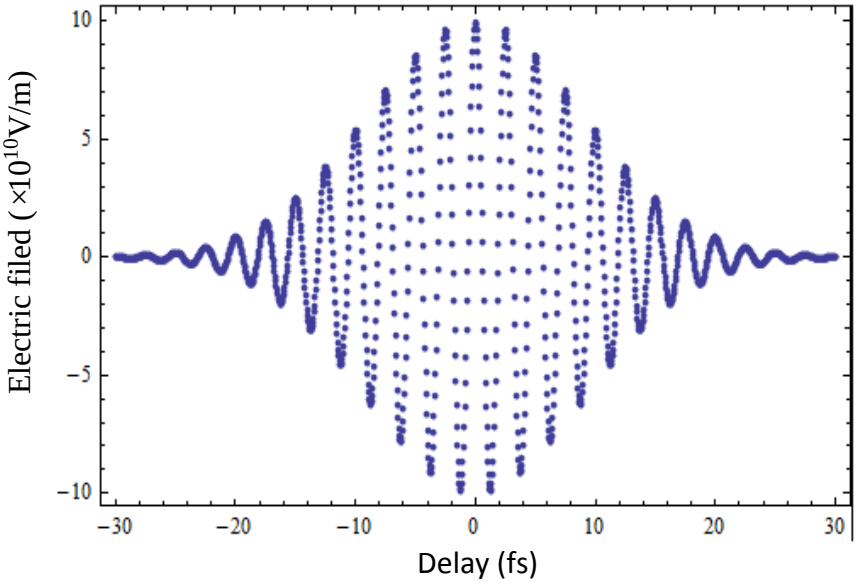

Figure 4.15 Calculated electric field for the 10Hz driving laser.

Figure 4.16 shows a plot of the Gouy phase, dipole phase, plasma and atomic (neutral medium) phase as a function of z, as well as the total phase. At z=0, the laser focus exists. The parameters are an 18 fs, 800 nm laser focused to a beam diameter of 5 mm with an intensity of 1.6 x 10^{14} W/cm^2. This peak intensity is corresponding to a photon energy cutoff of 50 eV. From the ADK calculation, the ionization probability of the gas is about 3%. The Guoy phase shift term is very small since the gas target is placed out of the focus, where a total flat phase is shown. However, if the gas target is placed after the focus, the degradation in the laser beam profile propagating in the gas medium will result in the lower conversion efficiency due to the defocusing of the plasma in the focus. The HHG flux with much stronger signal can be generated by simply choosing the appropriate focus position respect to the gas medium.

The coherence length was demonstrated in Fig. 4.17. The red arrow drawn on the plot represents a typical ~90mm interaction region over which we wish to generate harmonic flux.

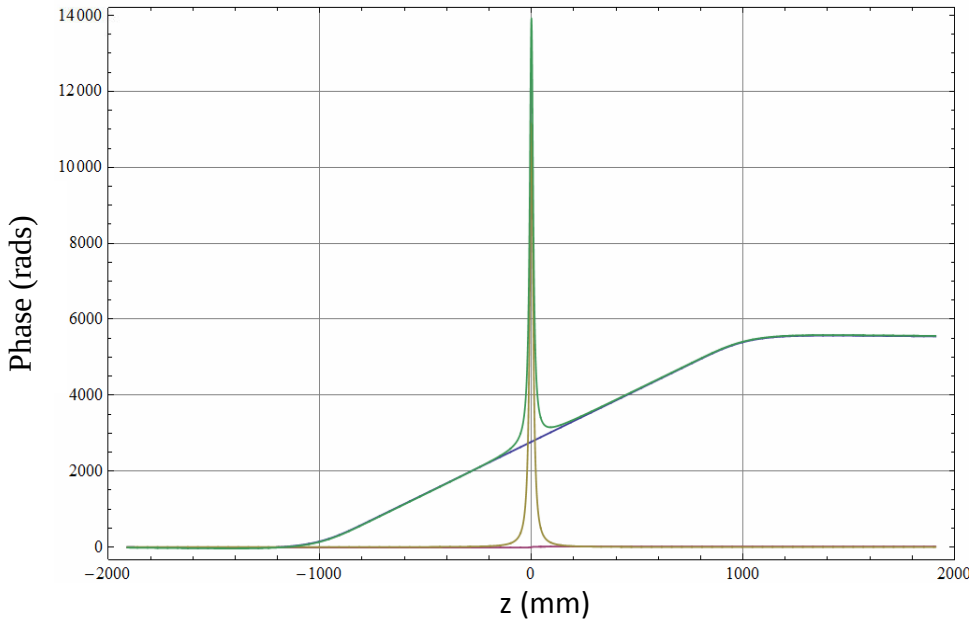

Figure 4.16 Total phase (green line), Gouy phase (dark-red line at the bottom), dipole phase (tan line), plasma and atomic phase (blue line) as a function of the z distance. The gas pressure is ~ 4.5 torr

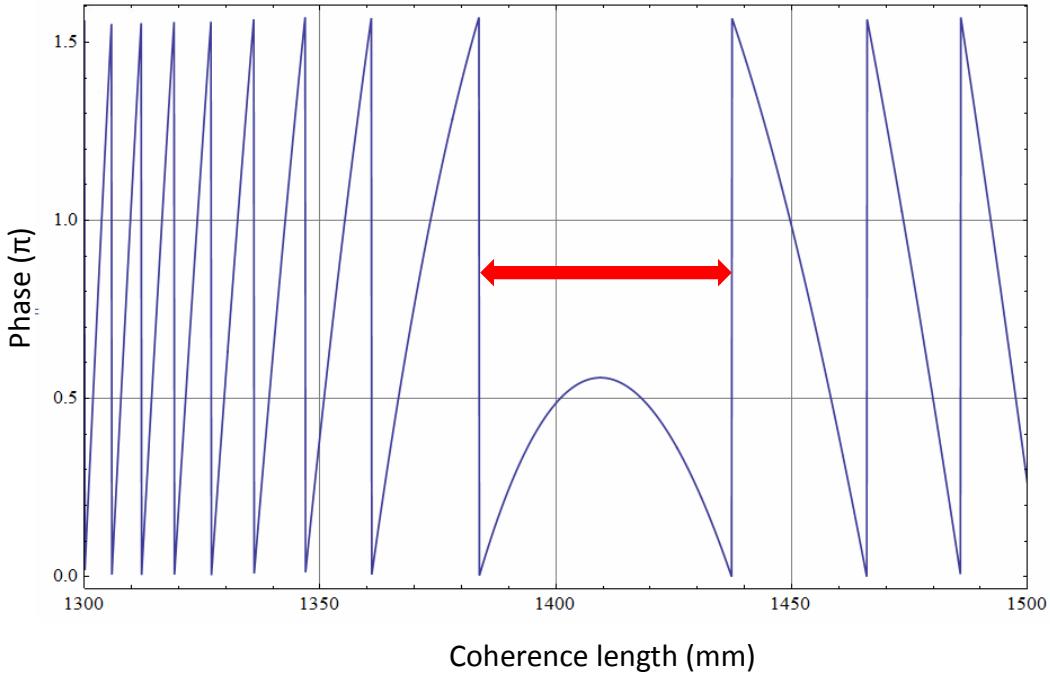

Figure 4.17 A calculated coherence length inside the HHG chamber with a gas pressure of 4.5 torr.

The output energy of the HHG is proportional to $[A_q(z)]^2$, where $A_q(z)$ is the field strength of the qth harmonic. And it was determined by:

$$\frac{dA_q(z)}{dz} + \frac{\alpha}{2}A_q(z) = iN_0 d(q\omega)\exp(i\Delta kz) \tag{4-21}$$

where $d(q\omega)$ is the dipole moment, α is the absorption coefficient for the qth harmonic, ω is the frequency of the fundamental laser, and Δk is the total phase mismatching wave vector. The second and third terms in this equation are corresponding to self-absorption and phase matching, respectively. The total photon number N_q of the qth-order harmonic per unit of time and area can be derived from that equation and can be written as [96]:

$$N_q \sim N_0^2 L_{med}^2 |d(q\omega)|^2 \left[sinc(\frac{\Delta k L_{med}}{2})\right] \tag{4-22}$$

where L_{med} is the length of the gas medium and N_0 is the neutral gas density. As a result, to increase the HHG flux, it is critical to increase the density and length of the gas under the phase-matching condition since the total photon number is quadratically dependent on the gas density and medium length.

When the coherence length is maximized, the HHG flux is limited by re-absorption in the target gas. The absorption length, L_{abs}, is defined by:

$$L_{abs} = \frac{1}{2\alpha} = \frac{\kappa T}{p\sigma_{ion}} \tag{4-23}$$

where κ is the Boltzmann constant, T the temperature, and σ_{ion} the ionization cross-section. In our experiment, the gas medium length is much longer than the absorption length. The total photon number for the qth harmonics is given by [96]:

$$N_q \sim N_0^2 L_{med}^2 |d(q\omega)|^2 \frac{4(L_{abs}L_{coh})^2}{L_{coh}^2 + (2\pi L_{abs})^2} \times [1 + \exp\left(-\frac{L_{med}}{L_{abs}}\right) - 2\cos\left(\frac{\pi L_{med}}{L_{coh}}\right)\exp\left(-\frac{L_{med}}{2L_{abs}}\right)] \quad (4\text{-}24)$$

This equation indicates that when the coherence length and the absorption length are comparable, the total photon number N_q saturates if the medium length is longer than the absorption length. Thus, to increase the HHG flux, the coherence length is much longer than the absorption length. Usually, the medium length, L_{med}, is at least three times of the absorption length. In this case, we can define an optimum medium length under the phase-matching conditions, $L_{med}^{opt} = 3L_{abs}(p_{match})$. In this case, the HHG energy yield can be expressed as [52, 89]:

$$N_q \sim N_0^2 L_{med}^2 |d(q\omega)|^2 z_R \sim |d(q\omega)|^2 S_{spot} (PL_{med})^2 \quad (4\text{-}25)$$

where z_R is the Rayleigh length, S_{spot} is the beam area of the driving laser inside the gas medium and P is the gas pressure. So, the HHG flux is proportional to the driving laser beam size and the squares of the medium length pressure product. It is also proportional to the square of the dipole strength for the qth harmonic order. The dipole strength is assumed to follow [97]:

$$d(q\omega) \sim (1 - \eta) \times I_0^{5\sim6} \quad (4\text{-}26)$$

where η is the ionization probability and I_0 is the laser intensity inside the gas medium. As a result, the laser intensity should be set at an optimum value near the ionization threshold of the gas medium. The ionization probability is ~2-10% for the gas medium. With a higher ionization probability, the negative dispersion due to free electrons will break the phase-matching conditions and decrease the target atomic gas density. On the other hand, the maximum value of the pressure length product is limited strictly by self-absorption by the gas medium itself. Consequently, the

only way to increase the HHG flux is to increase the interaction area. However, the increase of the spot size will result in the decrease of Gouy phase since the Gouy phase is given by:

$$\Delta k_{Guoy} = \frac{q}{z_R(1 + (\frac{z}{z_R})^2)} \tag{4-27}$$

Thus, the gas pressure needs to be chosen properly to cancel the reduced geometrical phase shift of the driving laser to meet a phase-matching condition. In experiment, we have to decrease the gas pressure to maintain the phase-matching condition while we must increase the interaction length to keep the pressure length product as a constant.

4.3 High Flux Attosecond Pulse Generation

As we discussed above, the energy scaling method can be applied to HHG in the neutral gas and the increase in harmonics energy is linearly dependent on the geometrical focusing area of the driving laser. As a result, a loosely focused beam with an excellent beam quality is required under the phase-matching condition. The experimental set up is shown in Fig. 4.18. It consists of four sections: the laser system, HH generation, application and diagnostics. The sections are connected by vacuum tubes and chambers, pumped by turbos from Leybold GmbH.

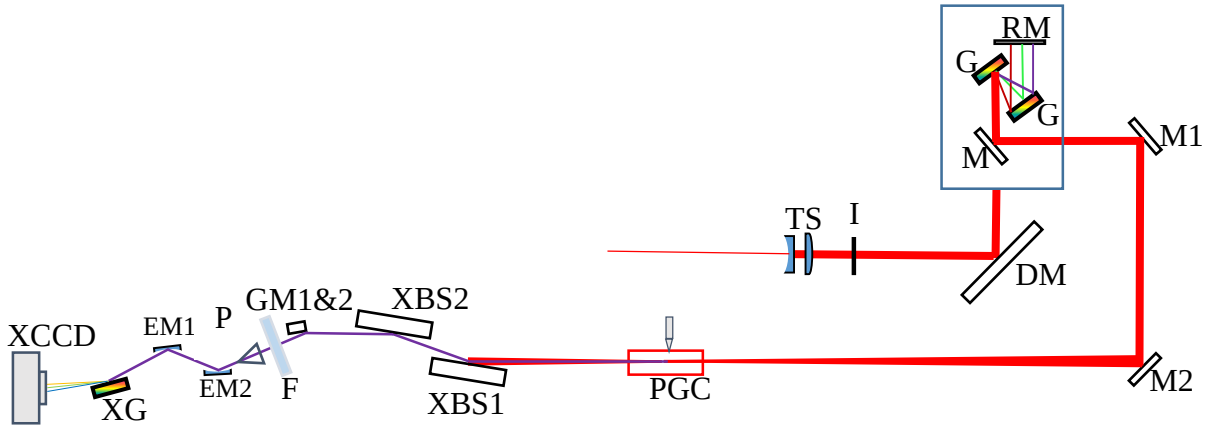

Figure 4.18 Experimental setup with the 25 m focusing configuration; TS - telescope, I - iris, DM - deformable mirror, M1 & M2 - folding mirror, G - grating, RM - roof mirror, PGC - pulsed gas cell, XBS1 & XBS2 - XUV beam splitter, GM1&2 - two gold mirrors, F - aluminum filter, P - XUV photodiode, EM1 and EM2 - ellipsoidal mirror, XG - XUV grating, XCCD - XUV CCD camera.

The pump or driving pulse was loosely focused by a telescope, which includes one negative plano-concave and one positive plano-convex lens with a focal length of 600 mm and 1600 mm, respectively. And by varying the separation of these two lenses, a tunable focal length from 10 to 100 meters can be achieved. This is of great importance to control the beams size, which allows for re-adjustments of the focusing geometry and the intensity distribution at focus. We can adjust the separation of the telescope to optimize the position of the laser focus relative to the gas tube along the propagation direction. Thus it makes us optimize the phase-matching condition and increase the XUV pulse energy in a simple way. Our HHG setup is designed to work in a loosely focused geometry into the interaction tube with a 25 m focal length. The pump beam size was increased to 68 mm before the compressor by the telescope to avoid the damaging on the optical components.

The driving laser beam can be apertured down by a variable diameter iris. It allows us to control the beam size so that we can re-adjust the focusing geometry, beam profile, laser energy and intensity distribution inside the gas medium. Two corner mirrors (M1 and M2) placed in two vacuum chambers are used to direct the driving laser into the generation chamber. These mirrors are designed and customized by us. They can not only provide a high reflectivity with high damage threshold but also a broad bandwidth to support the wide spectrum for the pulse duration of sub 15 fs. Two home-made mirror mounts with motorized knobs enable us to control the beam pointing by a computer to fine-tune the mirrors. After the two folding mirrors, the beam enters the generation chamber. The generation chamber is connected to the laser compressor chamber by vacuum tubes and chambers without any optical window, which will avoid self-phase modulation in the window induced by the intense focused laser. Since the laser beam propagates in vacuum, the B-integral is minimized. The focused beam then interacts with the rare gas confined in a glass gas tube. The interaction gas tube has a diameter of 4.6 mm and a length of 100 mm.

The gas tube is mounted on an optical mount with two knobs adjustable by feedthroughs. This mount is connected to an adaptor controlled by a XYZ manipulator. So, we can control the tilt and position of the tube with respect to the incoming laser beam. The HHG chamber is connected on both side by two very flexible bellows, which will allow us to optimize the position of the gas tube. The gas was released at a repetition rate of 10 Hz by a valve driven by a piezo-electric actuator and synchronized with the laser pulses as shown in Fig. 4.19 (from the Lee company). To maximum the HH signal, we optimized the opening and closing times.

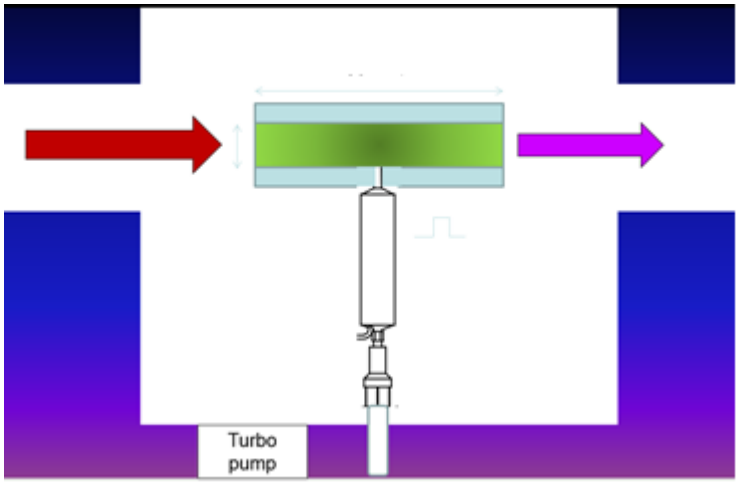

(a)

(b)

Figure 4.19 (a) a diagram of the gas tube configuration inside the HHG chamber, (b) the picture of the gas tube with a pulsed gas jet connected.

In fact, it is designed to work simultaneously with two gas jets to increase the gas pressure inside the gas tube. A CCD camera with a filter is applied to monitor the filamentation inside the gas tube. Figure 4.20 illustrates the observation of the laser induced filamentation (the bright line) inside the gas tube.

Figure 4.20 Filamentation induced by focusing a driving laser through the 10 cm long gas tube filled with argon gas.

The HHG beam then propagates collinearly with the driving laser in vacuum. Another challenge is the separation of the high-intensity driving laser pulse with the co-propagating harmonics. It is necessary to reduce the intensity of the driving laser pulses to less than a hundred of gigawatts per square centimeter to avoid damaging the XUV optics or a sample placed in the beam. Typically, the driving laser will be eliminated by one or more thin aluminum filters with a thickness of 200 nm or more. But these filters cannot survive with a laser energy of hundreds of mJ or higher.

Nagata *et al* reported a beam splitter (BS) for wavelengths shorter than 30 nm, which uses a 10 nm thick niobium nitrogen (NbN) film prepared on a Si substrate [98]. However, the low

damage threshold of Si restricted the boosting of the pump laser up to the J level. So, we designed an XUV BS to attenuate the fundamental while attaining the high-throughput for XUV sources. Tantalum pentoxide (Ta_2O_5) is a high-quality thin film material which can be prepared by sputtering on fused silica (SiO_2) substrate [21]. The BS was coated with 5 film layers of SiO_2 and Ta_2O_5, alternatively. It has an attenuation ratio of 1% and a damaging threshold intensity of at least 100 TW/cm^2 for 20 fs pump pulses.

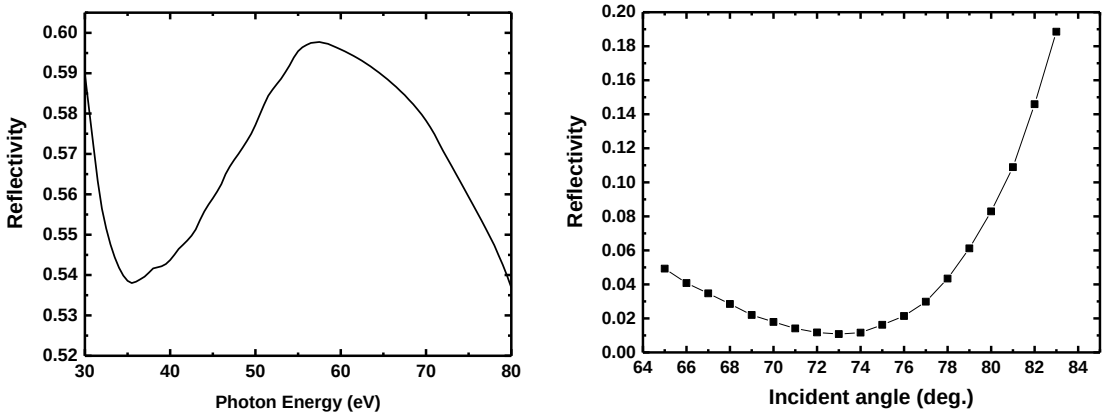

(a) (b)

Figure 4.21 (a) Calculated reflectivity for XUV BS as a function of the XUV photon energy at the incident angle of 73^o, (b) Measured reflectivity of XUV BS as function of the incident angles for the pump pulses.

Figure 4.21 (a) shows the calculated reflectivity of Ta_2O_5 film deposited on SiO_2 substrates as a function of the wavelengths for the p-polarized radiation. The actual reflectivity may be smaller than calculated one because of the roughness on the coating surface. Reflectivities of the 20 fs, 800nm pump pulses were measured as a function of the incident angle presented in Fig. 4.21 (b). The minimum reflectivity was 1%, which was achieved at an incident angle of 73^o. A second BS is placed orthogonally to the first one to attenuate s-polarized driving laser, considering the

gating technique for the isolated attosecond pulses in near future as shown in Fig. 4.22. Two absorption filters are placed between the XUV BS and mount to absorb the transmitted driving laser, eliminating the reflection from the mount surface. Another absorption filter with a 3 mm hole in the center is placed between them to block most of the residual IR from the first BS while transmitting all the reflected XUV. These beam splitters can also be adjusted by motorized knobs to fine-tune the XUV beam pointing propagating in the end station.

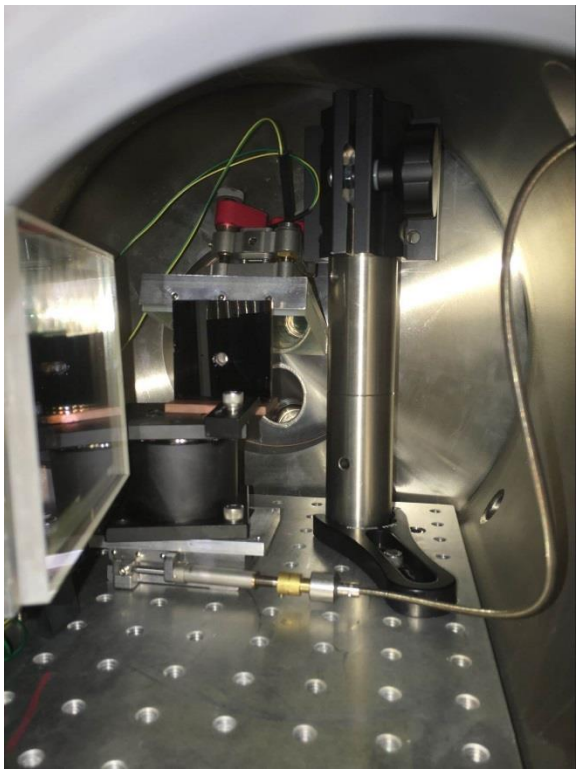

Figure 4.22 Two orthogonally placed XUV BS inside the chamber.

4.4 High Flux Attosecond Pulse Characterization

The XUV beam then is sent into a high vacuum end station that will split the pulses with precision timing and focus the pulses to spot sizes as small as one micron as shown in Fig. 4.23.

There are three major sections for this end station: (1) split mirror chamber, (2) experimental chamber, (3) XUV spectrometer.

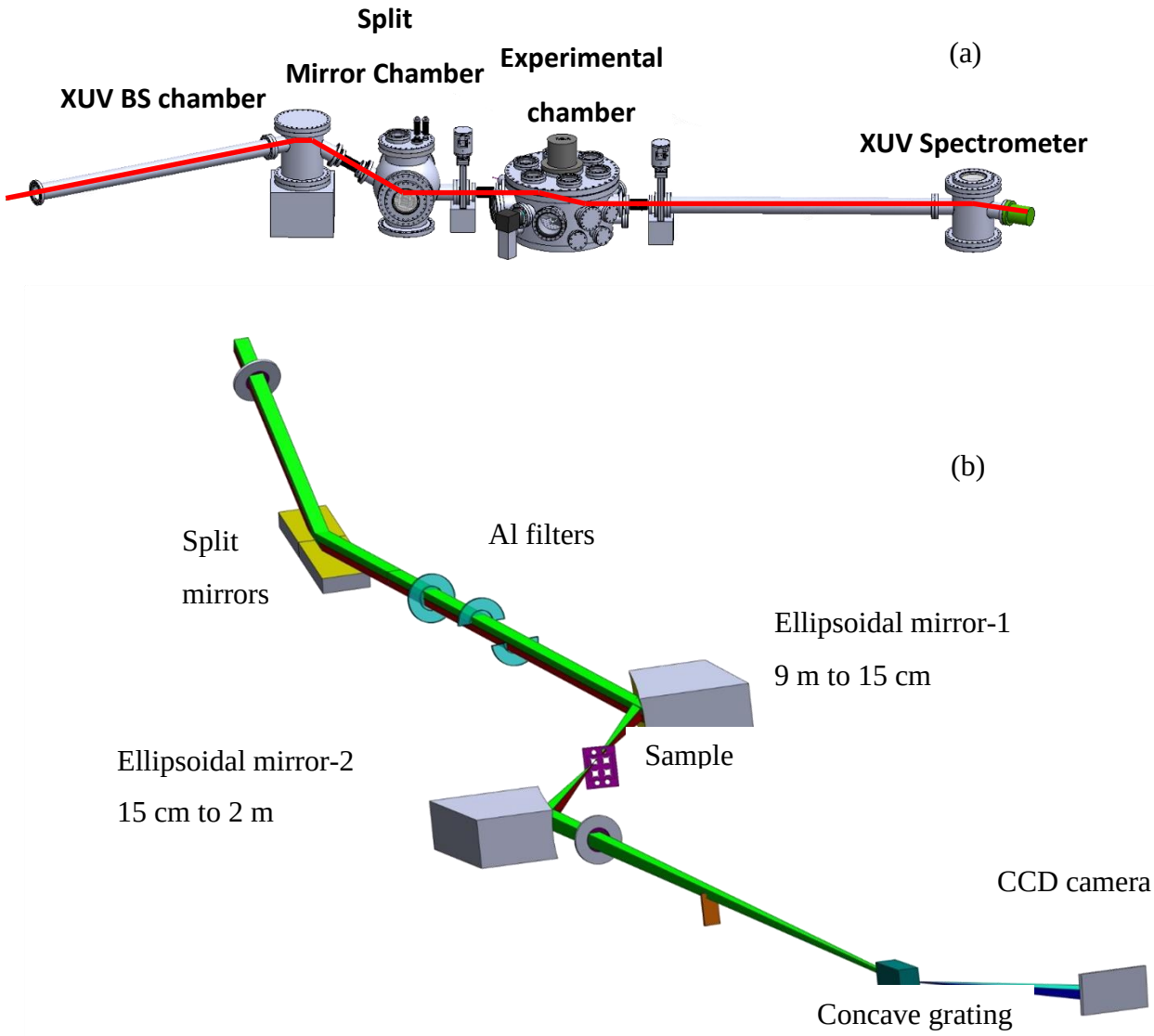

Figure 4.23 (a) diagram for the attosecond end station, (b) optical components inside.

The end station system has integral capability for streak field detection to verify the attosecond pulse durations and phase characteristics, as well as x-ray spectrometers for spectral bandwidth measurements. To perform true attosecond-attosecond pump-probe measurements, one

pulse is used to initiate a process, and a second attosecond pulse is used to probe the time dynamics of the electron correlation, either in transient absorption or by photoelectron spectroscopy. This design utilizes a pair of grazing incidence split mirrors to generate two identical broad band isolated attosecond pulses. One of them creates the delay (Δt) by slight displacement (d) of the total distance traveled and the second to compensate for spatial displacement of the two pulses as shown in Fig. 4.24.

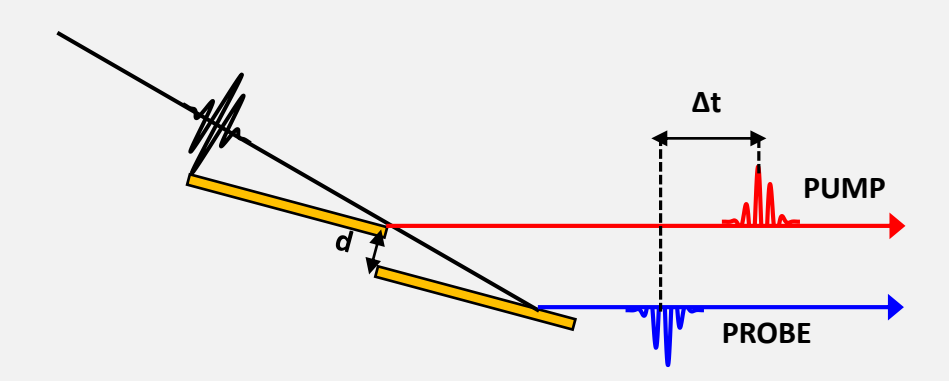

Figure 4.24 Time delay induced by two split mirrors.

These pulses are recombined at the sample, and then diverge again onto a grating and x-ray camera. The XUV reflectivity by these two split mirror are show in Fig. 4.25.

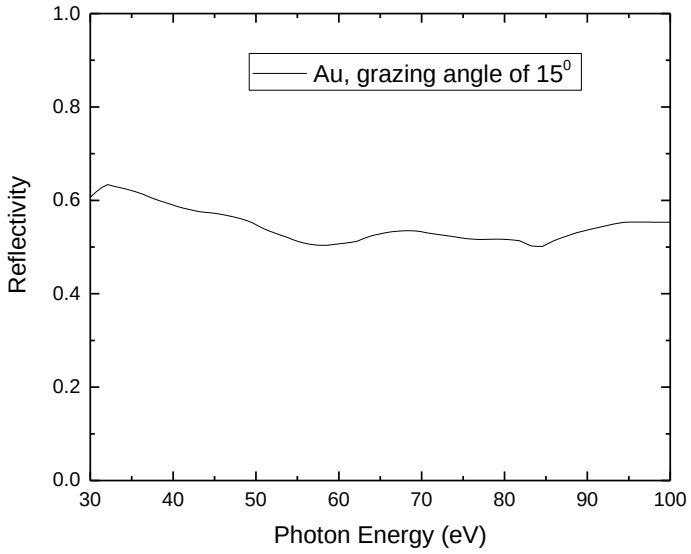

Figure 4.25 Split mirror reflectivities as a function of the s-polarized XUV photon energy [21].

These two fused silica mirrors with gold coatings mounted on motorized piezo stages with nanometer precision control were placed inside the split mirror chamber and work as the split mirrors as shown in Fig. 4.26. The stages have a 5-axis alignment for an overlap. The delay is applied using these stages, keeping the delayed part of the mirror parallel to the stationary part. The spatial overlap of the pump and probe pulses occurs at a small angle to maintain the high temporal resolution. For a 1-micron spot size and 100 as time resolution, the angle must be less than only 30 mrad by a calculation. Figure 4.25 (b) demonstrates the split mirror piezo stability test results. A RMS deviation of 9.3 nm corresponding to 15 as time delay jitter was obtained by a He-Ne laser. After the split mirrors, two metal holders mounting Al filters were designed to completely remove the residual IR from XUV and attenuate an XUV intensity through the selective pump and probe

filters with different thickness. At the present time, the attosecond spot size in most experiments is not carefully controlled [73, 99]. In the experimental chamber, a pair of Kirkpatrick-Baez mirrors was designed to have the capability to focus attosecond pulses to spot sizes of one micron [100]. This will achieve sufficient energy density to initiate the phase change in the sample directly with the attosecond pulses. It is enabling nonlinear optical experiments using attosecond pulses in the future, as well as applications to plasmonics and magnetics [28].

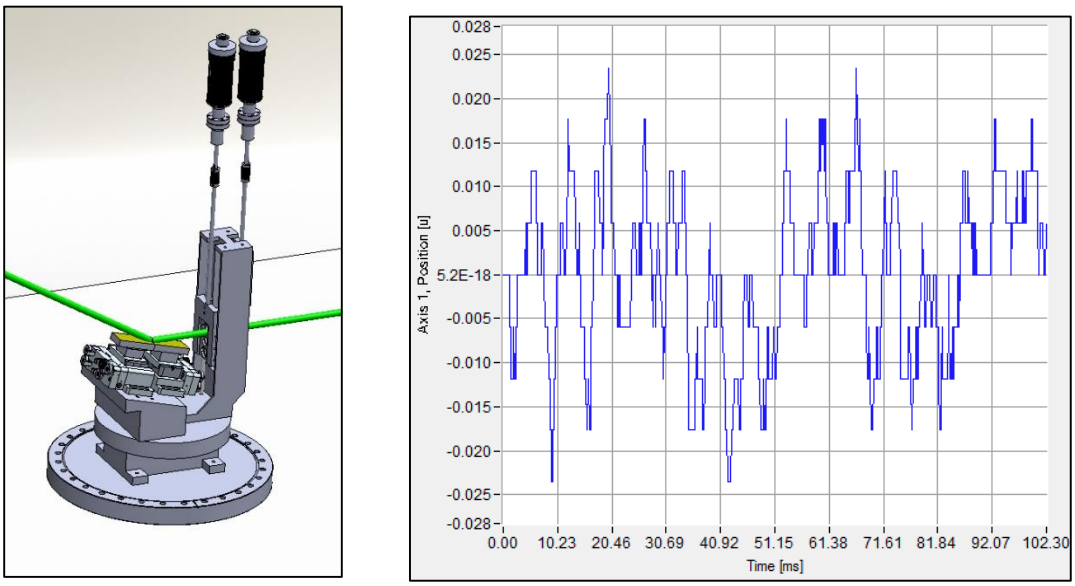

(a) (b)

Figure 4.26 (a) components inside the split mirror chamber, (b) split mirrors piezo stability test.

The Kirkpatrick-Baez mirrors consist of two ellipsoidal mirrors as shown in Fig. 4.23 (b). The first mirror has two focal lengths of 9 m and 15 cm, respectively while the second one has 15 cm and 2 m focal lengths. The gas tube generating XUV sources is placed at the first focal point, and the XUV beam will refocus at the second focal point. The gold coating features broadband

high reflection for attosecond pulses. The second ellipsoidal mirrors will image the focus into the XUV spectrometer in the end. The interaction region is designed to accommodate both solid and gas phase experiments. A motorized stage with a solid sample and gas tube holder is placed near the focus of the ellipsoidal mirror as shown in Fig. 4.27.

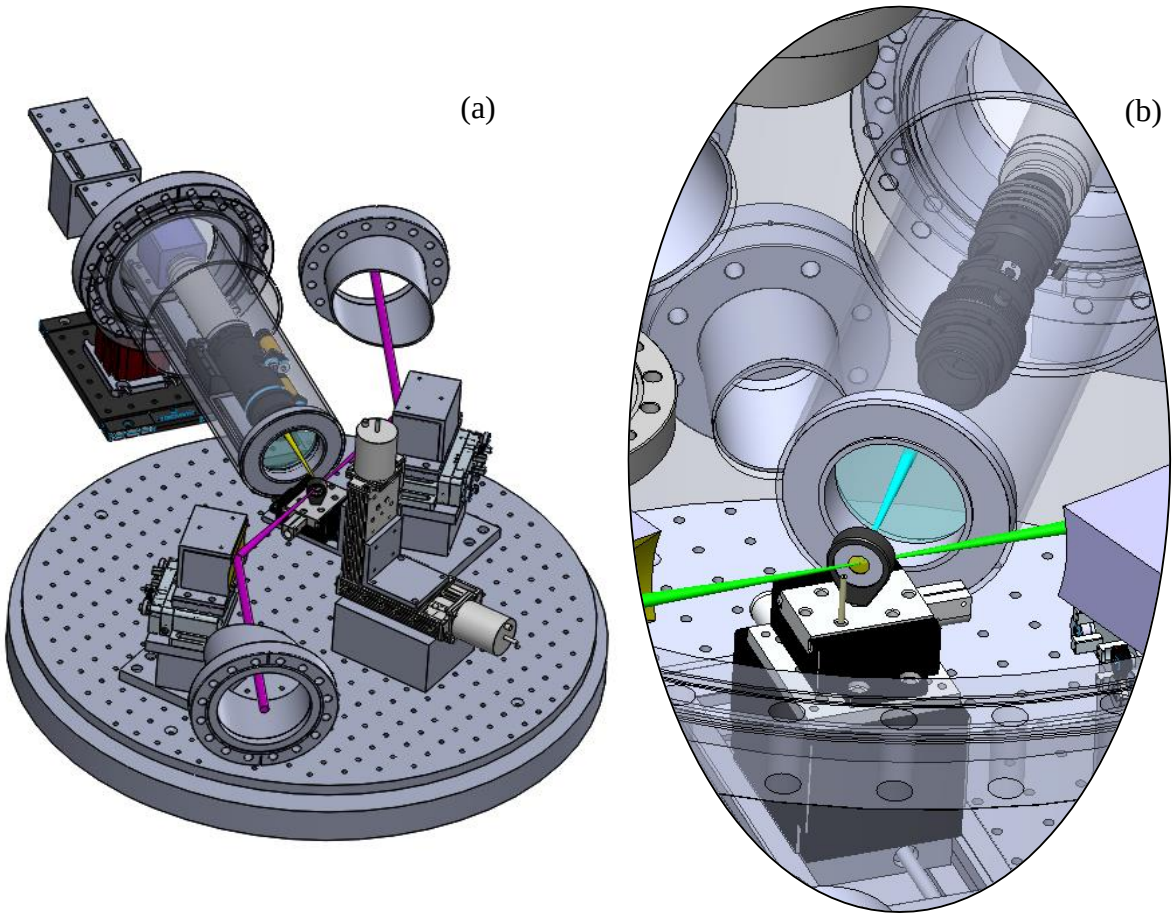

Figure 4.27 (a) Kirkpatrick-Baez mirrors in the experimental chamber and (b) a focus characterization with a scintillator by a long range microscope.

To measure the focusability of the XUV pulses by the first ellipsoidal mirror, a long range microscope will be used to an EUV camera to observe the spot induced by the focused XUV pulses on a Ce:YAG scintillation screen as shown in Fig. 4.27 (b) [101].

A time-of-flight mass spectrometer as shown in Fig. 4.28 is under installation and initial characterization measurements are designed around rare gases to realize attosecond-attosecond pump-probe delays, allowing measurements of ejected photoelectrons under multiphoton conditions for characterization of attoseond-attosecond pump-probe overlap [102]. The two photon double ionization of xenon and 2nd order autocorrelation experiment will be carried out in the near future.

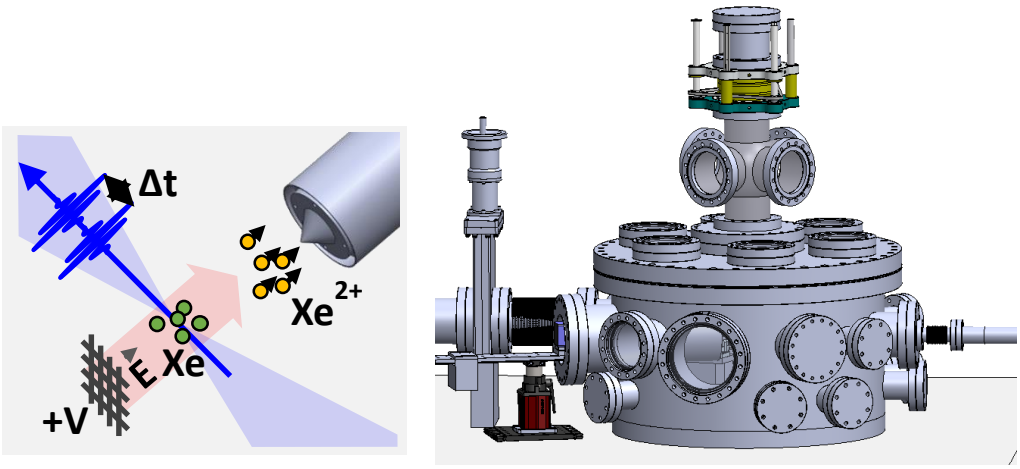

Figure 4.28 The time-of-flight mass spectrometer design.

After the focus, both pulses continue to diverge and hit the variable-line-space grating, which spatially disperses the frequency components of each pulse and focuses them into two different vertical positions on an XUV CCD camera. This XUV spectrometer is one of the most

critical parts in the experiment, which must have a high energy resolution in the energy range of interest. The spectrometer is depicted schematically in Fig. 4.29. A grazing incidence, aberration corrected concave grating (Hitachi 001-0640 XUV) was used to form the flat field spectrograph and the dispersed XUV spectra was recorded by an XUV CCD camera (Princeton Instruments PIXIS 400B). This grating has a flat-field spectrum range of 11-62 nm (20-112 eV).

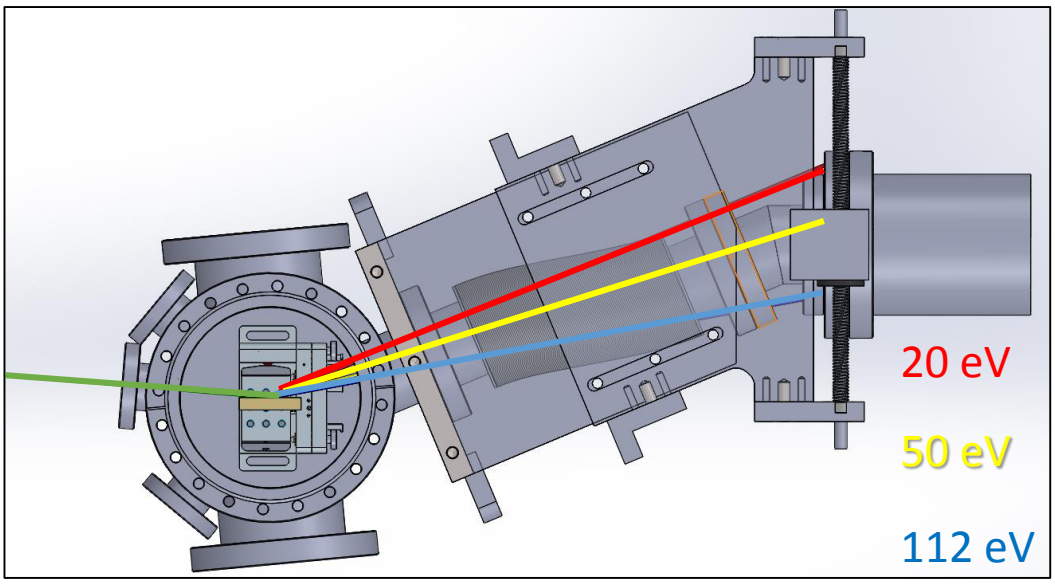

Figure 4.29 Schematic of the flat-field grazing incidence reflection grating spectrometer.

In order to calibrate the energy range and resolution, the XUV spectrum after absorption by neon gas was measured as shown in Fig. 4.30. A resolution of 25 meV at 45.5 eV was obtained [103].

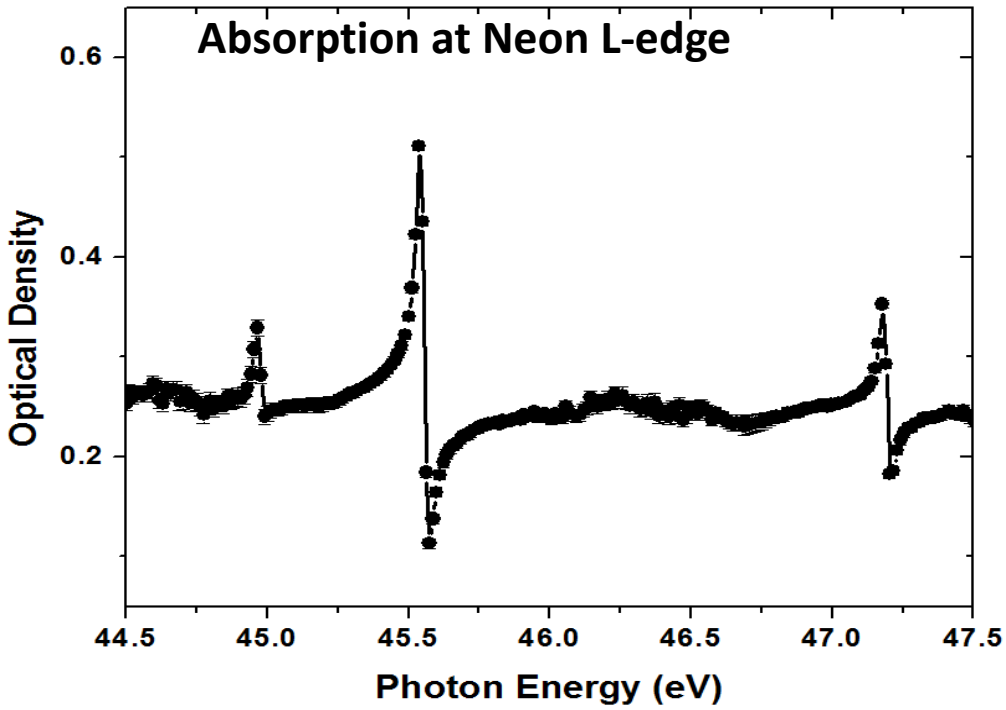

Figure 4.30 The measured absorption of Neon with a resolution of 25 meV.

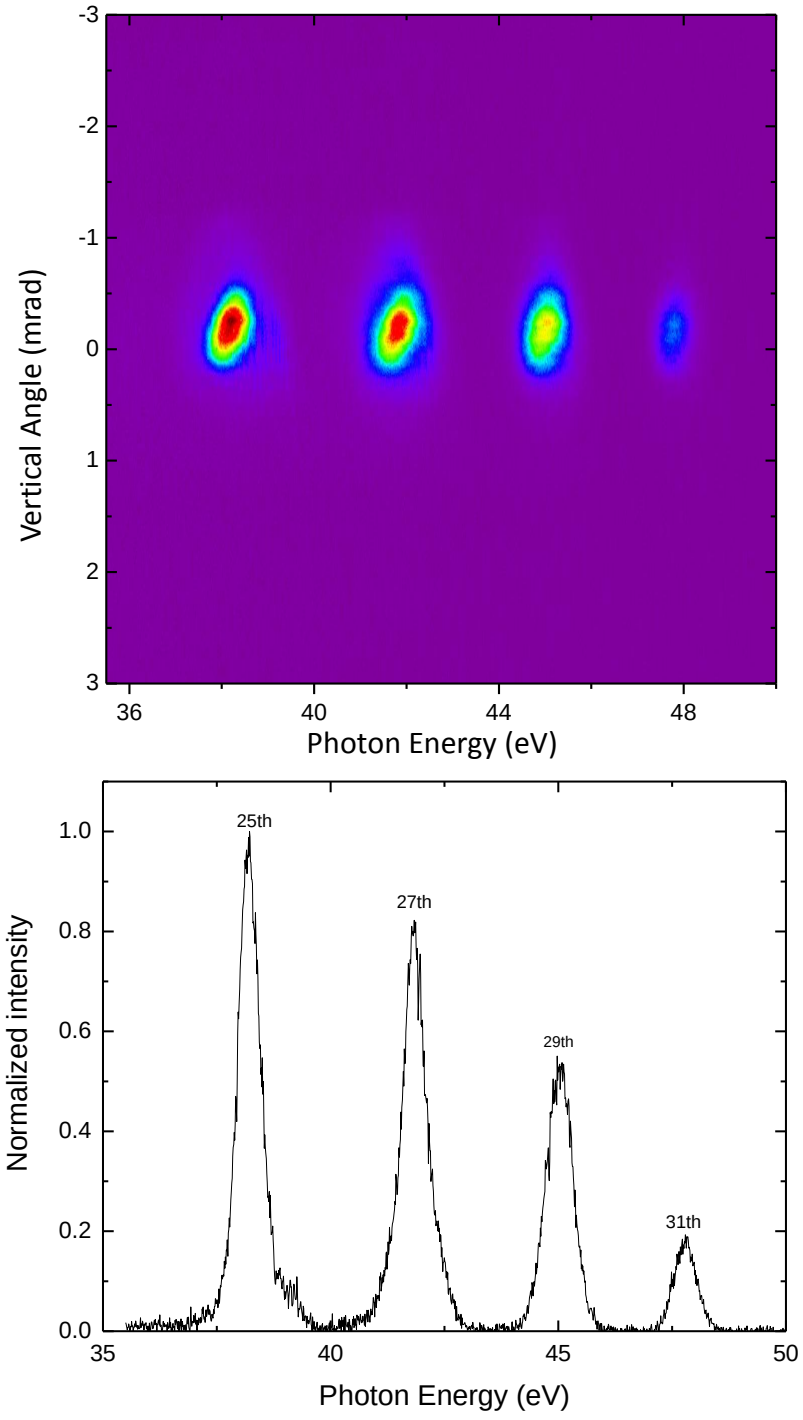

Figure 4.31 Experimental obtained harmonic spectrum in argon gas (top) and the measured harmonic spectrum distribution. The profile is normalized by the 25th-harmonic signal. (bottom).

A typical HHG spectrum in argon gas was shown in Fig. 4.31, including four odd harmonic orders. This spectrum was recorded by the XUV camera. The driving pulse energy is about 40 mJ with a beam diameter about 600 μm (FWHM) and the peak intensity is ~ 4×10^{14} W/cm^2. The background pressure inside the HHG chamber is ~ 6×10^{-5} torr.

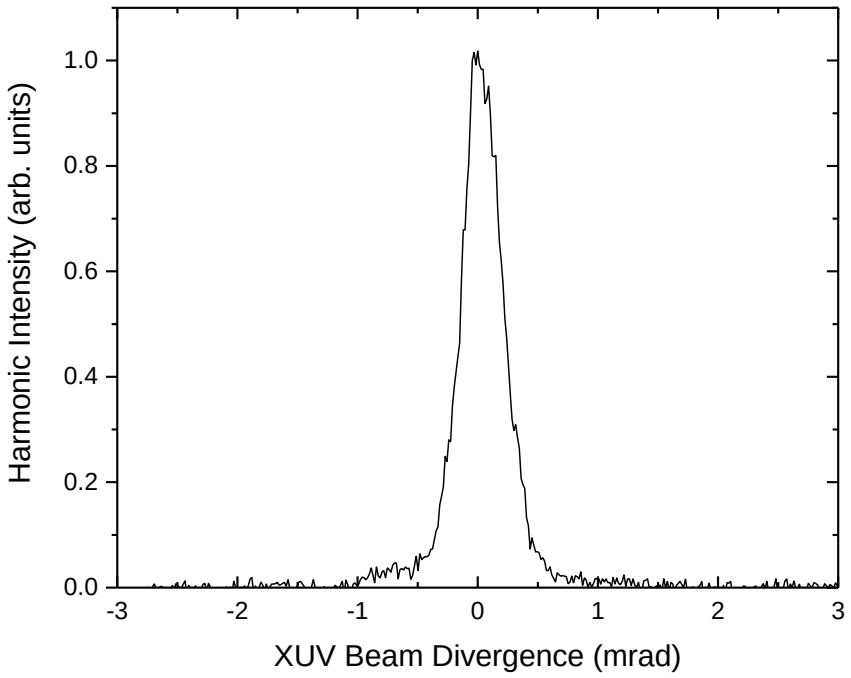

Figure 4.32 Normalized 1D distribution of the 25rd harmonic in Ar gas.

Figure 4.32 depicts the far-field spatial profile of the 25th harmonic. The profiles were integrated with respect to wavelength. The output beam divergence was estimated to be ~ 0.4 mrad (FWHM) with a Gaussian-like profile. The good beam quality indicates that the phase-matching condition is satisfied.

The beam emittance of HHG under the phase matching condition is proportional to the medium length and is related to a non-collinear angle of HHG. This kind of phase matching is called the "Cerenkov" phase matching. The phase mismatch is given by [12]:

$$\Delta k = k_q - qk_1 - \frac{q\pi\theta^2}{\lambda} \tag{4-28}$$

where θ is the non-collinear angle of HHG. Under the phase-matching condition ($k_q \sim qk_1$), the beam divergence angle is proportional to $1/\sqrt{L_{med}}$.

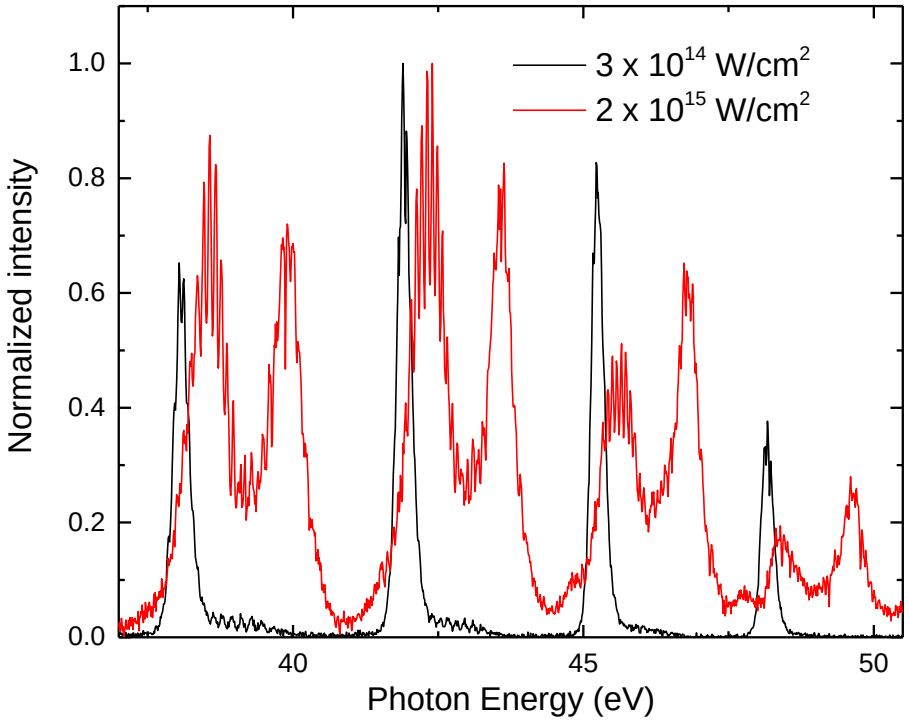

Figure 4.33 Measured harmonic spectra in argon medium with different driving laser intensities: 3×10^{14} W/cm^2 (black line) and 2×10^{15} W/cm^2 (read line).

When the driving laser intensity is well above the saturation intensity of argon (3.51×10^{14} W/cm^2), we observed the spectral broadening, blue shift and line splitting structures in high harmonics generated in argon gas as shown in Fig. 4.33 [104]. The spectral splitting is mainly induced by the propagation effects of HHG in the rapidly ionizing gas medium. If the driving laser intensity is far over the saturation intensity of argon, a volume of electron plasma with a time-dependent density will be produced in the interaction regime. The refractive indexes of HHG in gas medium are strongly time dependent due to the rapid ionization of the gas medium. Therefore, the high harmonics are chirped along their propagation through the ionizing gas medium, resulting in the spectra splitting.

In order to maximize high-order harmonic energies under the phase-matching condition, we investigated the dependence of the intensity of harmonics generated in argon as a function of the gas pressure and laser energy. The results were demonstrated in Fig. 4.34. The signal is normalized to the maximum obtained counts.

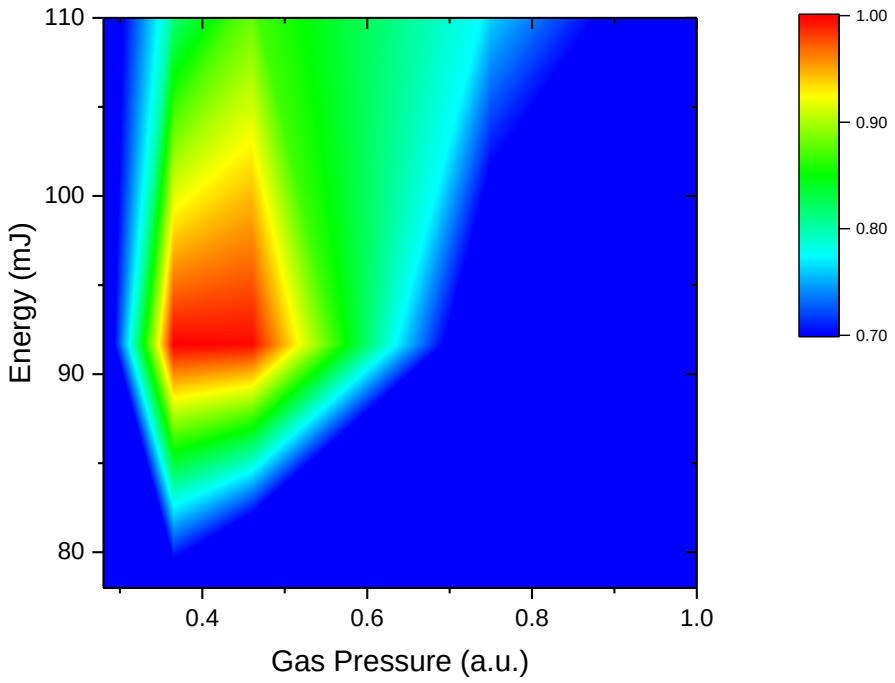

Figure 4.34 Intensity of the HHG generated in argon as a function of driving laser energy and generation gas pressure.

The optimized gas pressure had a finite tuning range which was explained by the phase-matching conditions and target gas re-absorption as discussed before. When the gas pressures are higher than the optimal gas condition, HHG is gradually decreased by the absorption of neutral atoms. When the laser intensity reaches the saturation intensity of argon, most of the atoms are fully ionized, resulting in breaking the phase matching condition due to the plasma dispersion. Therefore, it leads to the decrease of the conversion efficiency.

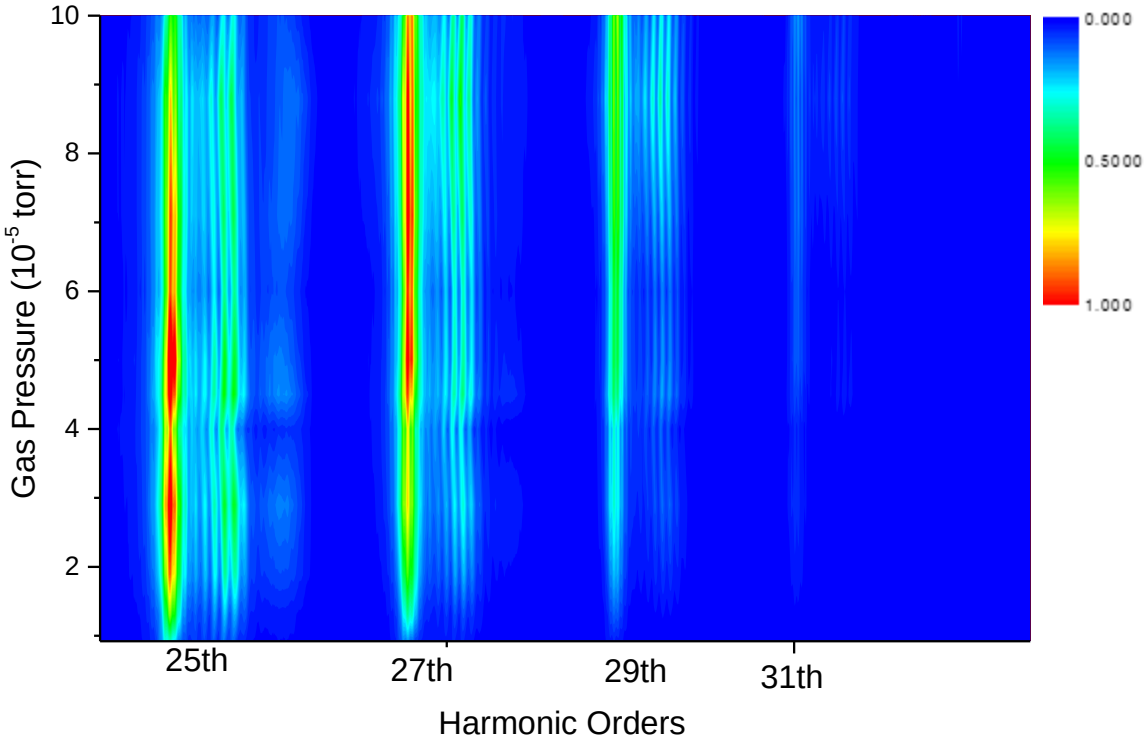

Figure 4.35 Pressure dependence of different harmonics in argon. The pulse energy is ~ 190 mJ. The spectra broadening was also observed as discussed above.

We also studied the influence of the pressure on each harmonic as shown in Fig. 4.35. The 25^{th} HHG intensity first increases quadratically with the gas pressure, as expected for a fully coherent process up to an optimum value between 4 and 6 $\times 10^{-5}$ torr. And then, the 25^{th} HHG emission drops due to the absorption of the harmonic photons by the target argon gas, and the ionization-induced refraction of the driving laser. The optimum gas pressure for the 27^{th} HHG is ~ 7 $\times 10^{-5}$ torr since the phase-matching gas pressure varies as we discussed before.

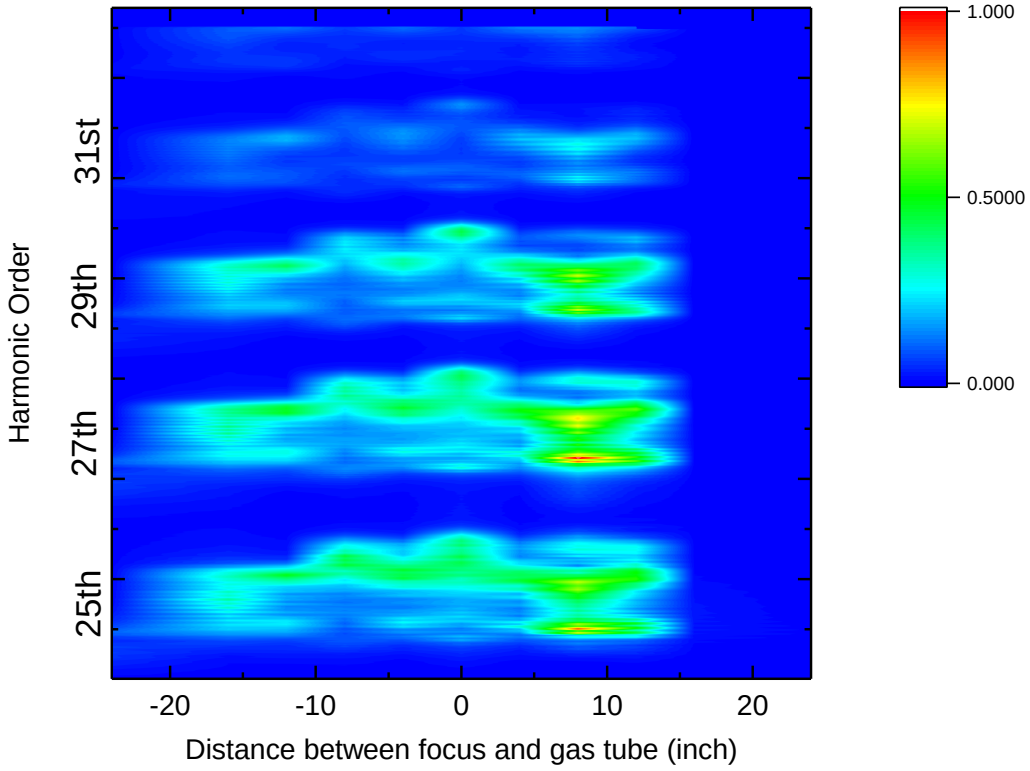

Figure 4.36 HHG intensities for different orders as a function of the distance between the focus and the gas tube. The focus position was controlled by varying the separation of the telescope. The pulse energy is ~ 110 mJ.

To investigate the relationship between the HHG output flux and the target gas position relative to the focusing point, we measured HHG intensity while varying the focus position by changing the separation of the telescope along the propagation axis of the driving laser. It is one of the most important issues in HHG optimization, as the interaction intensity in the gas dictates the propagation condition of the driving laser. The negative values of the abscissa correspond to focus positions in front of the gas target. At positive z values, the gas medium is placed before the focus. As presented in Fig. 4.36, the harmonic signal gradually increased toward the gas tube, and

the maximal HHG signal was obtained near z= 8 inch. At this positon, the laser spot diameter is about 1mm (Full width) with a pulse energy of 100 mJ.

With the gas medium after the focus, the diverging incident beam profile is degrading due to the plasma defocusing. The plasma defocusing effect severely limits the effective interaction length for harmonics generation. However, when the focus is after the gas medium, profile flattening and self-guiding can occur when a converging laser beam may compensate the plasma defocusing. When the argon target is ionized by the driving laser, the central part of the laser beam is refracted outwards due to higher electron density at the center, while the less-affected outer beam still converges. So, the laser beam is redistributed spatially and to form a flattened profile in the central portion. As a result, the electron density profile can also be flattened in the same region while the boundary electrons change rapidly. So, it can create a flattened refractive index profile with a sharp increase at boundaries, resulting a wave guide in which the laser beam is self-guided. The effective interaction volume can be significantly enhanced by the flattening and self-guiding intense laser pulse. Thus, it can increase the harmonic conversion efficiency [105]. As a result, the HHG flux is enhanced. Hence, great care should be taken to select a target gas location to ensure a sufficiently long interaction length.

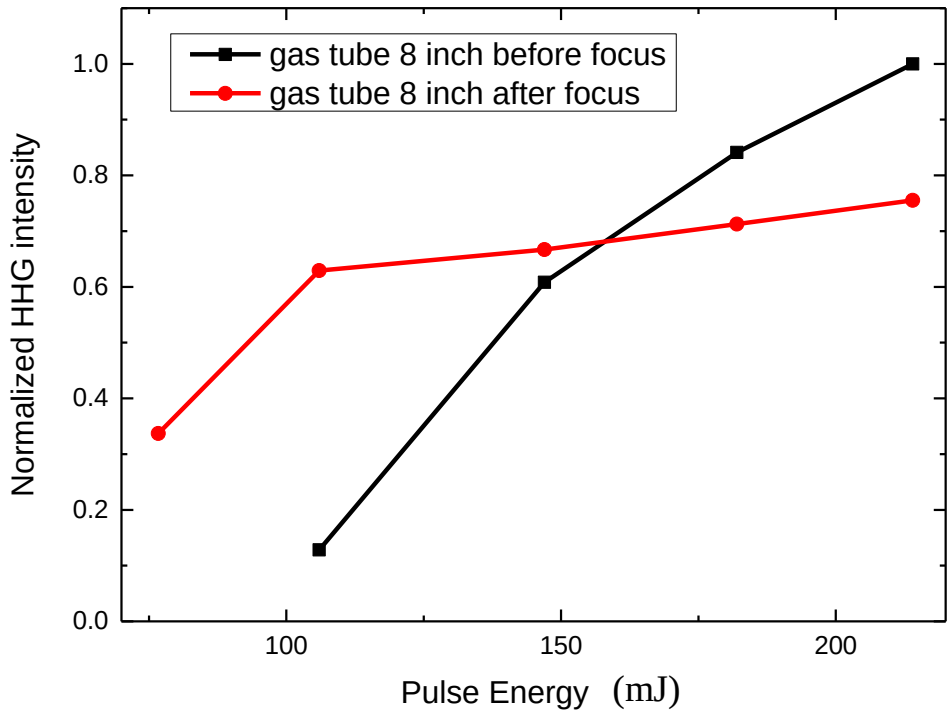

Figure 4.37 Total HHG counts recorded by a XUV CCD camera as a function of laser pulse energy for different focus positions: gas tube place 8 inch before (black line) and after focus (red line).

The above conclusion is consistent with the results in Fig. 4.37. With increase of the laser energy, the plasma defocusing emerges and can be exactly compensated by tailoring the convergence of the laser beam into the gas target. It effectively increases the phase-matching interaction volume, results in the increase of HHG intensities.

At last, the absolute total output energy of HHG was measured using an XUV photodiode (AXUV 100). This 15 mm by 16.5 mm size XUV photodiode is sensitive to XUV wavelengths from 250 to 10 nm with an internal quantum efficiency of 100%. The photodetector is a silicon p-n junction. Electron-hole pairs are created when XUV photons are incident on the chip. The

electron-hole pairs will be separated by the p-n junction electric field. So, the output current from this photodiode is proportional to the number of XUV photons. This photodiode was placed in the beam path with a 200 nm thick aluminum filter as shown in Fig. 4.18, and the output signal was recorded directly on an oscilloscope. The current is given by:

$$i = \frac{dQ}{dt} = \frac{V}{R} \tag{4-29}$$

where Q is the charge, R is the resistance and V is the voltage.

As a result, the total charge Q is expressed as:

$$Q = \frac{\int V(t)dt}{R} \tag{4-30}$$

where resistance is the input impedance of the scope and is ~50 Ω.

A typical oscilloscope signal is shown in Fig. 4.38. The black line is the signal when the XUV photons are being generated. The red line is the signal when the target gas is turned off with driving laser on. It is due to a very small transmission from the aluminum filter because of some very tiny pinholes in the filters.

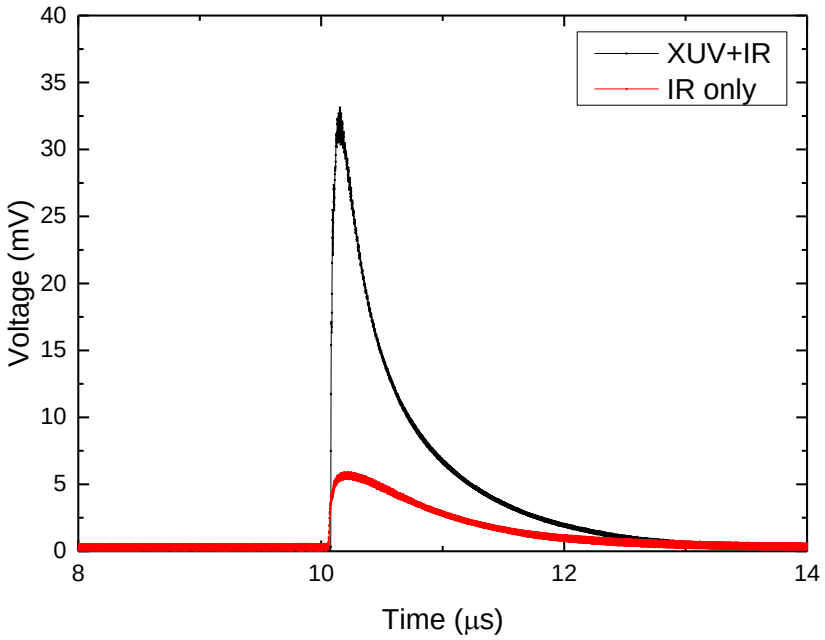

Figure 4.38 XUV photodiode signals for XUV and IR (black line) and IR only (red line).

The total number of photons originally generated can be calculated by:

$$N = \frac{Q}{e\eta T} \tag{4-31}$$

where e is the electron charge, η is the quantum efficiency of the detector, and T is the total transmission of the XUV reflectors and filters. The quantum efficiency is ~8 for our spectrum (~40 eV center energy). The transmission of the aluminum filters was independently measured by adding another aluminum filter to the detector. A total XUV pulse energy was measured with and without the additional filter and the ratio gave the transmission of our typical filter. A new aluminum filter has a transmission of 50% while ours transmits only ~20%. This is due to the

oxidized thin layers on both sides of the filter [106]. The total number of XUV photons was found to be 4×10^{10}. This gives a total pulse energy of 0.3 μJ at the exit of the gas tube.

CHAPTER 5 - EXPERIMENTS OF FEW-CYCLE CEP-SENSITIVE MIR FILAMENTS IN AIR

Nonlinear self-channeling of intense laser pulses in transparent media, commonly termed laser filamentation, has been extensively investigated using near-infrared (NIR) laser sources at 800 nm wavelength [107]. It has been recently argued that filamentation physics in the mid-infrared (MIR) spectral region can be profoundly different from that in the NIR. The generation of low-order harmonics may become the dominant effect that governs the nonlinear propagation. In addition, the optical period in the MIR is inherently longer than in the NIR [108]. The effects of the carrier-envelope phase (CEP) may become significant for relatively long pulse durations ~10 fs, which corresponds to about two optical cycles at 1.7 μm [109, 110].

5.1 The Concept of Carrier-Envelope Phase

The electric field of a laser pulse can be mathematically represented as:

$$E_0(t) = \cos(\omega_c t + \phi_{CE)} \tag{5-1}$$

where $E_0(t)$ is the electric field amplitude, ω_c is the carrier-frequency, and Φ_{CE} is the CEP. The CEP of the laser pulse depicts the offset between the peak of the laser electric field oscillation with respect to the laser pulse envelope at t=0. This is shown in Fig. 5.1. The peak of the carrier-wave oscillation is offset by Φ_{CE} to the peak of the pulse envelope.

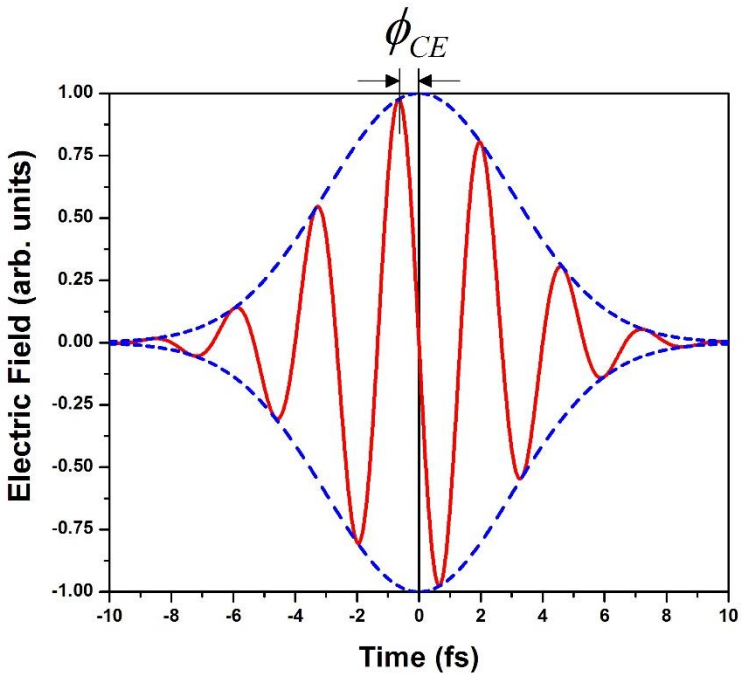

Figure 5.1 CEP for a laser pulse: Electric field (solid curve) and Pulse envelope (dashed curve).

To demonstrate more CEP values, four laser pulses with different CEP values change by π/2 are shown in Fig. 5.2. The electric fields seem to advance towards the leading edge of the pulses as the phase changes from 3π/2 to π/2 in steps.

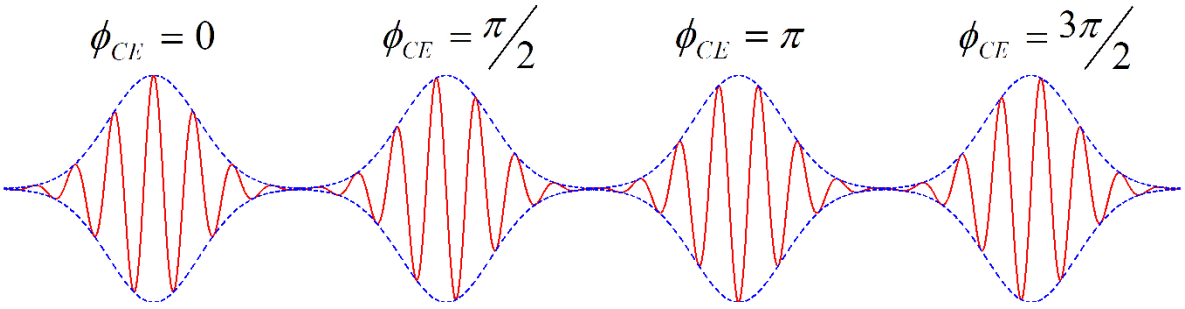

Figure 5.2 Four pulses with different CEP values.

The pulses used in Fig 5.2 for illustration of the CEP were few-cycles lasers to allow the CEP shift to be observed clearly. As the laser pulse duration rapidly approaches few or even single cycles, the electric field amplitude changes rapidly within a half cycle. This rapid variation of the electric field within the laser pulse envelope is the origin of CEP dependent effects in many phenomena such as above-threshold ionization (ATI), HHG and laser induced filaments [110-112]. The CEP control has permitted researchers access to controlling such phenomena susceptible to the CEP. The new development of a high-energy MIR few-cycle CEP-stable laser in our lab opens the study of CEP effects on the propagation dynamics of few-cycle MIR laser pulses in the filamentation regime for the first time.

5.2 A CE Phase-Stabilized Few-Cycle Laser at 1.7 μm

Different approaches to generate intense mid-infrared CEP stabilized few-cycle laser pulses have been demonstrated [113-115]. However, none of these approaches has been able to produce milli-joule sub-two cycle CEP stabilized laser pulses [116, 117]. In our lab, we generate a 3 mJ, sub-two cycle, CEP-stable laser pulse at 1.7 μm via a three-stage optical parametric chirped-pulse amplifier (OPCPA) in BiB_3O_6 (BIBO) [118]. To seed this laser, a pulse energy as high as 1 μJ is generated by intra-pulse different frequency generation (DFG).

DFG is one of the most important second order nonlinear effects. A pump photon with an angular frequency ω_p propagating in a nonlinear medium (like a BIBO), breaks down into two lower energy photons of frequencies ω_s and ω_i spontaneously or by stimulated parametric emission [119]. The suffixes p, s and i refer to pump, signal and idler pulses. The frequencies (signal and idler) are determined by the energy conservation condition:

$$\omega_s = \omega_p - \omega_i \tag{5-2}$$

Additionally, a momentum relationship (momentum conservation condition) must be satisfied during the parametric amplification process.

$$\Delta k = k_p - k_s - k_i \tag{5-3}$$

$$\left|k_j\right| = n_j(\omega)\frac{\omega_j}{c_0} = n_j(\omega)\frac{2\pi}{\lambda_j} \tag{5-4}$$

where k is the wave vector for laser pulses. The CEPs of the three pulses have a relation through the parametric interaction:

$$\Phi_i = \Phi_p - \Phi_s - \frac{\pi}{2} \tag{5-5}$$

If the two pulses undergoing the DFG process are from the same laser source and thus share the same CEP ($\Phi_p = \varphi + c3$, $\Phi_s = \varphi + c2$), then the CEP for the idler is given by:

$$\Phi_i = c3 - c2 - \frac{\pi}{2} = constant \tag{5-6}$$

So, the fluctuations of CEP are automatically cancelled in a passive and all-optical way [120, 121]. To generate mid-infrared pulses seeded by the DFG process, a wide spectrum input is a prerequisite. The DFG process occurs between different frequency components of a supercontinuum, which is sent into a crystal with ordinary polarization. The schematic setup of the OPCPA system is shown in Fig. 5.3.

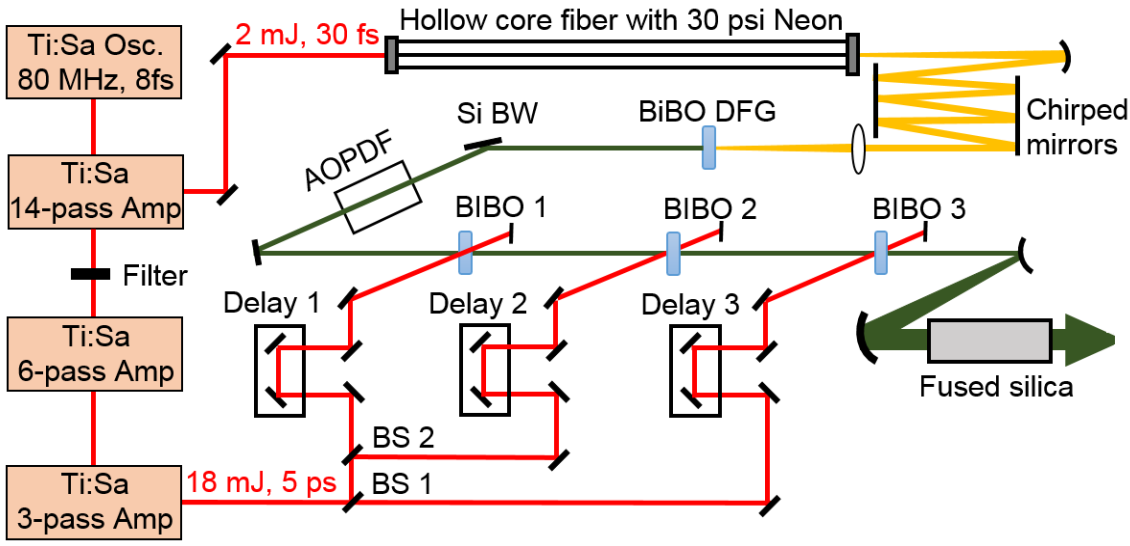

Figure 5.3 A diagram of our 1.7 μm OPCPA laser system. FS - Fused silica; BS1 - 20% reflection beam splitter; BS2 - 10% reflection beam splitter; Si BW - Silicon window at Brewster angle; AOPDF - Acousto-optic programmable dispersive filter for pulse stretching. (adapted with permission from ref [118], [Opt. Lett.]).

The OPCPA system starts with a homebuilt three-stage multi-pass Ti:-Sapphire laser system with a repetition rate of 1 kHz. The nJ pump (730 nm-830 nm) is stretched to 300 ps and boosted to 3.6 mJ in a 14-pass amplifier, out of which 2.6 mJ is compressed to 2.2mJ, 30 fs by a pair of transmission gratings and is then focused to a hollow core fiber with 30 psi neon for while light generation. This supercontinuum is then compressed to ~7 fs by using several pairs of chirped mirrors. A broadband IR (1.2 μm -2.2 μm) seed with a pulse energy of ~1 μJ is produced by intra-pulse DFG of the supercontinuum in a 1 mm type-II BIBO crystal (cutting angle 60 degree). This IR seed is stretched to ~4.4 ps using an IR acousto-optic programmable dispersive filter (AOPDF) with a typical energy of 20 nJ. The bandwidth of the residual 1 mJ pump from the 14-pass amplifier is chopped to 760 nm- 810 nm with a flat-top shape beam profile by a transmission filter. The pulse energy of 21 mJ is achieved after two consecutive 6-pass and 3-pass amplifiers, which is

compressed to 18 mJ, 5 ps (FWHM) in a transmission grating pair. The OPCPA consists of three stages, in which all BIBO crystals are type I cutting at 11 degrees and a small non-collinear angle of 1 degree is introduced to separate the signal and pump after amplification. Both the first and second stages have 5 mm thick BIBO crystals, and are pumped by a 360 μJ and 3.3 mJ pump laser, respectively. The third stage 3 mm BIBO is pumped by a 14.4 mJ pump laser and boosts the pulse energy to 3 mJ. We achieved a highest conversion efficiency (18%) in the last stage among any current sub-two-cycle OPCPA. The IR pulse is compressed by a 15 cm fused silica to a pulse duration of 11.4 fs (FWHM) retrieved by a home-made second harmonic generation (SHG) FROG, as shown in Fig. 5.4 [118].

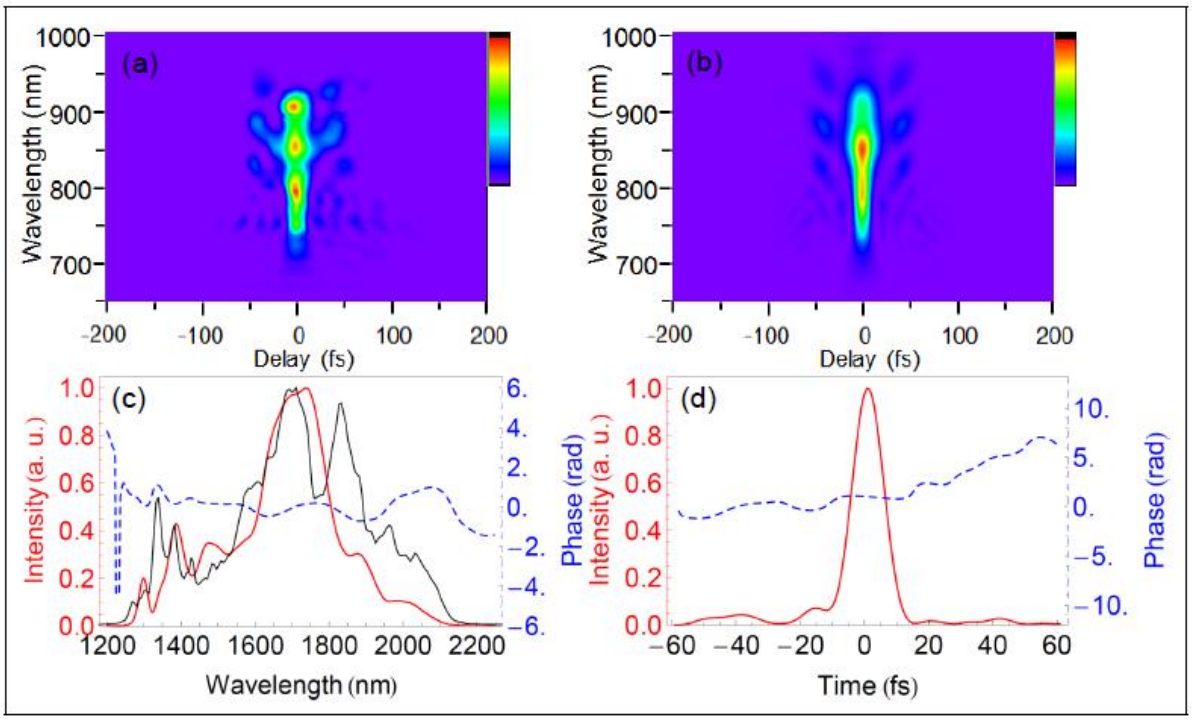

Figure 5.4 (a) Experimental FROG trace; (b) retrieved FROG trace; (c) independently measured spectrum (black), retrieved spectrum (red), and retrieved spectral phase (blue); (d) retrieved pulse (red) and temporal phase (blue). (adapted with permission from ref [118], [Opt. Lett.])

We build a single-shot f-2f interferometer to measure CEP values. A sapphire plate is applied to generate a white light continuum and a BBO is used to double the frequency. The CEP fluctuation is measured to be ~165 mrad (RMS) after one hour of single-shot collection, as depicted in Fig. 5.5.

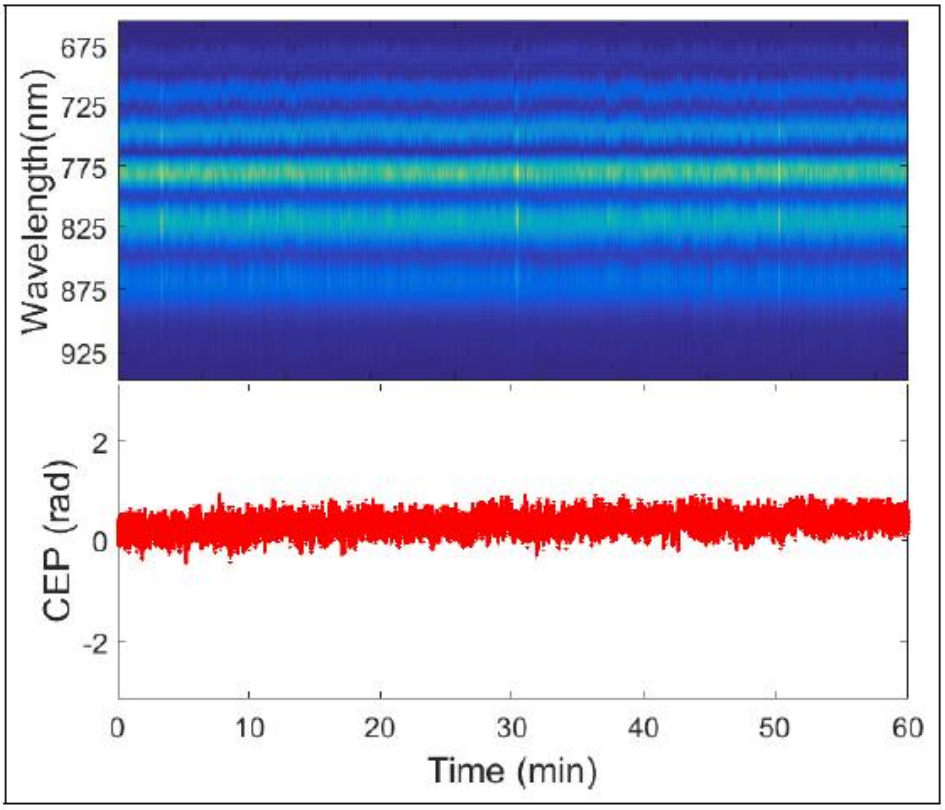

Figure 5.5 Top: f-2f interferograms collected for 1 hour; bottom: CEP fluctuations (165 mrad RMS) in one hour. (adapted with permission from ref [118], [Opt. Lett.])

5.3 Filamentation Induced by the 1.7 μm CEP Stabilized Laser in Air

The definition of a laser induced filamentation can be described in Fig. 5.6. An intense high power pulse was focused to reach high enough intensities to ionize the medium in its path and leave behind a narrow column of plasma. Filamentation begins with self-focusing within a nonlinear medium due to an intensity dependent and spatially varying refractive index. The nonlinear refractive index associated with a medium and modulated by an intense laser pulse is given by:

$$n = n_0 + n_2 I(r,t) \tag{5-7}$$

where n is the total refractive index, n_0 is the field free refractive index, n_2 is the nonlinear refractive index and I (r, t) is the temporally and spatially varying laser intensity [119].

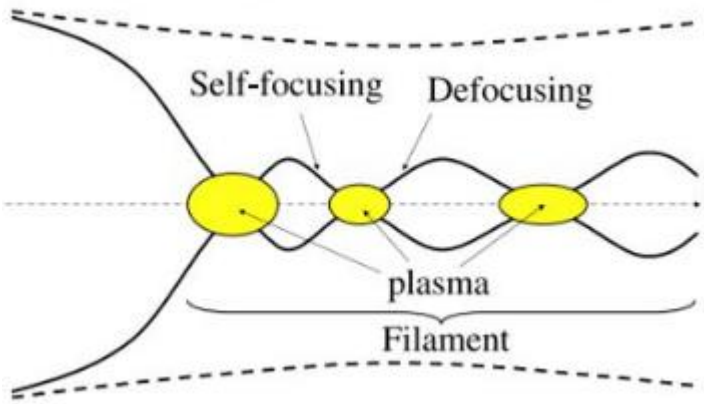

Figure 5.6 Self-focusing and filamentation of a femtosecond laser pulse.

A laser pulse with a Gaussian intensity distribution will shape a Gaussian refractive index profile, resulting in a highest refractive index along the propagation axis. This modulated refractive index acts as a positive lens that makes the beam to self-focus, which causes the beam to collapse.

Self-focusing increases the intensity until ionization of the gas medium occurs and a plasma is formed. Then, a higher electron density at the center will refract the laser beam outwards. The laser beam is redistributed spatially and this will cancel the effects of self-focusing and contribute to the formation of a filament. These self-focusing and defocusing process will modulate and stabilize the filament. These filaments are of great interest due to applications to remote sensing, super-continuum generation, pulse compression, and THz generation [122].

The critical power of self-focusing is given by:

$$P_{cr} = C(8\pi n_0 n_2)^{-1}\lambda^2 \tag{5-8}$$

where C is a numerical factor, 3.72<C<6.4, defined by the beam profile and λ is the laser wavelength [123, 124]. The critical power threshold is a key parameter and it sets a limit on the peak power and the energy of laser pulses in a filamentamtion. Besides, it is quadraticlly dependent on the wavelength of the driving laser. This λ^2 scaling law will enable us to increase the laser peak power and radiation energy in a single filament by a longer wavelength driving laser. On the other hand, the physics behind the influence of the initial CEP on the filamentation of ultrashort laser pulses in air is not entirely clear. Thanks to our 1.7 μm CEP stabilized few-cycle laser, we can experimentally investigate the CEP effects in filamentation in air.

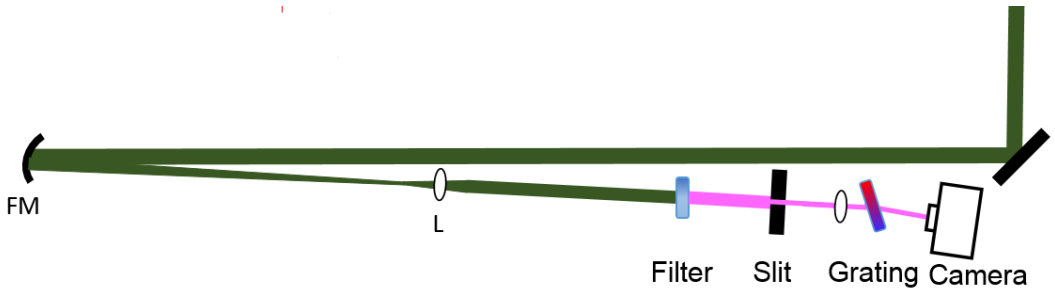

Figure 5.7 Generation of a laser filament in air using a 1.7 μm laser pulse: FM - gold coated focusing mirror (f ~2 m); L - collimated lens (f ~500 mm).

The laser beam (1.4 mJ 1.7 μm 11.4 fs) is focused using a spherical mirror with a focal length of 2 m. After the focus, a lens (f ~500 mm) was used to collimate the beam and a filter is applied to eliminate the mid infrared laser and to transmit the radiation from the filament. Then the beam was directly sent into the slit of an imaging spectrometer as shown in Fig. 5.7. The filament has been characterized in terms of plasma distribution and spectral reshaping of the laser pulse upon passing through the filamentation zone. The generated spectrum does not show any measurable dependence on the pulse repetition frequency of the laser, indicating that the effects of thermal accumulation in the air are negligible [125]. The phase of the laser was adjustable by controlling an acousto-optic programmable dispersive filter as shown in Fig. 5.3. A roughly 15 cm long filament was observed. Two beam images with an initial CEP of $0.2\,\pi$ and $0.9\,\pi$, respectively, impinged on a screen were recorded by a CCD camera. The different colors indicate the fact that the spectrum of the generated broadband emission depends on the CEP quite strongly.

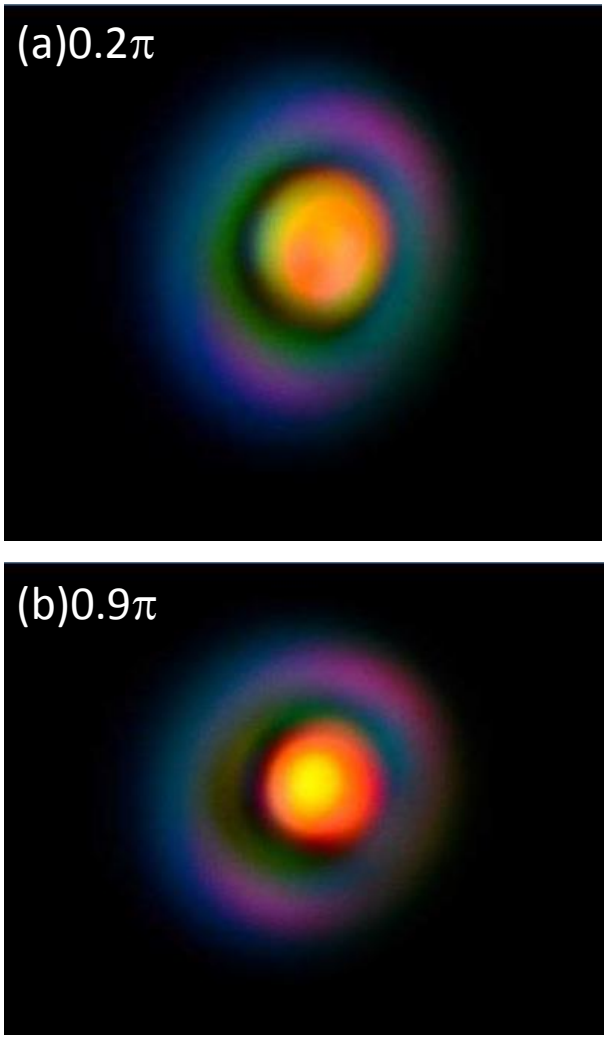

Figure 5.8 Direct emission patterns with two values of the CEP: (a) 0.2 π and (b) 0.9 π.

We measured the broadened spectra due to the self-phase modulation as shown in Fig. 5.9. Subtle and repeatable differences in the spectra for CEP=0.2 π and 0.9 π were observed around 550nm and 900n m.

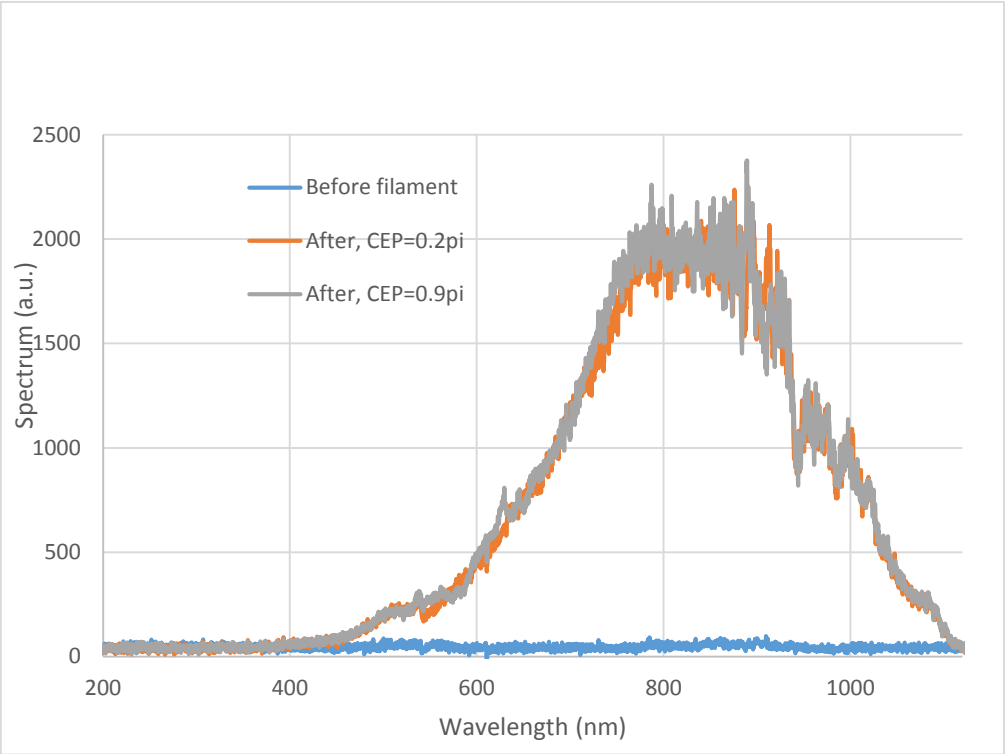

Figure 5.9 Cross-section-integrated NIR-VIS spectra in forward direction: before filament (blue line), after filament with CEP=0.2 π (orange line) and with CEP= 0.9 π (gray line).

The CEP dependence is π-periodic, as expected. It becomes particularly evident when the emission is analyzed with the aid of an imaging spectrometer, which resolves the wavelength and the direction of emission along two orthogonal axes, producing the so-called k-ω spectrum. Examples of the two most dissimilar k-ω spectra corresponding to two different values of the CEP (with an arbitrary constant phase offset) are shown Fig. 5.10.

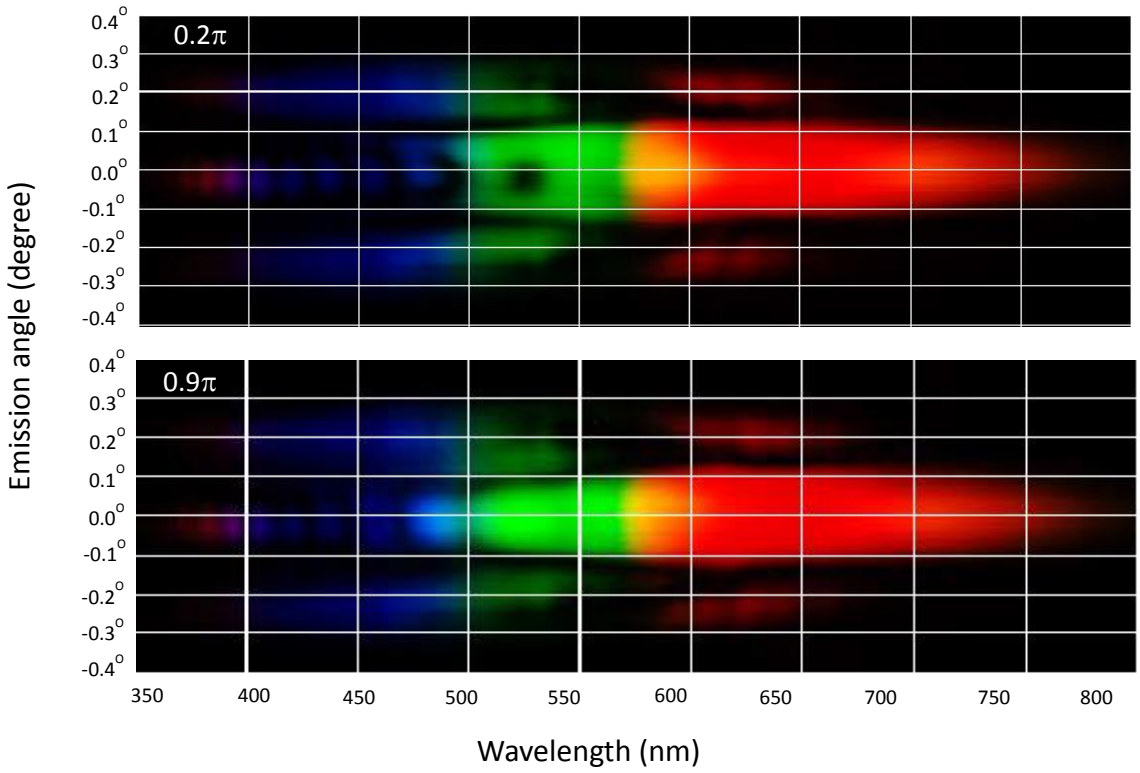

Figure 5.10 Angularly-resolved spectra of forward- propagating white-light emission, for the two values of the CEP that produce the most dissimilar spectra. Emission with wavelengths above 750 nm is blocked by a color-glass filter.

The most evident CEP-dependent feature is the spectral hole in the on-axis emission at ~525 nm wavelength, which is close to the third harmonic of the pump. The hole opens and closes as the value of the CEP is changed. Currently, the physics behind the observed CEP dependence of the third harmonic emission is not fully understood. Our current hypothesis is that the spectral hole is due to the interference between two channels of 3rd harmonic generation: the direct process, converting three photons of the pump beam into one photon of third harmonic, and the sum-frequency mixing between the pump and its second harmonic. The generation of the latter, which is prohibited in an isotropic medium, is enabled through the inversion symmetry breaking, e.g., by

the plasma density gradient in the filament [126]. Note that we do experimentally observe strong second-harmonic emission. This is the first experimental demonstration of CEP-controlled filamentation in air using mJ-level few-cycle mid-infrared laser pulses. The results show, remarkably, that the phase survives in the highly nonlinear filament propagation through air.

CHAPTER 6 - OUTLOOK AND CONCLUSIONS

Previous attosecond pump-probe type measurements can only be achieved by combining a few-cycle visible or near infrared pulse with an attosecond pulse. The ultimate time limit is directly affected by the duration of the few cycle visible or near infrared pulse. In this work, a robust and efficient method for generating high flux attosecond pulses was developed and tested by a loosely focused geometry. The iFAST high power driving laser and HHG facilities have been built for the generation, characterization and application of microjoule level attosecond pulses at 50 eV photon energy. The designed end-station has the capability of focusing attosecond pulses to spot sizes of 1 μm, and it is sufficient to achieve the desired 1-10 mJ/cm^2 XUV energy density to induce the nonlinear experiments with 1 μJ pulse energies. A true pump-probe experiment will be conducted due to the establishment of true attosecond-attosecond measurements in this work.

In the near future, with the availability of attosecond pulses with sufficient flux, it will be possible to use one pulse to initiate a process, such as to create electron holes in an inner shell, and to probe the time dynamics of the electron-correlated processes with the second attosecond pulse, either in transient absorption or by photoelectron spectroscopy. Attosecond processes in materials will then be probed by methods such as x-ray transient absorption spectroscopy and transient dispersion. It can provide direct access to atom-specific charge state dynamics, indicative of the motion of electrons or holes in materials. The methods will provide sophisticated means to follow charge flow in materials, to trace the location of holes and electrons by way of their influence on the core level spectrum of specific atoms in the materials. Exciting prospects emerge to follow spin and magnetism, through electronic and spin superposition states and their coupling to phonon modes. This will introduce the "era" of true attosecond-attosecond pump-probe spectroscopy.

APPENDIX A: LIST OF PUBLICATIONS

Peer-Reviewed Journal Publications

1. Yang Wang, Tianyi Guo, Jialin Li, Xiaoming Ren, Yanchun Yin, Jie Li, Yi Wu, Eric Cunningham, M. F. Jager, C. J. Kaplan, D. M. Neumark, S. R. Leone, and Zenghu Chang, "Enhanced high-order harmonic generation driven by a wave-front corrected high-intensity laser" (under submission)

2. Yang Wang, Jialin Li, Tianyi Guo, Xiaoming Ren, Yanchun Yin, Jie Li, Yi Wu, and Zenghu Chang, "Generation of an intense attosecond pulse and its application" (under submission)

3. Yanchun Yin, Xiaoming Ren, Andrew Chew, Jie Li, Yang Wang, Fengjiang Zhuang, Yi Wu & Zenghu Chang, "Generation of octave-spanning mid-infrared pulses from cascaded second-order nonlinear processes in a single crystal", Scientific Reports 7, 11097 (2017)

4. Jie Li, Xiaoming Ren, Yanchun Yin, Kun Zhao, Andrew Chew, Yan Cheng, Eric Cunningham, Yang Wang, Shuyuan Hu, Yi Wu, Michael Chini & Zenghu Chang, "53-attosecond X-ray pulses reach the carbon K-edge", Nature Communications 8, 186 (2017)

5. Yanchun Yin, Andrew Chew, Xiaoming Ren, Jie Li, Yang Wang, Yi Wu & Zenghu Chang, "Towards Terawatt Sub-Cycle Long- Wave Infrared Pulses via Chirped Optical Parametric Amplification and Indirect Pulse Shaping", Scientific Reports 8, 45794 (2017)

6. Yanchun Yin, Jie Li, Xiaoming Ren, Yang Wang, Andrew Chew, and Zenghu Chang, "High-energy two-cycle pulses at 3.2 μm by a broadband-pumped dual-chirped optical parametric amplification", Optics Express 24(22), 24989 (2016)

7. Yi Wu, Eric Cunningham, Jie Li, Huaping Zang, Michael Chini, Xiaowei Wang, Yang Wang, Kun Zhao, and Zenghu Chang, "Generation of High-Flux Attosecond Extreme Ultraviolet Continuum with a 10 Terawatt Laser", Applied Physics Letters 102,201105 (2013)

Conference Presentation

Yang Wang, Xiaoming Ren, Yanchun Yin, Jie Li, Pavel Polynkin, Aaron C. Bernstein, James R. Welch, Michael C. Downerand and Zenghu Chang, "Experiments of Few-Cycle CEP-sensitive MIR Filaments in Air", Annual MURI Review for Laser induced Filaments, 3rd-4th May, 2017, Orlando, FL (Oral Presentation and Poster).

APPENDIX B: COPYRIGHT PERMISSION

NATURE PUBLISHING GROUP LICENSE TERMS AND CONDITIONS

Oct 02, 2017

This Agreement between UCF Department of Physics -- YANG WANG ("You") and Nature Publishing Group ("Nature Publishing Group") consists of your license details and the terms and conditions provided by Nature Publishing Group and Copyright Clearance Center.

License Number	4201051486787
License date	Oct 02, 2017
Licensed Content Publisher	Nature Publishing Group
Licensed Content Publication	Nature Physics
Licensed Content Title	Attosecond science
Licensed Content Author	P. B. CorkumandFerenc Krausz
Licensed Content Date	Jun 1, 2007
Licensed Content Volume	3
Licensed Content Issue	6
Type of Use	reuse in a dissertation / thesis
Requestor type	academic/educational
Format	electronic
Portion	figures/tables/illustrations
Number of figures/tables/illustrations	1
High-res required	no
Figures	Figure 2 Creating an attosecond pulse. a–d, An intense femtosecond near-infrared or visible (henceforth: optical) pulse (shown in yellow) extracts an electron wavepacket from an atom or molecule.
Author of this NPG article	no
Your reference number	14
Title of your thesis / dissertation	GENERATION OF HIGH-FLUX ATTOSECOND PULSES AND TOWARDS ATTOSECOND-ATTOSECOND PUMP-PROBE EXPERIMENTS
Expected completion date	Nov 2017
Estimated size (number of pages)	150
Requestor Location	UCF Department of Physics 4111 Libra Drive Physical Sciences Bldg. 430 ORLANDO, FL 32816 United States Attn: YANG WANG
Billing Type	Invoice
Billing Address	UCF Department of Physics 4111 Libra Drive

Physical Sciences Bldg. 430

ORLANDO, FL 32816
United States
Attn: YANG WANG

Total 0.00 USD

Terms and Conditions

Terms and Conditions for Permissions

Nature Publishing Group hereby grants you a non-exclusive license to reproduce this material for this purpose, and for no other use,subject to the conditions below:

1. NPG warrants that it has, to the best of its knowledge, the rights to license reuse of this material. However, you should ensure that the material you are requesting is original to Nature Publishing Group and does not carry the copyright of another entity (as credited in the published version). If the credit line on any part of the material you have requested indicates that it was reprinted or adapted by NPG with permission from another source, then you should also seek permission from that source to reuse the material.

2. Permission granted free of charge for material in print is also usually granted for any electronic version of that work, provided that the material is incidental to the work as a whole and that the electronic version is essentially equivalent to, or substitutes for, the print version.Where print permission has been granted for a fee, separate permission must be obtained for any additional, electronic re-use (unless, as in the case of a full paper, this has already been accounted for during your initial request in the calculation of a print run).NB: In all cases, web-based use of full-text articles must be authorized separately through the 'Use on a Web Site' option when requesting permission.

3. Permission granted for a first edition does not apply to second and subsequent editions and for editions in other languages (except for signatories to the STM Permissions Guidelines, or where the first edition permission was granted for free).

4. Nature Publishing Group's permission must be acknowledged next to the figure, table or abstract in print. In electronic form, this acknowledgement must be visible at the same time as the figure/table/abstract, and must be hyperlinked to the journal's homepage.

5. The credit line should read:
   Reprinted by permission from Macmillan Publishers Ltd: [JOURNAL NAME] (reference citation), copyright (year of publication)
   For AOP papers, the credit line should read:
   Reprinted by permission from Macmillan Publishers Ltd: [JOURNAL NAME], advance online publication, day month year (doi: 10.1038/sj.[JOURNAL ACRONYM].XXXXX)

   Note: For republication from the *British Journal of Cancer*, the following credit lines apply.
   Reprinted by permission from Macmillan Publishers Ltd on behalf of Cancer Research UK: [JOURNAL NAME] (reference citation), copyright (year of publication)For AOP papers, the credit line should read:
   Reprinted by permission from Macmillan Publishers Ltd on behalf of Cancer Research UK: [JOURNAL NAME], advance online publication, day month year (doi: 10.1038/sj.[JOURNAL ACRONYM].XXXXX)

6. Adaptations of single figures do not require NPG approval. However, the adaptation should be credited as follows:

   Adapted by permission from Macmillan Publishers Ltd: [JOURNAL NAME] (reference citation), copyright (year of publication)

   Note: For adaptation from the *British Journal of Cancer*, the following credit line

applies.
Adapted by permission from Macmillan Publishers Ltd on behalf of Cancer Research UK: [JOURNAL NAME] (reference citation), copyright (year of publication)

7. Translations of 401 words up to a whole article require NPG approval. Please visit http://www.macmillanmedicalcommunications.com for more information.Translations of up to a 400 words do not require NPG approval. The translation should be credited as follows:

   Translated by permission from Macmillan Publishers Ltd: [JOURNAL NAME] (reference citation), copyright (year of publication).

   Note: For translation from the *British Journal of Cancer*, the following credit line applies.
   Translated by permission from Macmillan Publishers Ltd on behalf of Cancer Research UK: [JOURNAL NAME] (reference citation), copyright (year of publication)

We are certain that all parties will benefit from this agreement and wish you the best in the use of this material. Thank you.
Special Terms:
v1.1

Questions? customercare@copyright.com or +1-855-239-3415 (toll free in the US) or +1-978-646-2777.

From: wangyang [mailto:wangyang@knights.ucf.edu]
Sent: Monday, October 02, 2017 8:06 PM
To: pubscopyright
Cc: Yanchun Yin
Subject: a copyright permission request from Yang Wang (University of Central Florida)

Dear Editor:
This is Yang Wang from College of Optics and Phonics at the University of Central Florida.
There is one paper from our group published in 2016 and the information is:

"High-efficiency optical parametric chirped-pulse amplifier in BiB3O6 for generation of 3 mJ, two-cycle, carrier-envelope-phase-stable pulses at 1.7 μm"
Y.C. Yin, J. Li, X.M. Ren, K. Zhao, Y. Wu, E. Cunningham, and Z. Chang
Optics Letters 41(6), pp.1142-1145

I used this laser to do the filament experiment and I am going to involve the laser information to my Phd dissertation thesis.
Can I ask for a permission to use the following three figures in this paper to demonstrate the laser parameters in my thesis?

"Fig. 3. Schematic setup of the OPCPA system. BS1, 20% reflection beam splitter; BS2, 10% reflection beam splitter; Si BW, silicon window at
Brewster's angle.

Fig. 5. (a) Experimental SHG FROG trace; (b) retrieved SHG
FROG trace; (c) independently measured spectrum (black), retrieved
spectrum (red), and retrieved spectral phase (green); (d) retrieved pulse
(red) and temporal phase (green).

Fig. 6. Top: f-to-2f interferograms collected for 1 h; bottom: CEP
fluctuations (165 mrad RMS) in 1 h."

My contact information:
Name: Yang Wang
4111 Libra Drive
Physical Sciences Bldg. 430
Orlando, FL 32816-2385
Tel: 785-341-3277

I also cc this email to the first author of this paper who is Dr. Yanchun Yin in our group.

Thank you.

Regards
YANG Wang

To: pubscopyright <copyright@osa.org>;

Cc: Yanchun Yin <Yanchun.Yin@ucf.edu>;

Hello, Rebecca
I will follow the citation format.
Thanks
Regards
YANG

From: pubscopyright <copyright@osa.org>
Sent: Tuesday, October 3, 2017 1:54:30 PM
To: wangyang; pubscopyright
Cc: Yanchun Yin
Subject: RE: a copyright permission request from Yang Wang (University of Central Florida)

Dear Yang Wang,

For the use of figures 3, 5, and 6 from Yanchun Yin, Jie Li, Xiaoming Ren, Kun Zhao, Yi Wu, Eric Cunningham, and Zenghu Chang, "High-efficiency optical parametric chirped-pulse amplifier in BiB3O6 for generation of 3 mJ, two-cycle, carrier-envelope-phase-stable pulses at 1.7 μm," Opt. Lett. 41, 1142-1145 (2016):

OSA considers your requested use of its copyrighted material to be Fair Use under United States Copyright Law. It is requested that a complete citation of the original material be included in any publication.

While your publisher should be able to provide additional guidance, OSA prefers the below citation formats:

For citations in figure captions:

[Reprinted/Adapted] with permission from ref [x], [Publisher]. (with full citation in reference list)

For images without captions:

Journal Vol. #, first page (year published)
An example: Opt. Lett. 41, 1142 (2016)

Let me know if you have any questions.

Kind Regards,

Rebecca Robinson

Rebecca Robinson
October 3, 2017
Authorized Agent, The Optical Society

LIST OF REFERENCES

1. Corkum, P.B. and F. Krausz, *Attosecond science.* Nature physics, 2007. **3**(6): p. 381.
2. Krausz, F. and M. Ivanov, *Attosecond physics.* Reviews of Modern Physics, 2009. **81**(1): p. 163.
3. Chang, Z. and P. Corkum, *Attosecond photon sources: the first decade and beyond.* JOSA B, 2010. **27**(11): p. B9-B17.
4. Frank, F., C. Arrell, T. Witting, W. Okell, J. McKenna, J. Robinson, C. Haworth, D. Austin, H. Teng, and I. Walmsley, *Invited review article: technology for attosecond science.* Review of Scientific Instruments, 2012. **83**(7): p. 52.
5. Gagnon, E., P. Ranitovic, X.-M. Tong, C.L. Cocke, M.M. Murnane, H.C. Kapteyn, and A.S. Sandhu, *Soft X-ray-driven femtosecond molecular dynamics.* Science, 2007. **317**(5843): p. 1374-1378.
6. Nisoli, M. and G. Sansone, *New frontiers in attosecond science.* Progress in Quantum Electronics, 2009. **33**(1): p. 17-59.
7. Paul, P.M., E. Toma, P. Breger, G. Mullot, F. Augé, P. Balcou, H. Muller, and P. Agostini, *Observation of a train of attosecond pulses from high harmonic generation.* Science, 2001. **292**(5522): p. 1689-1692.
8. Ferray, M., A. L'Huillier, X. Li, L. Lompre, G. Mainfray, and C. Manus, *Multiple-harmonic conversion of 1064 nm radiation in rare gases.* Journal of Physics B: Atomic, Molecular and Optical Physics, 1988. **21**(3): p. L31.

9. Sansone, G., L. Poletto, and M. Nisoli, *High-energy attosecond light sources.* Nature Photonics, 2011. **5**(11): p. 655-663.

10. Bucksbaum, P.H., *The future of attosecond spectroscopy.* Science, 2007. **317**(5839): p. 766-769.

11. Hentschel, M., R. Kienberger, C. Spielmann, and G.A. Reider, *Attosecond metrology.* Nature, 2001. **414**(6863): p. 509.

12. Midorikawa, K., Y. Nabekawa, and A. Suda, *XUV multiphoton processes with intense high-order harmonics.* Progress in Quantum Electronics, 2008. **32**(2): p. 43-88.

13. Corkum, P.B., *Plasma perspective on strong field multiphoton ionization.* Physical Review Letters, 1993. **71**(13): p. 1994.

14. Keldysh, L., *Ionization in the field of a strong electromagnetic wave.* Sov. Phys. JETP, 1965. **20**(5): p. 1307-1314.

15. Bransden, B.H. and C.J. Joachain, *Physics of atoms and molecules*. 2003: Pearson Education India.

16. Protopapas, M., C.H. Keitel, and P.L. Knight, *Atomic physics with super-high intensity lasers.* Reports on Progress in Physics, 1997. **60**(4): p. 389.

17. Colosimo, P., G. Doumy, C. Blaga, J. Wheeler, C. Hauri, F. Catoire, J. Tate, R. Chirla, A. March, and G. Paulus, *Scaling strong-field interactions towards the classical limit.* Nature Physics, 2008. **4**(5): p. 386.

18. Hecht, J., *PHOTONIC FRONTIERS: HIGH HARMONIC GENERATION: High harmonic generation pushes spectroscopy to the cutting edge.* Laser Focus World, 2012. **48**(2): p. 44-47.

19. Itatani, J., J. Levesque, D. Zeidler, and H. Niikura, *Tomographic imaging of molecular orbitals.* Nature, 2004. **432**(7019): p. 867.

20. Ko, D.H., K.T. Kim, and C.H. Nam, *Attosecond-chirp compensation with material dispersion to produce near transform-limited attosecond pulses.* Journal of Physics B: Atomic, Molecular and Optical Physics, 2012. **45**(7): p. 074015.

21. Henke, B.L., E.M. Gullikson, and J.C. Davis, *X-ray interactions: photoabsorption, scattering, transmission, and reflection at E= 50-30,000 eV, Z= 1-92.* Atomic data and nuclear data tables, 1993. **54**(2): p. 181-342.

22. Ammosov, M., N.B. Delone, and V.P. Krainov, *Tunnelling ionization of complex atoms and of atomic ions in an alternating electromagnetic field.* Journal of Experimental and Theoretical Physics, 1986. **64**(6): p. 1191-1194.

23. Gibbon, P., *Harmonic generation by femtosecond laser-solid interaction: A coherent "water-window" light source?* Physical Review Letters, 1996. **76**(1): p. 50.

24. Ackermann, W.a., G. Asova, V. Ayvazyan, A. Azima, N. Baboi, J. Bähr, V. Balandin, B. Beutner, A. Brandt, and A. Bolzmann, *Operation of a free-electron laser from the extreme ultraviolet to the water window.* Nature photonics, 2007. **1**(6): p. 336-342.

25. Rocca, J.J., *Table-top soft x-ray lasers.* Review of Scientific Instruments, 1999. **70**(10): p. 3799-3827.

26. Takahashi, E., Y. Nabekawa, T. Otsuka, M. Obara, and K. Midorikawa, *Generation of highly coherent submicrojoule soft x rays by high-order harmonics.* Physical Review A, 2002. **66**(2): p. 021802.

27. Gallmann, L., C. Cirelli, and U. Keller, *Attosecond science: recent highlights and future trends.* Annual review of physical chemistry, 2012. **63**: p. 447-469.

28. Chang, Z., P.B. Corkum, and S.R. Leone, *Attosecond optics and technology: progress to date and future prospects.* JOSA B, 2016. **33**(6): p. 1081-1097.

29. Yakovlev, V.S., J. Gagnon, N. Karpowicz, and F. Krausz, *Attosecond streaking enables the measurement of quantum phase.* Physical review letters, 2010. **105**(7): p. 073001.

30. Nabekawa, Y., H. Hasegawa, E.J. Takahashi, and K. Midorikawa, *Production of doubly charged helium ions by two-photon absorption of an intense sub-10-fs soft x-ray pulse at 42 eV photon energy.* Physical review letters, 2005. **94**(4): p. 043001.

31. Manschwetus, B., L. Rading, F. Campi, S. Maclot, H. Coudert-Alteirac, J. Lahl, H. Wikmark, P. Rudawski, C. Heyl, and B. Farkas, *Two-photon double ionization of neon using an intense attosecond pulse train.* Physical Review A, 2016. **93**(6): p. 061402.

32. Hu, S. and L. Collins, *Attosecond pump probe: exploring ultrafast electron motion inside an atom.* Physical review letters, 2006. **96**(7): p. 073004.

33. Goulielmakis, E., M. Schultze, M. Hofstetter, V.S. Yakovlev, J. Gagnon, M. Uiberacker, A.L. Aquila, E. Gullikson, D.T. Attwood, and R. Kienberger, *Single-cycle nonlinear optics.* Science, 2008. **320**(5883): p. 1614-1617.

34. Shan, B., S. Ghimire, and Z. Chang, *Effect of orbital symmetry on high-order harmonic generation from molecules.* Physical Review A, 2004. **69**(2): p. 021404.

35. Antoine, P., A. L'huillier, and M. Lewenstein, *Attosecond pulse trains using high–order harmonics.* Physical Review Letters, 1996. **77**(7): p. 1234.

36. Chang, Z., *Single attosecond pulse and xuv supercontinuum in the high-order harmonic plateau.* Physical Review A, 2004. **70**(4): p. 043802.

37. Shan, B., S. Ghimire, and Z. Chang, *Generation of the attosecond extreme ultraviolet supercontinuum by a polarization gating.* Journal of modern optics, 2005. **52**(2-3): p. 277-283.

38. Corkum, P., N. Burnett, and M.Y. Ivanov, *Subfemtosecond pulses.* Optics letters, 1994. **19**(22): p. 1870-1872.

39. Platonenko, V. and V. Strelkov, *Single attosecond soft-x-ray pulse generated with a limited laser beam.* JOSA B, 1999. **16**(3): p. 435-440.

40. Tcherbakoff, O., E. Mével, D. Descamps, J. Plumridge, and E. Constant, *Time-gated high-order harmonic generation.* Physical Review A, 2003. **68**(4): p. 043804.

41. Sansone, G., E. Benedetti, F. Calegari, C. Vozzi, L. Avaldi, R. Flammini, L. Poletto, P. Villoresi, C. Altucci, and R. Velotta, *Isolated single-cycle attosecond pulses.* Science, 2006. **314**(5798): p. 443-446.

42. Li, X., A. L'Huillier, M. Ferray, L. Lompré, and G. Mainfray, *Multiple-harmonic generation in rare gases at high laser intensity.* Physical Review A, 1989. **39**(11): p. 5751.

43. Eichmann, H., A. Egbert, S. Nolte, C. Momma, B. Wellegehausen, W. Becker, S. Long, and J. McIver, *Polarization-dependent high-order two-color mixing.* Physical Review A, 1995. **51**(5): p. R3414.

44. Watanabe, S., K. Kondo, Y. Nabekawa, A. Sagisaka, and Y. Kobayashi, *Two-color phase control in tunneling ionization and harmonic generation by a strong laser field and its third harmonic.* Physical review letters, 1994. **73**(20): p. 2692.

45. Kim, I.J., C.M. Kim, H.T. Kim, G.H. Lee, Y.S. Lee, J.Y. Park, D.J. Cho, and C.H. Nam, *Highly efficient high-harmonic generation in an orthogonally polarized two-color laser field.* Physical Review Letters, 2005. **94**(24): p. 243901.

46. Pfeifer, T., L. Gallmann, M.J. Abel, P.M. Nagel, D.M. Neumark, and S.R. Leone, *Heterodyne mixing of laser fields for temporal gating of high-order harmonic generation.* Physical review letters, 2006. **97**(16): p. 163901.

47. Mashiko, H., S. Gilbertson, C. Li, S.D. Khan, M.M. Shakya, E. Moon, and Z. Chang, *Double optical gating of high-order harmonic generation with carrier-envelope phase stabilized lasers.* Physical review letters, 2008. **100**(10): p. 103906.

48. Feng, X., S. Gilbertson, H. Mashiko, H. Wang, S.D. Khan, M. Chini, Y. Wu, K. Zhao, and Z. Chang, *Generation of isolated attosecond pulses with 20 to 28 femtosecond lasers.* Physical review letters, 2009. **103**(18): p. 183901.

49. Gilbertson, S., H. Mashiko, C. Li, S.D. Khan, M.M. Shakya, E. Moon, and Z. Chang, *A low-loss, robust setup for double optical gating of high harmonic generation.* Applied Physics Letters, 2008. **92**(7): p. 071109.

50. Gilbertson, S., Y. Wu, S.D. Khan, M. Chini, K. Zhao, X. Feng, and Z. Chang, *Isolated attosecond pulse generation using multicycle pulses directly from a laser amplifier.* Physical Review A, 2010. **81**(4): p. 043810.

51. Tamaki, Y., J. Itatani, M. Obara, and K. Midorikawa, *Optimization of conversion efficiency and spatial quality of high-order harmonic generation.* Physical Review A, 2000. **62**(6): p. 063802.

52. Ditmire, T., J. Crane, H. Nguyen, L. DaSilva, and M. Perry, *Energy-yield and conversion-efficiency measurements of high-order harmonic radiation.* Physical Review A, 1995. **51**(2): p. R902.

53. Cunningham, E., Y. Wu, and Z. Chang, *Carrier-envelope phase control of a 10 Hz, 25 TW laser for high-flux extreme ultraviolet quasi-continuum generation.* Applied Physics Letters, 2015. **107**(20): p. 201108.

54. Strickland, D. and G. Mourou, *Compression of amplified chirped optical pulses.* Optics communications, 1985. **55**(6): p. 447-449.

55. Backus, S., C.G. Durfee III, M.M. Murnane, and H.C. Kapteyn, *High power ultrafast lasers.* Review of scientific instruments, 1998. **69**(3): p. 1207-1223.

56. Morgner, U., F.X. Kärtner, S.-H. Cho, Y. Chen, H.A. Haus, J.G. Fujimoto, E.P. Ippen, V. Scheuer, G. Angelow, and T. Tschudi, *Sub-two-cycle pulses from a Kerr-lens mode-locked Ti: sapphire laser.* Optics letters, 1999. **24**(6): p. 411-413.

57. Martinez, O., *3000 times grating compressor with positive group velocity dispersion: Application to fiber compensation in 1.3-1.6 μm region.* IEEE Journal of Quantum Electronics, 1987. **23**(1): p. 59-64.

58. Martinez, O., *Design of high-power ultrashort pulse amplifiers by expansion and recompression.* IEEE Journal of Quantum Electronics, 1987. **23**(8): p. 1385-1387.

59. Martinez, O., J. Gordon, and R. Fork, *Negative group-velocity dispersion using refraction.* JOSA A, 1984. **1**(10): p. 1003-1006.

60. Shan, B., C. Wang, and Z. Chang, *High peak-power kilohertz laser system employing single-stage multi-pass amplification*. 2006, Google Patents.

61. Valasek, J., *Properties of Rochelle salt related to the piezo-electric effect.* Physical Review, 1922. **20**(6): p. 639.

62. Moulton, P., *Ti-doped sapphire: tunable solid-state laser.* Optics News, 1982. **8**(6): p. 9-9.

63. Nisoli, M., S. De Silvestri, and O. Svelto, *Generation of high energy 10 fs pulses by a new pulse compression technique.* Applied Physics Letters, 1996. **68**(20): p. 2793-2795.

64. Nisoli, M., S. De Silvestri, O. Svelto, R. Szipöcs, K. Ferencz, C. Spielmann, S. Sartania, and F. Krausz, *Compression of high-energy laser pulses below 5 fs.* Optics letters, 1997. **22**(8): p. 522-524.

65. Cheriaux, G., B. Walker, L. Dimauro, P. Rousseau, F. Salin, and J. Chambaret, *Aberration-free stretcher design for ultrashort-pulse amplification.* Optics letters, 1996. **21**(6): p. 414-416.

66. Du, D., C. Bogusch, C.T. Cotton, J. Squier, S. Kane, G. Korn, and G. Mourou, *Terawatt Ti: sapphire laser with a spherical reflective-optic pulse expander.* Optics letters, 1995. **20**(20): p. 2114-2116.

67. Seres, J., A. Müller, E. Seres, K. O'Keeffe, M. Lenner, R.F. Herzog, D. Kaplan, C. Spielmann, and F. Krausz, *Sub-10-fs, terawatt-scale Ti: sapphire laser system.* Optics letters, 2003. **28**(19): p. 1832-1834.

68. Kopp, C., L. Ravel, and P. Meyrueis, *Efficient beamshaper homogenizer design combining diffractive optical elements, microlens array and random phase plate.* Journal of Optics A: Pure and Applied Optics, 1999. **1**(3): p. 398.

69. Takada, H., M. Kakehata, and K. Torizuka, *Broadband high-energy mirror for ultrashort pulse amplification system.* Applied Physics B: Lasers and Optics, 2000. **70**(7): p. S189-S192.

70. Tournois, P., *Acousto-optic programmable dispersive filter for adaptive compensation of group delay time dispersion in laser systems.* Optics communications, 1997. **140**(4-6): p. 245-249.

71. Trebino, R., *Frequency-resolved optical gating: the measurement of ultrashort laser pulses*. 2012: Springer Science & Business Media.

72. Chini, M., H. Mashiko, H. Wang, S. Chen, C. Yun, S. Scott, S. Gilbertson, and Z. Chang, *Delay control in attosecond pump-probe experiments.* Optics express, 2009. **17**(24): p. 21459-21464.

73. Baker, S., J.S. Robinson, C. Haworth, H. Teng, R. Smith, C. Chirilă, M. Lein, J. Tisch, and J.P. Marangos, *Probing proton dynamics in molecules on an attosecond time scale.* Science, 2006. **312**(5772): p. 424-427.

74. Calegari, F., G. Sansone, S. Stagira, C. Vozzi, and M. Nisoli, *Advances in attosecond science.* Journal of Physics B: Atomic, Molecular and Optical Physics, 2016. **49**(6): p. 062001.

75. Boutu, W., T. Auguste, J. Caumes, H. Merdji, and B. Carré, *Scaling of the generation of high-order harmonics in large gas media with focal length.* Physical Review A, 2011. **84**(5): p. 053819.

76. Hergott, J.-F., M. Kovacev, H. Merdji, C. Hubert, Y. Mairesse, E. Jean, P. Breger, P. Agostini, B. Carré, and P. Salières, *Extreme-ultraviolet high-order harmonic pulses in the microjoule range.* Physical Review A, 2002. **66**(2): p. 021801.

77. Rudawski, P., C. Heyl, F. Brizuela, J. Schwenke, A. Persson, E. Mansten, R. Rakowski, L. Rading, F. Campi, and B. Kim, *A high-flux high-order harmonic source.* Review of Scientific Instruments, 2013. **84**(7): p. 073103.

78. Chanteloup, J.-C., F. Druon, M. Nantel, A. Maksimchuk, and G. Mourou, *Single-shot wave-front measurements of high-intensity ultrashort laser pulses with a three-wave interferometer.* Optics letters, 1998. **23**(8): p. 621-623.

79. Druon, F., G. Chériaux, J. Faure, J. Nees, M. Nantel, A. Maksimchuk, G. Mourou, J.C. Chanteloup, and G. Vdovin, *Wave-front correction of femtosecond terawatt lasers by deformable mirrors.* Optics letters, 1998. **23**(13): p. 1043-1045.

80. Chanteloup, J.-C., H. Baldis, A. Migus, G. Mourou, B. Loiseaux, and J.-P. Huignard, *Nearly diffraction-limited laser focal spot obtained by use of an optically addressed light valve in an adaptive-optics loop.* Optics letters, 1998. **23**(6): p. 475-477.

81. Hornbeck, L.J., *Deformable mirror light modulator*. 1984, Google Patents.

82. Platt, B.C. and R. Shack, *History and principles of Shack-Hartmann wavefront sensing.* Journal of Refractive Surgery, 2001. **17**(5): p. S573-S577.

83. Thomas, S., T. Fusco, A. Tokovinin, M. Nicolle, V. Michau, and G. Rousset, *Comparison of centroid computation algorithms in a Shack–Hartmann sensor.* Monthly Notices of the Royal Astronomical Society, 2006. **371**(1): p. 323-336.

84. Lane, R. and M. Tallon, *Wave-front reconstruction using a Shack–Hartmann sensor.* Applied optics, 1992. **31**(32): p. 6902-6908.

85. Noll, R.J., *Zernike polynomials and atmospheric turbulence.* JOsA, 1976. **66**(3): p. 207-211.

86. Born, M. and E. Wolf, *Principles of optics: electromagnetic theory of propagation, interference and diffraction of light*. 2013: Elsevier.

87. Ranc, S., G. Chériaux, S. Ferré, J.-P. Rousseau, and J.-P. Chambaret, *Importance of spatial quality of intense femtosecond pulses.* Applied Physics B: Lasers and Optics, 2000. **70**(7): p. S181-S187.

88. Takahashi, E.J., Y. Nabekawa, and K. Midorikawa, *Low-divergence coherent soft x-ray source at 13 nm by high-order harmonics.* Applied physics letters, 2004. **84**(1): p. 4-6.

89. Takahashi, E., Y. Nabekawa, M. Nurhuda, and K. Midorikawa, *Generation of high-energy high-order harmonics by use of a long interaction medium.* JOSA B, 2003. **20**(1): p. 158-165.

90. Balcou, P., P. Salieres, A. L'Huillier, and M. Lewenstein, *Generalized phase-matching conditions for high harmonics: The role of field-gradient forces.* Physical Review A, 1997. **55**(4): p. 3204.

91. Popmintchev, T., M.-C. Chen, O. Cohen, M.E. Grisham, J.J. Rocca, M.M. Murnane, and H.C. Kapteyn, *Extended phase matching of high harmonics driven by mid-infrared light.* Optics letters, 2008. **33**(18): p. 2128-2130.

92. Siegman, A.E., *Lasers university science books.* Mill Valley, CA, 1986. **37**: p. 462-466.

93. Chin, S.L., W. Liu, F. Théberge, Q. Luo, S.A. Hosseini, V.P. Kandidov, O.G. Kosareva, N. Aközbek, A. Becker, and H. Schroeder, *Some fundamental concepts of femtosecond laser filamentation.* Progress in Ultrafast Intense Laser Science III, 2008: p. 243-264.

94. Lewenstein, M., P. Salieres, and A. L'huillier, *Phase of the atomic polarization in high-order harmonic generation.* Physical Review A, 1995. **52**(6): p. 4747.

95. Lewenstein, M., P. Balcou, M.Y. Ivanov, A. L'huillier, and P.B. Corkum, *Theory of high-harmonic generation by low-frequency laser fields.* Physical Review A, 1994. **49**(3): p. 2117.

96. Takahashi, E.J., Y. Nabekawa, H. Mashiko, H. Hasegawa, A. Suda, and K. Midorikawa, *Generation of strong optical field in soft x-ray region by using high-order harmonics.* IEEE Journal of Selected Topics in Quantum Electronics, 2004. **10**(6): p. 1315-1328.

97. Krause, J.L., K.J. Schafer, and K.C. Kulander, *Calculation of photoemission from atoms subject to intense laser fields.* Physical Review A, 1992. **45**(7): p. 4998.

98. Nagata, Y., Y. Nabekawa, and K. Midorikawa, *Development of high-throughput, high-damage-threshold beam separator for13 nm high-order harmonics.* Optics letters, 2006. **31**(9): p. 1316-1318.

99. Uiberacker, M., T. Uphues, M. Schultze, A.J. Verhoef, V. Yakovlev, M.F. Kling, J. Rauschenberger, N.M. Kabachnik, H. Schröder, and M. Lezius, *Attosecond real-time observation of electron tunnelling in atoms.* Nature, 2007. **446**(7136): p. 627.

100. Mimura, H., S. Matsuyama, H. Yumoto, H. Hara, K. Yamamura, Y. Sano, M. Shibahara, K. Endo, Y. Mori, and Y. Nishino, *Hard X-ray diffraction-limited nanofocusing with Kirkpatrick-Baez mirrors.* Japanese journal of applied physics, 2005. **44**(4L): p. L539.

101. McKinsey, D., C. Brome, J. Butterworth, R. Golub, K. Habicht, P. Huffman, S. Lamoreaux, C. Mattoni, and J. Doyle, *Fluorescence efficiencies of thin scintillating films in the extreme ultraviolet spectral region.* Nuclear Instruments and Methods in Physics Research Section B: Beam Interactions with Materials and Atoms, 1997. **132**(3): p. 351-358.

102. Li, G. and G.M. Hieftje, *Time-of-flight mass spectrometer*. 1997, Google Patents.

103. Feldman, U. and K. Widing, *Photospheric abundances of oxygen, neon, and argon derived from the XUV spectrum of an impulsive flare.* The Astrophysical Journal, 1990. **363**: p. 292-298.

104. Wang, Y., Y. Liu, X. Yang, and Z. Xu, *Spectral splitting in high-order harmonic generation.* Physical Review A, 2000. **62**(6): p. 063806.

105. Kim, H.T., I.J. Kim, D.G. Lee, K.-H. Hong, Y.S. Lee, V. Tosa, and C.H. Nam, *Optimization of high-order harmonic brightness in the space and time domains.* Physical Review A, 2004. **69**(3): p. 031805.

106. Vedder, P.W. and J.F. Lindblom, *Thin film filter performance for extreme ultraviolet and x-ray applications.* Optical Engineering, 1990. **29**(6): p. 614-624.

107. Brabec, T. and F. Krausz, *Intense few-cycle laser fields: Frontiers of nonlinear optics.* Reviews of Modern Physics, 2000. **72**(2): p. 545.

108. Shim, B., S.E. Schrauth, and A.L. Gaeta, *Filamentation in air with ultrashort mid-infrared pulses.* Optics express, 2011. **19**(10): p. 9118-9126.

109. Wang, L., X. Lu, H. Teng, T. Xi, S. Chen, P. He, X. He, and Z. Wei, *Carrier-envelope phase-dependent electronic conductivity in an air filament driven by few-cycle laser pulses.* Physical Review A, 2016. **94**(1): p. 013827.

110. Bergé, L., C.-L. Soulez, C. Köhler, and S. Skupin, *Role of the carrier-envelope phase in laser filamentation.* Applied Physics B: Lasers and Optics, 2011. **103**(3): p. 563-570.

111. Paulus, G., F. Grasbon, H. Walther, and P. Villoresi, *Absolute-phase phenomena in photoionization with few-cycle laser pulses.* Nature, 2001. **414**(6860): p. 182.

112. Haworth, C., L. Chipperfield, J. Robinson, P. Knight, J. Marangos, and J. Tisch, *Half-cycle cutoffs in harmonic spectra and robust carrier-envelope phase retrieval.* Nature Physics, 2007. **3**(1).

113. Gu, X., G. Marcus, Y. Deng, T. Metzger, C. Teisset, N. Ishii, T. Fuji, A. Baltuska, R. Butkus, and V. Pervak, *Generation of carrier-envelope-phase-stable 2-cycle 740-μJ pulses at 2.1-μm carrier wavelength.* Optics express, 2009. **17**(1): p. 62-69.

114. Hauri, C., R.B. Lopez-Martens, C. Blaga, K. Schultz, J. Cryan, R. Chirla, P. Colosimo, G. Doumy, A. March, and C. Roedig, *Intense self-compressed, self-phase-stabilized few-cycle pulses at 2 μm from an optical filament.* Optics letters, 2007. **32**(7): p. 868-870.

115. Mücke, O.D., S. Ališauskas, A.J. Verhoef, A. Pugžlys, A. Baltuška, V. Smilgevičius, J. Pocius, L. Giniūnas, R. Danielius, and N. Forget, *Self-compression of millijoule 1.5 μm pulses.* Optics letters, 2009. **34**(16): p. 2498-2500.

116. Vozzi, C., F. Calegari, E. Benedetti, S. Gasilov, G. Sansone, G. Cerullo, M. Nisoli, S. De Silvestri, and S. Stagira, *Millijoule-level phase-stabilized few-optical-cycle infrared parametric source.* Optics letters, 2007. **32**(20): p. 2957-2959.

117. Giguère, M., B.E. Schmidt, A.D. Shiner, M.-A. Houle, H.C. Bandulet, G. Tempea, D.M. Villeneuve, J.-C. Kieffer, and F. Légaré, *Pulse compression of submillijoule few-optical-cycle infrared laser pulses using chirped mirrors.* Optics letters, 2009. **34**(12): p. 1894-1896.

118. Yin, Y., J. Li, X. Ren, K. Zhao, Y. Wu, E. Cunningham, and Z. Chang, *High-efficiency optical parametric chirped-pulse amplifier in BiB 3 O 6 for generation of 3 mJ, two-cycle, carrier-envelope-phase-stable pulses at 1.7 μm.* Optics letters, 2016. **41**(6): p. 1142-1145.

119. Shen, Y.-R., *The principles of nonlinear optics.* New York, Wiley-Interscience, 1984, 575 p., 1984.

120. Fuji, T., N. Ishii, C.Y. Teisset, X. Gu, T. Metzger, A. Baltuska, N. Forget, D. Kaplan, A. Galvanauskas, and F. Krausz, *Parametric amplification of few-cycle carrier-envelope phase-stable pulses at 2.1 μm.* Optics letters, 2006. **31**(8): p. 1103-1105.

121. Fang, X. and T. Kobayashi, *Self-stabilization of the carrier-envelope phase of an optical parametric amplifier verified with a photonic crystal fiber.* Optics letters, 2004. **29**(11): p. 1282-1284.

122. Mitrofanov, A., A. Voronin, D. Sidorov-Biryukov, A. Pugžlys, E. Stepanov, G. Andriukaitis, T. Flöry, S. Ališauskas, A. Fedotov, and A. Baltuška, *Mid-infrared laser filaments in the atmosphere.* Scientific reports, 2015. **5**.

123. Chiao, R.Y., E. Garmire, and C.H. Townes, *Self-trapping of optical beams.* Physical Review Letters, 1964. **13**(15): p. 479.

124. Tempea, G. and T. Brabec, *Theory of self-focusing in a hollow waveguide.* Optics letters, 1998. **23**(10): p. 762-764.

125. Cheng, Y.-H., J.K. Wahlstrand, N. Jhajj, and H. Milchberg, *The effect of long timescale gas dynamics on femtosecond filamentation.* Optics express, 2013. **21**(4): p. 4740-4751.

126. Liang, Y., J.M. Watson, and S. Chin, *Second harmonic generation in gases with a high-intensity CO2 laser.* Journal of Physics B: Atomic, Molecular and Optical Physics, 1992. **25**(11): p. 2725.